UNIVERSITÀ DEGLI STUDI DI PARMA
DIPARTIMENTO DI FISICA

Synthesis, Structural Investigation and Spectroscopic Properties of Lithium Fullerides

Daniele Pontiroli

Thesis submitted for the award of the degree of Ph.D. in Physics
Dottorato di Ricerca in Fisica

Supervisor: Prof. Mauro Riccò

XVIII Ciclo - Gennaio 2006

A mio nonno Mario

Contents

Introduction

Fullerenes, the third of carbon allotrope besides diamond and graphite, have profoundly fascinated the scientific community since their discovery in 1985, by Kroto and Smalley [1]. The in large scale production of fullerenes, made available thanks to the adoption of Krätschmer and Huffman method in 1990, opened a "new era" in carbon chemistry [2].

The most abundant molecule of this family is Buckminsterfullerene C_{60}, so called in honour of the American architect R. Buckminster Fuller. This is a stable carbon molecule with the typical shape of a "soccer ball", in which carbon atoms retain some sp^3 character besides the essentially sp^2 hybridisation, like in graphite. This provides the necessary curvature to obtain a closed-cage structure, but, at the same time, it promotes the presence of unsaturated molecular π frontier orbitals.

On one hand, the quasi-spherical shape of C_{60} is particularly favourable to aggregate in a Van der Waals molecular solid, the *fullerite*, in which the presence of empty spaces can facilitate the intercalation of other small molecules or atoms. On the other hand, the relatively small superposition of molecular orbitals yields narrow electronic bands when the molecules are brought togheter to form a solid.

Thanks to these features, C_{60} represents the ideal "building block" for a rather varied family of compounds, the *fullerides*, which display several attractive physical properties. They consist of charge-transfer salts, obtained by the intercalation of C_{60} crystals with electron donor atoms (alkali, alkali-earth, rare-earth atoms). Due to the presence of empty orbitals, C_{60} is able to receive the alkali electron, while metallic ions fill the wide interstices of the host lattice, thus stabilising the overall structure.

The presence of electrons in the delocalised three-fold degenerate $LUMO$ (Lowest Unoccupied Molecular Orbital) of C_{60} significantly changes the physical behaviour of the compound; if the pristine fullerene is a diamagnetic semiconductor, on the contrary doped fullerides can display metallicity, superconductivity and even magnetic order [3, 4]. The richness of physical states which can be observed is due to the strong electronic correlations, which cannot be neglected in these systems, because of the

high density of states in the narrow bands in the solid, reflecting their molecular orbital characters.

A typical example is the K_xC_{60} ($1 \leq x \leq 6$) series, in which the *LUMO* is progressively filled as doping increases. For $x = 6$, the compound is an insulator, as expected from the complete filling of the LUMO band, whereas for $x = 3$ the half-filled band yields a metal, with a superconducting transition below $\sim$ 19 K; but surprisingly, for $x = 4$, the compound is again a *nonmagnetic insulator*, probably due to the cooperative effect of Mott-Hubbard localisation and Jahn Teller distortion. Finally, for $x = 1$, the system displays a *1D polymerisation* of the fullerene units and low-dimension metallicity, with a *metal-to-insulator* transition at low temperature.

This last example shows that fullerides can display not only electronic, but also *structural* instabilities [5]. Among these, *polymerisation* is an interesting phenomenon in C_{60} compounds; either because it permits to obtain systems with low-dimensional character, as for example 1D conductivity and spin density waves (SDW); or because a polymer has potentially attractive mechanical properties. Moreover, recent studies have shown that polymers of fullerenes could also show remarkable magnetic properties, as in the rhombohedral 2D polymerised C_{60} phase, which displays ferromagnetic order up to 500 K [6].

In this context, lithium-doped fullerides appear as a very promising class of new fulleride compounds, which are only partially known, mainly due to the difficulties in their preparation. Despite this, the interest in these systems goes back to almost fifteen years ago, when theoretical studies based on the Car-Parrinello method, supported also by experiments on molecular beams of C_{60}, evidenced the possibility of the formation of a stable $Li_{12}C_{60}$ superfulleroid phase [7]. The superfulleroid structure would keep the icosahedrical symmetry of C_{60} and hence also the high degeneracy of the frontier orbitals, feature strictly connected to the superconductive behaviour, but has never been observed in the solid phase. On the contrary, the study of lithium fullerides evidenced other peculiar features of these systems. The investigation of the Li_xCsC_{60} phases has shown the presence of strong Li^+-C interactions, which appears as a partial charge transfer from the alkali to the buckyball [8]. Moreover, thanks to the small alkali dimensions, a larger doping range in the host fullerene structure can be obtained and up to 30 Li atoms per C_{60} units can be incorporated in the host lattice (whereas the maximum limit is 6 for K, Rb, Cs and 11 for Na) [9]. For high doping rate ($x > 7$) the formation of lithium clusters in the largest fullerene interstices was observed [10]. For the "low doped" systems, on the contrary, the small steric hindrance of Li^+ ions allows the fullerene units to get close enough and therefore the polymerisation of C_{60}

is possible and was observed by several groups [9, 11].

In the present thesis a systematic study of the largely unknown "low doped" lithium fullerides was made, in an effort to shed light on this class of fullerene-based materials and to evidence their specific structural and electronic properties. The structural investigation was performed mainly by diffraction techniques, both with laboratory and synchrotron x-ray, whereas the electronic and vibrational properties were probed with Raman spectroscopy. Moreover, a parallel investigation using resonance techniques, such as Nuclear Magnetic Resonance (NMR) both static and Magic Angle Spinning (MAS), and Electron Spin Resonance (ESR) completes the current analysis [12].

The first chapter of this work introduces the systems under study: first, the basic theoretical background necessary to understand the remarkable electronic properties of alkali doped fullerides is given, then the phenomenology of C_{60} polymerisation, both in undoped and in doped systems, is presented. Next, lithium fullerides are introduced, and subsequently the role of ammonia molecules in fullerene compounds is discussed.

In the second chapter, the x-ray diffraction technique, the main experimental tool of investigation in this work, is extensively discussed, with particular regard to the sources used and the experimental setup in case of polycrystalline materials.

The third chapter deals with the Raman spectroscopy technique, mainly applied to fullerene compounds; after a general classical introduction to the Raman scattering phenomenon, the main features of the Raman spectra, related with C_{60} molecular dynamics, in the various fullerene systems are explained.

In the fourth chapter, an overview of the most common strategies used to perform an *ab-initio* structural analysis starting from powder diffraction data is given. The main software applications, extensively used during this work, are also briefly described.

The fifth and the sixth chapters are devoted to the experimental results. In the former, the main aspects of the sample preparation, which represented an important part of this work, are explained. In the latter the outcome of x-ray diffraction and Raman measurements are presented and discussed.

Finally, the conclusions summarize the most important results obtained.

Chapter 1

Fullerenes and fullerides

Introduction

This first chapter is an overview of the systems which were the object of this work: the alkali doped fullerides and in particular the lithium fullerides. First (sec. 1.1), the main features of Buckminsterfullerene are explained. Then (sec. 1.2), the alkali doped fullerides are introduced, with some elements of the theoretical background necessary to understand their complex physics (sec. 1.3). Next, the attention is focussed on polymerisation in fullerenes (sec. 1.4), both in the undoped and in the doped species, and hence the family of lithium doped fullerides is introduced (sec. 1.5). Finally, some details about the ammoniated fullerides is given (sec. 1.6).

1.1 Fullerene C_{60}

C_{60} is the most common representative of the fullerene family. The molecule presents the shape of a truncated icosahedron, with high symmetry, defined by the point group I_h. The 60 equivalent carbons of the cage form 12 pentagons and 12 hexagons, describing a spherical surface whose radius is ~ 3.56 Å (see fig. 1.1a). Actually, the electronic wave functions of the molecular orbitals extend inside and outside the sphere by about 1.5 Å, thus the outer diameter of the molecule is ~ 10 Å. Moreover, the π electrons are not homogeneously delocalised on the sphere, and there are two different C-C bond lengths in the buckyball: the edges shared by two hexagons are $b_{hh} \sim 1.46$ Å, whereas those between an hexagon and a pentagon are shorter, $b_{ph} \sim 1.40$ Å (for comparison, the C-C distance is 1.54 Å in diamond and 1.42 Å in graphite).

The production of fullerenes is a well consolidated technique, based on the evap-

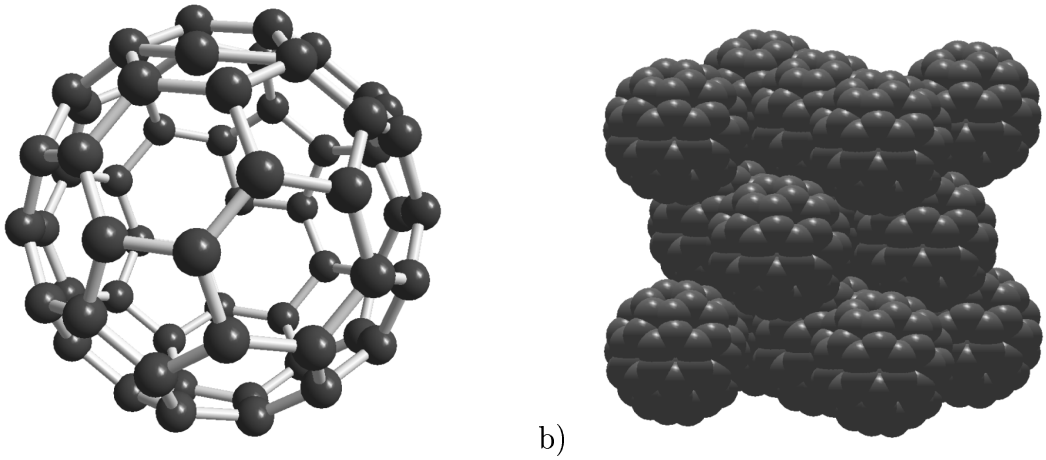

a) b)

Figure 1.1: a) A schematic representation of the C_{60} molecule and b) the crystal *fcc* structure of solid C_{60}.

orisation of rods of pure graphite through arc discharge in an inhert atmosphere (200 mBar of He); this is the Krätschmer and Huffman method [2]. The obtained soot undergoes chromatography, which permits to separate the various fullerene species. The most abundant are C_{60} and C_{70} (respectively $\sim 80\%$ and $\sim 20\%$ of the produced fullerenes).

In the solid state, C_{60} molecules arrange to form a *face centered cubic* lattice (see fig. 1.1b), with spatial group $\mathbf{F\,m\,\overline{3}\,m}$, a = 14.17 Å, and $d_{C60-C60} = 10.02$ Å at 300 K. At room temperature the molecules rotates freely around their centre of gravity, thus giving rise to a *plastic crystal*. With the decrease of temperature, the rotation stops below 260 K and the structure becomes *simple cubic* (spatial group: $\mathbf{P\,a\,\overline{3}}$), because the intrinsic incompatibility of the icosahedral symmetry of C_{60} and the cubic symmetry prevent the description of the structure with the *fcc* lattice [13]. More specifically, in this phase neighbouring buckyballs are still in motion, but their rotational axes are now hindered along different [1 1 1] directions, this configuration satisfying the *sc* symmetry.

The main feature in the solid C_{60} is the presence of two energetic scales: one associated to the strong intramolecular covalent bonds of the cage and the other due to the soft interball Van der Waals binding of the solid. This deeply influences the electronic behaviour, in fact the band model of the solid resembles the molecular levels (fig. 1.2), which result only weakly splitted in narrow bands; the Lowest Unoccupied Molecular Orbital (LUMO) presents a non-bonding nature, in agreement with the strong electronegative character of the molecule, and is triply degenerate with t_u symmetry. Cyclovoltammetric measurements [14, 15] on solutions of C_{60} in solvents explored the

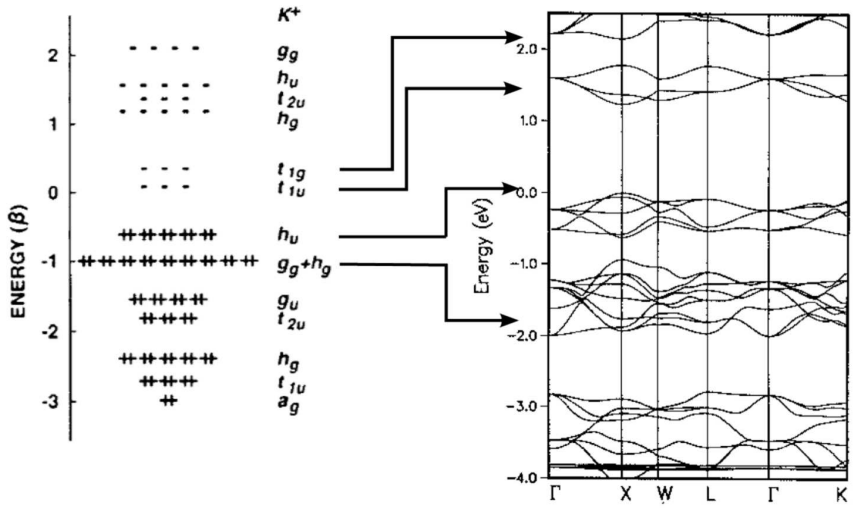

Figure 1.2: A scheme of molecular orbitals of C_{60} and the derived electronic band structure in the molecular crystal.

progressive filling of this orbital, and have shown the presence of C_{60}^{n-} stable states with n up to 6. But doped species, obtained by intercalation of alkali-earth atoms, indicate that it is even possible to reach anion charges of up to 12^- [16]; in that case also the t_{1g} LUMO + 1 level is populated.

In the following table the main properties of the solid C_{60} are summarised:

Average C - C distance	1.44 Å
fcc lattice constant	14.17 Å
C_{60} mean ball diameter	6.83 Å
C_{60} outer ball diameter	10.18 Å
C_{60} inner ball diameter	3.48 Å
Tetrahedral site radius	1.12 Å
Octahedral site radius	2.07 Å
Mass density	1.72 g/cm^3
Electron affinity	2.65 eV
Ionisation potential (1^{st})	7.58 eV
Ionisation potential (2^{nd})	11.5 eV
Vol. coeff. thermal expansion	$6.2 \cdot 10^{-5}$cm^3/K
Band gap (HOMO - LUMO)	1.7 eV

Table 1.1: Main physical properties of solid C_{60}.

1.2 Alkali doped fullerides

The low reduction potential of the C_{60} molecule and the presence of many intermolecular space available in the crystal structure make the intercalation chemistry of solid C_{60} with electron donors atoms very rich and easy. This permits the formation of charged transfer salts based on fullerenes, so called *fullerides*. Moreover, the relative modest splitting of the bands in the solid and the presence of high energy intramolecular vibrational states, due to the "rigidity" of the fullerene cage, are promises of non-conventional electronic properties of the fullerides, as high T_c superconductivity and metal-to-insulator transitions.

The intercalation of electron donor atoms in the host fullerene lattice yields the formations of very interesting compounds, whose noticeable physical properties, since almost fifteen years, are still debated and discussed. The undoped C_{60} is a semiconductor with a gap between HOMO and LUMO of ~ 1.7 eV. Of course, if new electrons are given to the buckyball, the conduction band progressively fills and changes in the transport properties are expected. This is obtained by the intercalation of alkali atoms (A = potassium, rubidium, cesium) in the fullerene lattice. For example, the half filling of the t_{1u} orbital reached in K_3C_{60} (*fcc*, spatial group $\mathbf{F\,m\,\overline{3}\,m}$, $a = 14.24$ Å) gives rise to a metallic phase [17, 3], with a superconducting transition below $T_c = 19$ K. On the contrary, K_6C_{60} (*bcc*, spatial group $\mathbf{I\,m\,\overline{3}}$, $a = 11.39$ Å) is an insulator. Surprisingly, insulating non-magnetic ground state is found also in K_4C_{60} (*bct*, spatial group $\mathbf{I\,4/m\,m\,m}$, $a = 11.89$ Å, $c = 10.77$ Å) [18, 19], which should be metallic, basing on the classical band theory. The deviation from the classical theory of the conducting properties of the A_xC_{60} compounds, together with the very high T_c which characterises the $x = 3$ phases, as compared with the other BCS-like materials, are strong hints of the fact that intercalated fullerides are highly electron correlated systems. In the next section the main theoretical bases necessary to a more complete understanding of the electronic features in A_xC_{60} compounds will be given.

1.3 Theoretical background

In alkali doped fullerenes, many factors have to be considered, in order to describe their electronic behaviour:

- Fullerides are strong correlated systems, as indicated both from theoretical and experimental works, and the classical band theory is insufficient to explain the experimental results

- The electronic properties arise from a narrow conduction band, which, depending on the level of symmetry in the system, can conserve the triply degeneracy of the t_{1u} orbitals

- There is a strong coupling between the conduction electrons and the intramolecular phonons of the buckyball, which could yield to superconductivity and/or structural deformations

Fulleride phenomenology consists then of the interplay of all these factors; they generally must be treated simultaneously, because, as it will be shown in the following sections, their typical energy results of the same order of magnitude.

1.3.1 The Hubbard model

When the electron-electron interactions in a solid are sufficiently strong to invalidate the classical one-electron approximation, it is necessary to introduce a new parameter in the many-body Hamiltonian, which can take into account the interelectron repulsion. The simplest model which is capable to describe the effect of correlations was proposed by Hubbard. For a non degenerate partially filled band, the *Hubbard Hamiltonian* is [20]:

$$H = -t \sum_{i,j} (c^+_{i\uparrow} c_{j\uparrow} + c^+_{i\downarrow} c_{j\downarrow}) + U \sum_i n_{i\uparrow} n_{i\downarrow} \tag{1.1}$$

where $c^+_{i\uparrow}$ creates a spin-up electron at the site i, $c_{j\downarrow}$ annihilates a spin-down electron at the site j, and $n_{i\uparrow} = c^+_{i\uparrow} c_{i\uparrow}$ is the number of spin-up electrons in the site i (zero or the unity, based on the Pauli's principle). In the eq. 1.1, the t parameter in the first term is the *hopping matrix element*; it represents the kinetic energy of the electrons which visit different sites without changing their spin orientation, and is proportional to the bandwidth W. On the contrary, in the second term, the *Hubbard parameter* U, indicates the increase of the energy when a spin-down electron is added to a site where a spin-up electron already exists, arising from the Coulomb interactions. The two terms are in competition; basing on this simple model, if $U/W < 1$, the electrons are delocalised and the system is a metal, according with the classical theory. On the contrary, if $U/W > 1$, the on-site Coulomb repulsion prevents the hopping and the compound becomes a *Mott-Hubbard insulator*.

In fullerides, theoretical calculations of the density of states [21, 22] indicate that typical values for W are $0.5 - 0.6$ eV; on the other hand, concerning the electron repulsion, LDA calculations which take into account also the shielding effects found

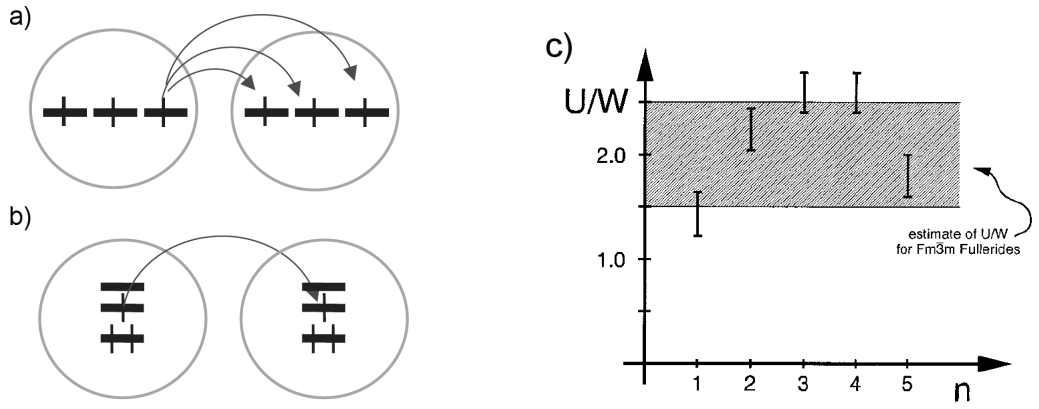

Figure 1.3: a) Hopping channels in change transfer between trivalent fullerene molecules with triply degenerate t_{1u} orbitals and b) without degeneracy. c) Estimation of the critical ratio $(U/W)_c$ in a multiband Hubbard model which describes *fcc* fullerides, for different filling rate n of the degenerate t_{1u} band.

that $U = 0.8 - 1.3$ eV [5]. This yields U/W in the range $1.3 - 2.6$; hence, all the alkali fullerides should be Mott-Hubbard insulators. The metallic behaviour of K_3C_{60} is recovered if the triple degeneracy of the t_{1u} orbitals due to the face centered cubic structure of this compound is taken in account, as shown by Gunnarson et al. [23]; it emerged that, for a half-filled system with orbital degeneracy N, the critical value $(U/W)_c$ is enhanced by a factor $\sqrt{N}$; the presence of degeneracy, in fact, introduces new hopping channels, as shown in fig. 1.3a and 1.3b. By moving from the ideal half-filling condition and in presence of band degeneracy, this effect remains, even if smaller, also for the other stoichiometries (see fig. 1.3c) [24]. Further enhancement arises from the *frustrated* nature of the *fcc* lattice [25]. The new value $(U/W)_c \sim 2.3$ places K_3C_{60} near to a metal-to-insulator transition, and justifies the high T_c of its superconducting phase.

1.3.2 Jahn Teller effect and Hund's rule

The high symmetry of the fullerene molecule is an unsuitable feature for a system which needs to minimise its ground energy. According to the Jahn-Teller theorem, *any non linear molecular system in a degenerate electronic state is unstable, and undergoes distortion to form a system with lower symmetry and lower energy, by removing the degeneracy.* These deformations are very small, and no clear evidences of their presence in bulk fullerides have been given yet [26]. Nevertheless, there is a general consensus

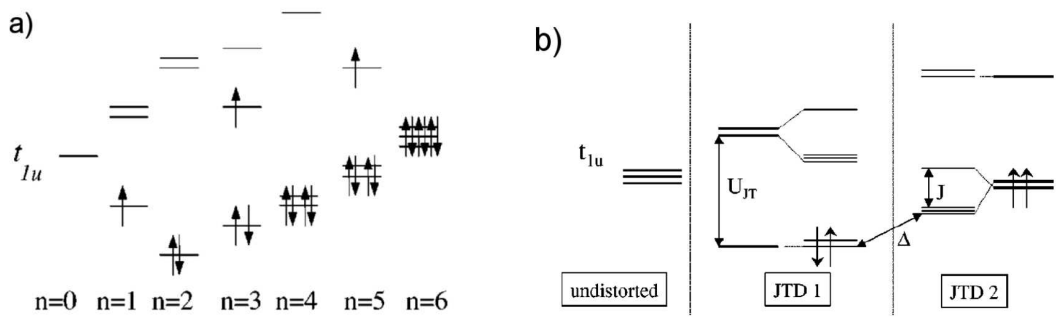

Figure 1.4: a) Schematic representation of the splitting of the t_{1u} levels in C_{60} induced by JTD. Only the most stable JTD is shown. b) The two most stable distortions, called JTD1 and JTD2 for the three t_{1u} levels with two electron per C_{60}: the optical (U_{JT}) and singlet-triplet (Δ) gaps, and the exchange splitting (J) are shown [27].

that *Jahn Teller Distortions* (JTD) play an essential role in the electronic properties of alkali doped fullerides.

In fig. 1.4a it is shown a schematic representation of the t_{1u} levels induced by JTD in the fullerene molecule. The energy gain from JTD always results larger for *even* x, and favours a singlet insulating state. On the contrary, for *odd* stoichiometries, the enhancing of the distortions leads to an effective attraction between electrons [5], which results in a small opposite contribution to the Coulomb repulsion. Typical Jahn Teller energies in fullerides range from 0.1 and 0.5 eV, and arise from the coupling between electrons and the H_g intramolecular vibrational modes (see later in chap. 3). Moreover, JTD can be either *static* or *dynamic*; in the first case, the system results frozen in one configuration of lowest energy, whereas in the second case molecules resonate on several degenerate distorted arrangements. Theoretical studies suggested [26] that the latter configuration should be preferred by fullerene systems.

Since JTD favours a low-spin ground state, it is in competition with the *Hund's rule coupling*, which on the contrary promotes a high spin state. This last interaction, as known, originates from the *exchange integral* (J) [28], which should favour a ferromagnetic coupling for electrons filling degenerate orbitals, thus maximising the multiplet spin. Again, in fullerene these two contributions display similar energies ($\sim$ 0.1 eV); however, since no high spin configuration was observed in these systems, this fact leads to the conclusion that JTD should be the predominant effect.

1.3.3 The A_4C_{60} case

The A_4C_{60} compounds with A = K, Rb, Cs are systems in which the effects of electron interactions, crystal field, Jahn Teller distortions and Hund's rule coupling concur to yield a complex electronic behaviour.

From experimental data, as mentioned before, A_4C_{60} compounds presents a *bct* lattice arrangement and display an unconventional non magnetic insulating ground state [17, 19]. The phenomenology is further complicated by the observation in these systems of two band gaps, of respectively ~ 0.1 and ~ 0.5 eV [29, 27], and by the recovery of the metallic state in Rb_4C_{60} with the application of pressure [30].

Extensive theoretical investigations [25, 26, 24] agree with the fact that the overall behaviour can be explained only if both the correlations and the electron-phonon interaction are taken into account and concluded that A_4C_{60} are Mott-Jahn Teller insulators; the Mott-Hubbard transition justifies an insulating ground state, whereas the further (dynamical) JTD stabilises a non magnetic ground state and permits also to explain the presence of the two optical and spin gaps (see fig. 1.4).

1.4 Polymerisation in fullerenes and fullerides

Besides the interesting electronic properties, fullerene based materials display a rich variety of structural instabilities. Pristine C_{60} shows itself an *fcc-sc* structural transition, obtained simply by cooling the solid, because the decrease of the thermal excitation permits the fullerene molecules to find a more ordered orientation in the packing. But the most noticeable structural transitions are probably connected to the *polymerisation* of the buckyballs. Since the first indication of a polymerised C_{60} system [31], subsequent extensive investigations evidenced an huge variety of structures, either 1D or 2D or 3D dimensionally arranged [32, 33, 34].

1.4.1 Types of polymerisation

Despite this large family of compounds, C_{60} can polymerise essentially in only two ways: by a [2+2] *cycloaddition reaction* (Diels Alder reaction) which promotes the formation of four-membered carbon rings, shared by the neighbouring fullerene units; or by separated single C-C bonds. The cycloaddition is the most common process and characterises both undoped and doped systems (see below). Thermochemical studies [35], based on the use of semiempirical AM1 method and the Born Haber cycle, have shown that the choice between these two types of configurations strongly depends on

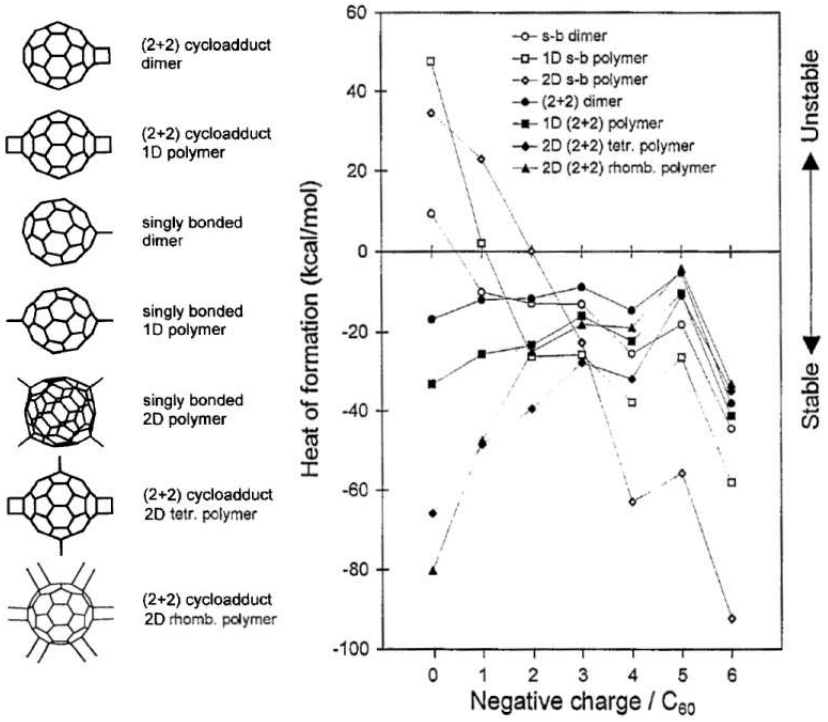

Figure 1.5: The enthalpy of polymerisation in function of the negative charge transfer on C_{60} for several known polymerised structures, either linked with [2+2] cycloaddition reaction or single C-C bond, calculated with thermochemical methods [35].

the effective charge transferred to C_{60}. In fig. 1.5 the calculated enthalpy of formation for several polymeric systems versus the anionic state of C_{60} is shown; it results that cycloaddition reaction leads to a compound which is always quite stable, but is energetically favoured in undoped or low-doped systems ($x < 3$). On the contrary, for higher doping range ($x > 3$) single C-C bond results the most stable configuration. The obtained values are in agreement with the experimentally observed systems.

1.4.2 Polymerisation in pristine C_{60}

Polymerisation in C_{60} can be realised with several methods: by photo-excitation, by molecular collision, by ionisation or by high pressure and high temperature treatments. It was observed the first time on laser irradiated thin fullerene films [31], in which oligomers insoluble in toluene were produced. Pure C_{60} always polymerises through [2+2] cycloaddition reaction, which necessitates an activation energy to occur and lead the system to a metastable state; usually a short and moderate annealing of the polymerised sample permits to replace the monomeric state. Putting C_{60} in extreme

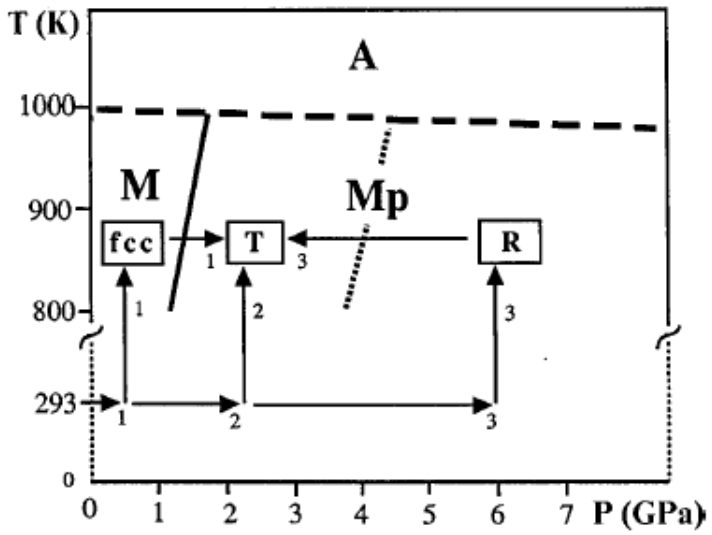

Figure 1.6: The phase diagram of pure polymerised C_{60} from [36]. **A** indicates the existence range of atomic carbon, due to the collapse of the C_{60} cage, **M** corresponds to the monomeric state. **Mp** is the range of polymerised C_{60}, both tetragonal (**T**) and rhombohedral (**R**).

thermal and pressure conditions ($T = 800 - 900$ K and $2 - 5$ GPa), yielded new interesting structural phases, as shown in the phase diagram of fig. 1.6. Substantially, three different isomers were observed: an orthorhombic 1D, a tetragonal 2D and 2D rhombohedral arranged polymers [33]. In particular, recently it has been noted that the rhombohedral structure also displays interesting magnetic properties; the compound presents ferromagnetic order up to 500 K [6]. The mechanism of this process, which is a break-down in the research of magnetism in carbon bases materials, is already under investigation.

1.4.3 Polymerisation in doped fullerides

Now we focus on the spontaneous polymerisation which is observed in the charged fullerides. Despite the "hard" chemistry requested to obtain pure polymerised C_{60}, just mixing fullerene with alkali atoms can promote spontaneous polymerisation between the charged buckyballs. Polymerised fullerides display generally an higher crystallinity, as compared with the other polymers, hence their structures can be studied in detail. Both systems characterised by four-membered carbon rings and separated single C-C bonds have been observed, and various dimensionalities were explored.

At the beginning, the first compound of this class which was discovered was KC_{60}

[37], which indeed displays a unusual rich phase diagram. The high temperature phase, isostructural to K_3C_{60}, undergoes a first order phase transition, in the $T = 350 - 400$ K temperature range. The study of the structure of this cooled phase evidenced that the nearest C_{60}-C_{60} distance is only 9.1 Å, even less than the external diameter of the buckyball. This distance is compatible with fullerenes linked by two covalent bonds, promoted by a [2+2] cycloaddition reaction. The polymerisation occurs along the face diagonals of the high-temperature *fcc* lattice and the orientation of the planes of the four-membered carbon rings can change in four different configurations, giving rise to different structural phases [5]. The 1D AC_{60} polymers, with A = K, Rb, Cs, are air-stable and good metals. If the high monomer phase is quenched at 77 K, it persists in the *fcc* arrangement up to 150 K, then dimerises. $(C_{60})_2^{2-}$ dimers are characterised by a single C-C bond between buckyballs, whose distance is 1.54 Å [5].

Polymerisation by single C-C bond occurs in some higher doped fullerides, when small alkali atoms are intercalated, like sodium. Na_2AC_{60}, with A = K, Rb, Cs, presents a high-temperature *fcc* phase; when they are cooled, a *fcc-sc* transition is observed. If the temperature is decreased slowly, 1D polymerisation with single C - C bonds takes place, and from ESR measurements it results that the polymeric phase is metallic [38, 39].

Polymerisation can also promote structures with higher dimensionality. In this context Na_4C_{60} is a very interesting system; it is a 2D polymer connected by single C-C bonds between the buckyballs and displays semi-metallic characteristics [40, 41]. This polymer is stable up to 500 K; above this temperature, the bonds break and a monomer *bct* structure forms. EPR measurements indicated that this phase could be metallic [42], despite the presence of four charges transferred to the buckyball; in fact, with these features, a non-magnetic insulating state should be expected (see sec. 1.3.3). A possible cause which permits to recovery a metallic state in this system was identified in the very low C_{60}-C_{60} distance of ~ 9.80 Å, as compared with the other A_4C_{60} compounds.

1.5 Lithium fullerides

Lithium doped fullerides Li_xC_{60} are among the less studied alkali doped fullerides; this probably because of the lack of superconducting behaviour of this class of compound, and the difficulties in their preparation. Indeed, lithium presents the lowest value of the vapour pressure as compared with the other alkali atoms (see later at sec. 5.3.1), and this gives some problems with the traditional techniques based of the evaporation

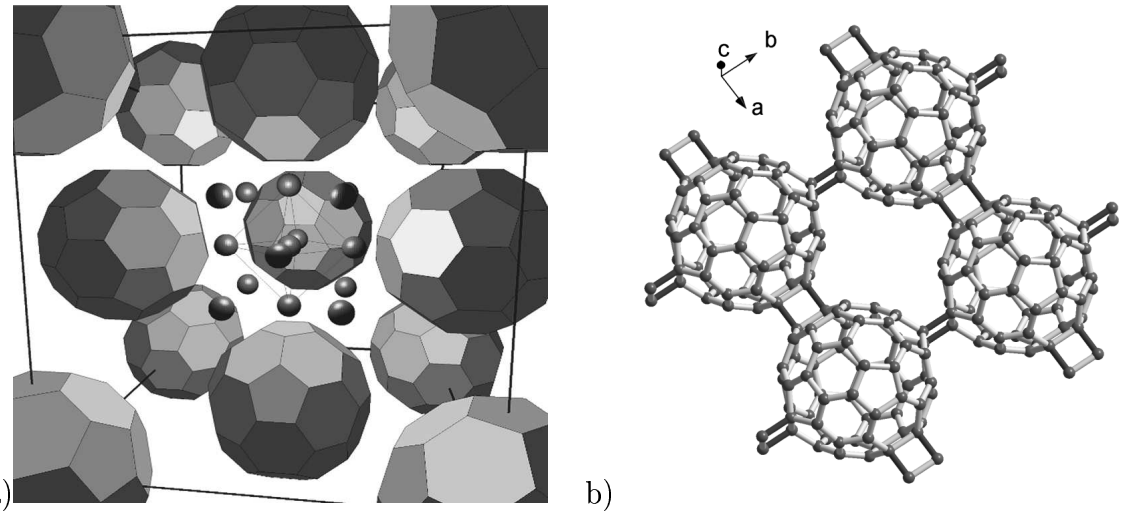

Figure 1.7: a) Lithium clusters in the high temperature (T > 550 K) phase of $Li_{12}C_{60}$ [10]. b) The 2D polimeric structure for Li_4C_{60} proposed by [11].

of the alkali in fullerene. Despite this, the interest on this systems started early, after the discover of superconductivity in K_3C_{60} [7]; then theoretical studied based on the Car-Parrinello method and experimental observations on molecular beams indicated the possibility of formation of the *superfulleroid* structure $Li_{12}C_{60}$. Here the 12 lithium atoms coordinate with the 12 pentagons of the buckyball, leading to the formation of a charged highly symmetric molecule, with electron population in the derived-t_{1u} degenerate orbitals. The conservation of the degeneracy of the frontier orbitals has been already indicated as an essential ingredient to obtain a metallic phase in the fullerides, which are systems very close to a metal-to-insulator transition (see par. 1.3.1); hence this could be also a promise of superconducting behaviour. But the bulk state of the superfulleroid structure was never observed. On the contrary, the research on Li doped fullerides has shown other interesting features of this class of compound:

- A very high doping level can be reached as compared with the other alkali doped fullerides: thanks to the small lithium dimensions up to 30 Li atoms per C_{60} unit can be accommodated in the host structure. When the doping is sufficiently high ($x > 7$) lithium tends to clusterize (fig. 1.7a). Confirmation of this behaviour comes from high resolution x-ray measurements [10] and Multiple Quantum NMR [43], performed on the systems with $x = 12$ and $x = 15$ at high temperature ($T > 550$ K); lithium clusters are located in the biggest octahedral voids of the *fcc* fullerenic matrix and show only a weak interaction with the carbons of the cage, as proved by the absence of J couplings among ^{7}Li and ^{13}C and the

considerable ^{7}Li motional narrowing in the NMR spectrum.

- The tendency of lithium of promote covalent Li^+-C interaction and hence to reduce the effective charge transfer on C_{60}. The very interesting system Li_xCsC_{60} with $x = 1.5-6$ are all characterised by a *fcc* structure, which guarantees the degeneracy of the frontier orbitals, and are metallic. Nevertheless, the stoichiometry $x = 2$, which should correspond to nominally 3 el/C_{60} *does not* result superconductive, whereas the recovery of the superconducting behaviour is obtained for $x = 3$, when the effective half band filling is reached [8].

- The formation of polymerised structure in the less doped systems. Due to the small steric hindrance and the concomitant presence of an *electrostatic pressure*, charge transfer salts Li_xC_{60} undergo polymerisation of fullerene units. Studies which started from low resolution x-ray data have identified some polymerised phases, either 2D trigonal and 2D tetragonal, depending on lithium stoichiometry, even if the results show some discrepancies [9, 11]. It was proposed that fullerenes link through [2+2] cycloaddition bonds, as in the tetragonal and rhombohedral pure polymerised C_{60} phases (see fig. 1.7b).

1.6 Ammoniated fullerides

An important class of fullerene compounds is represented by the ammoniated phases of alkali doped fullerides. The introduction of molecular ammonia in the interstices of the host fulleride lattice leads generally to the complexation of the metal cations; the basic effect of this intercalation is the simple *isotropic expansion* of the lattice, which sometimes can be easily controlled by varying the ammonia amount in the sample. However, as already stressed, due to the high correlated state of alkali fullerides, the consequences of a similar topological change can be dramatic: this is the case, for example, of $(NH_3)_4Na_2CsC_{60}$ [45], in which the $(NH_3)_4$-Na complex is located into the octahedral void of the *fcc* lattice. After the intercalation of ammonia, the cubic symmetry and the metallic behaviour of the original structure is retained, but the expansion of the cell yields to an high enhance of the superconducting critical temperature from $T_c = 12$ K of Na_2CsC_{60} ($a = 14.126$ Å) to $T_c = 30$ K of the ammoniated phase ($a = 14.473$ Å)[1]. The mechanism of such a behaviour can easily described in the framework of the *BCS theory*. In the weak coupling limit $\lambda \ll 1$, the critical

[1]However, other subsequent experiments, performed by other research groups, did not provide a confirmation of this effect.

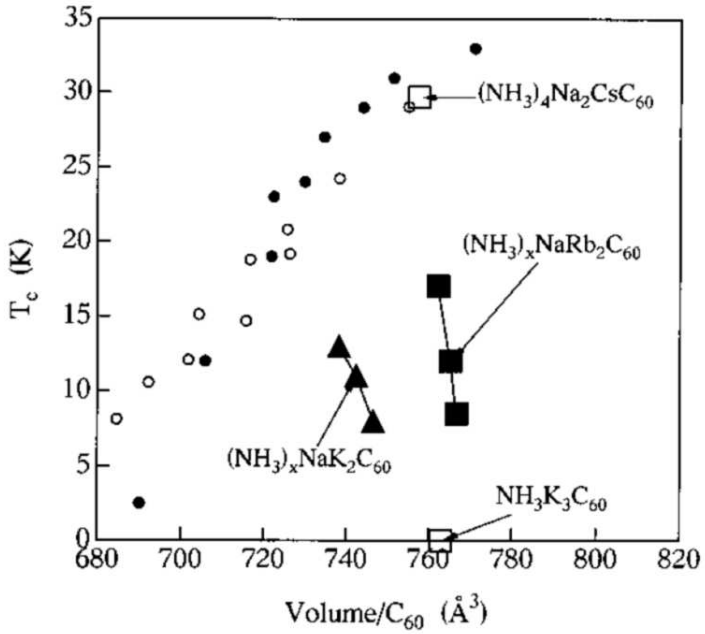

Figure 1.8: Variation of T_c with the unit cell volume for some ammoniated fullerides, compared with values obtained for other A_3C_{60} systems [44].

temperature T_c is expressed by:

$$T_c \propto \omega_0 \exp -1/\lambda \tag{1.2}$$

where ω_0 is the average phonon frequency [5]. On the other hand, $\lambda = N(E_F) \cdot V$, where $N(E_F)$ is the density of states at the Fermi energy, and V the BCS interaction energy. Now, the chemical expansion induced by ammonia molecules provokes a *narrowing* of the electronic bands, and a subsequent *increase* of the density of state; from eq. 1.2, this effect yields an increase of T_c.

A totally different behaviour is shown by the $(NH_3)_xNaA_2C_{60}$ phases ($x \sim 1$, A = K, Rb) [46]. In this case the compounds do not form in absence of the ammonia; the linear Na-NH_3 complexes are placed in the octahedral site of the *fcc* lattice, and result disordered over the eight equivalent [1 1 1] directions. Even in this case the compound is metallic and displays superconducting transition, but the T_c value is much lower than expected from the comparison with the other fullerene systems, as shown in fig. 1.8. The lattice parameter can easily change by varying the ammonia doping, but in this case, an *opposite* correlation (with respect to eq. 1.2) between the lattice parameter and T_c is observed. This deviation from the classical BCS/Eliashberg theory was first

referred to the disorder induced by the off-centering position of the Na^+ cations, then by the presence of weak H bonds between ammonia and the buckyballs, but it is still investigated [46, 47, 48]. When $x \sim 2$ a metal-to-insulator transition occurs [49].

Due to the symmetry mismatch between the fullerene packing and the geometry of the complexed cation, presence of ammonia in the host lattice can sometimes induce important structural changes in the compound, which obviously reflect also in its electronic properties. Intercalation of K_3C_{60} with NH_3 lead to the body centered orthorhombic $NH_3K_3C_{60}$ phase [44, 4, 16]; the loss of the cubic symmetry, and hence the degeneration of the frontier orbitals, produces the suppression of superconductivity, even if the metallic character is retained down to 40 K. Below this temperature, a metal-to-insulator transition leads to a insulating ground state with an antiferromagnetic order.

Chapter 2

X-ray diffraction techniques

Introduction

This chapter provides a description of x-ray diffraction techniques, in particular powder x-ray diffraction, which was the main tool of investigation of this work. After a recall of several theoretical concepts (sec. 2.1), the discussion focuses on the setup of a x-ray experiment, whith particular regard to the sources, both conventional generators and synchrotrons (sec. 2.2). Then the attention concentrates on the powder diffraction experiment (sec. 2.3). Finally, the main features of the instruments used in this work are given (sec. 2.4).

2.1 X-ray diffraction

The main bases of cristallography were posed at the beginning of the twentieth century, after the discovery of x-rays by Roentgen in 1896. In 1912 von Laue indicated the x-rays as the natural radiation for investigate the structure of crystals. In 1913 Bragg and von Laue managed to describe the structure of NaCl, KCl, KBr and KI starting from the analysis of their x-ray patterns.

The power of this tool of investigation, which became quickly one of the most important instruments of the research in the physic of the materials, is due to the fact that x-rays possess a wavelength comparable with the standard atomic and molecular distances, of the order of $\sim$ 1 Å; the second essential ingredient is the presence of a *lattice*, a regular and periodic arrangement of scattering units. When a coherent x-ray wave front bears upon a lattice, part of the radiation is elastically reflected by the atoms, giving rise to a macroscopic effect of interference, which is improperly

named *diffraction*. The two main effects which take part to this phenomenon are *Thomson scattering*, which represents the coherent contribution to the scattering, and the *Compton scattering*, which on the contrary represents the incoherent contribution.

2.1.1 Coherent and incoherent scattering

Considering a plane monocromatic wave, its electric field is described by the equation:

$$\mathbf{E}_i = \mathbf{E}_{0i} \exp 2\pi i\nu \, (t - x/c) \tag{2.1}$$

$\mathbf{E}_{i0}$ is the amplitude of the wave and $\mathbf{E}_i$ is the value of the field at the time t and position x. When the wave interacts with a charged particle, the latter starts to oscillate, excited by the Lorentz force, and it irradiates an electromagnetic field as a classical dipole. In an orthogonal system centred on the particle, the electric field of the scattered radiation at the point Q in the space lying in the plane (x, y), at the distance r from the origin O (see fig. 2.1), is:

$$\mathbf{E}_d = \mathbf{E}_{0d} \exp \left[2\pi i\nu \, (t - x/c) - i\alpha\right] \tag{2.2}$$

where α is the phase delay between the incident wave and the emitted wave, due to the impedance of the system.

From considerations of classical electromagnetism it is possible to demonstrate that $\mathbf{E}_{0d}$ lies on the plane (x, y) and is expressed by the formula [50]:

$$\mathbf{E}_{0d} = \frac{1}{r}\mathbf{E}_{0i}(e^2/mc^2) \sin\varphi \tag{2.3}$$

where φ is the angle formed by the direction of oscillation of the particle and the direction of the observation. In general, the incident radiation is not polarized, but it is a superimposition of two orthogonal totally polarized components. Only for radiation with electric field in the plane (x, y) the emitted wave will depend on the parameter φ, otherwise, if the electric field is orthogonal to the plane, always $\varphi = 90°$. In general, for an incident wave, in which K_1 part has the electric field orthogonal to the plane of observation, and K_2 part parallel, the intensity of the scattered radiation in Q is:

$$I_s = I_i \frac{e^4}{m^2 r^2 c^4}(K_1 + K_2 cos^2 2\theta) \tag{2.4}$$

where I_i is the incident and I_s is the scattered intensity. Of course, if the wave is totally

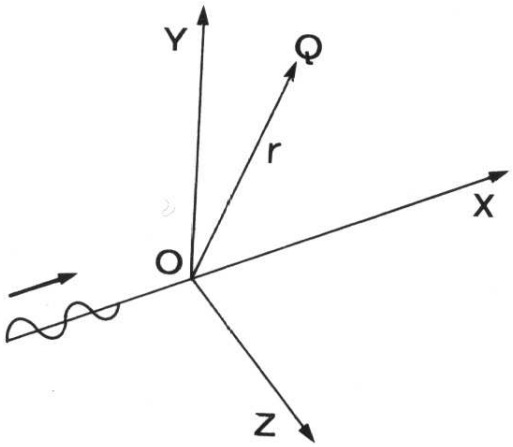

Figure 2.1: A schematic representation of the Thomson scattering.

unpolarized, $K_1 = K_2 = \frac{1}{2}$ and:

$$I_s = I_i \frac{e^4}{m^2 r^2 c^4} (\frac{1 + cos^2 2\theta}{2}) \tag{2.5}$$

The factor $\frac{1+cos^2 2\theta}{2}$ is called *polarization factor*. This means that, for unpolarised incident beam, the intensity of the diffused radiation is maximum in the direction of the incident wave and minimum in the orthogonal direction.

The elastic Thomson scattering is responsible of the diffraction phenomenon, because in this process the diffused radiation maintains a *well defined* phase relation with the incident beam; in other words, it is a *coherent* process. But in the scattering process there is also a non negligible contribution from *incoherent* radiation, which could mainly be ascribed to Compton scattering. In this case the radiation is not elastically diffused, but loses part of its energy during the interaction with the charge particle. The emergent radiation has no more a definite phase relation with the incident one, and its wavelength is weakly changed according to the equation [50]:

$$\Delta\lambda(\text{Å}) = 0.024(1 - \cos 2\theta) \tag{2.6}$$

The maximum value of $\Delta\lambda$ is reached in back-scattering configuration. The Compton

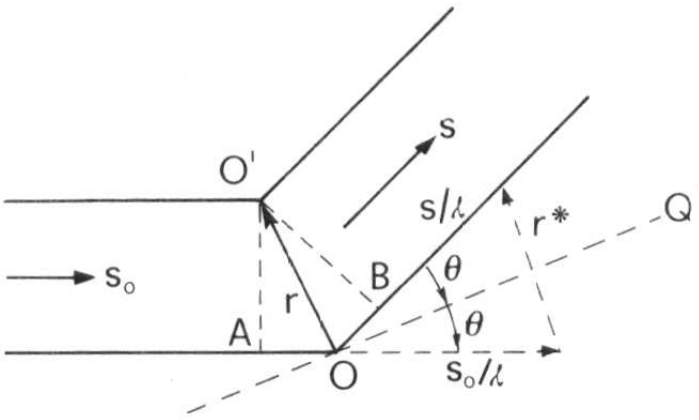

Figure 2.2: The plane wave with unit vector $\mathbf{s}_0$ is scattered by the centres O and O'. The distance $\mathbf{r}$ between the two centres, the scattered wave, whose unit vector is $\mathbf{s}$, and the difference vector $\mathbf{r}^*$ are also shown.

scattering contributes on the increase of the background signal.

2.1.2 Interference of scattered waves

As we already stressed, x-ray diffraction is actually an interference effect of the scattered waves from a ordered ensemble of atoms or molecules. Let's consider a couple of scattering centres positioned in O and O' as in fig. 2.2:

A plane wave, whose unit vector associated with its direction of propagation is $\mathbf{s}_0$, hit them and the observator focuses on the radiation diffused in the $\mathbf{s}$ direction. The phase difference between the two waves scattered in O and O' is:

$$\delta = \frac{2\pi}{\lambda}(\mathbf{s} - \mathbf{s}_0) \cdot \mathbf{r} = 2\pi \mathbf{r}^* \cdot \mathbf{r} \tag{2.7}$$

where $\mathbf{r}* = \frac{1}{\lambda}(\mathbf{s} - \mathbf{s}_0) = (2\sin\theta/\lambda)\,\hat{\mathbf{r}}^*$ is the difference vector. If λ is much greater than r, then the phase difference is very small, and no interference phenomena will occur.

The wave scattered by O and O' has the same form of eq. 2.3. It can be assumed that the atoms in the lattice do not change their position during the time, and the values measured during the diffraction experiment are *mean* values of the time; hence, the dependence from t drops out. Putting O in the centre of the reference frame, the wave scattered by O' along the $\mathbf{s}$ direction is then given by:

$$F(\mathbf{r}^*)_{O'} = A_{O'} \exp(2\pi i \mathbf{r}^* \cdot \mathbf{r}) \tag{2.8}$$

where $A_{O'}$ is the amplitude. If there are N scattering points, each in the position $\mathbf{r}_j$ with respect to O, the *total amplitude* in the $\mathbf{s}$ direction is the superimposition of all the contributions:

$$F(\mathbf{r}^*) = \sum_{j=1}^{N} A_j \exp(2\pi i \mathbf{r}^* \cdot \mathbf{r}_j) \tag{2.9}$$

where A_j is the amplitude of the wave scattered by the j-th scatterer.

Focussing now on the intensity I, it is convenient to refer to the intensity I_{eTh} scattered by the free electron, thus defining the ratio I/I_{eTh} as f^2, where f is the *scattering factor* of the object; actually, it represents the density of the scattering particle. For a *continuum* of scattering centres, by defining $\rho(\mathbf{r})$ as the electron density in the volume $d\mathbf{r}$, we obtain for $F(\mathbf{r}^*)$ the expression:

$$F(\mathbf{r}^*) = \int_V \rho(\mathbf{r}) \exp(2\pi i \mathbf{r}^* \cdot \mathbf{r}) d\mathbf{r} = T\left[\rho(\mathbf{r})\right] \tag{2.10}$$

where T is the Fourier transform operator. This means that *the amplitude of the wave scattered from a continuum of scattering centres is the Fourier transform of the density of the scatterers.* The vector $\mathbf{r}^*$ defines a new space which is called *reciprocal space.* The knowledge of the modulus and the phase of the scattered amplitudes allows to unequivocally define the density of scatterers; nevertheless, this knowledge is in practice never complete and generally an experiment of x-ray diffraction permits to obtain information only about the modulus of $F(\mathbf{r}^*)$.

2.1.3 Scattering by atoms, molecules and crystals

Atomic form factor

The main scattering centres in a sample which undergoes x-ray diffraction are the electrons, whose mass is ~ 2000 times less than proton (see eq. **??**). When an electron is bonded to an atom, the probability distribution $\rho_e(\mathbf{r})$ in the space is represented by the modulus of its Schroedinger wave function $\psi(\mathbf{r})$:

$$\rho_e(\mathbf{r}) = |\psi(\mathbf{r})|^2 \tag{2.11}$$

The *electron scattering factor* for an atomic electron is:

$$f_e(\mathbf{r}^*) = \int_V \rho_e(\mathbf{r}) \exp(2\pi i \mathbf{r}^* \cdot \mathbf{r}) d\mathbf{r} \tag{2.12}$$

V being the region of the space in which $|\psi(\mathbf{r})|^2 \neq 0$. In the case of an electron in an atom, it is reasonable to assume that $\rho_e(\mathbf{r})$ has spherical symmetry (rigorously true for s electrons). In this case [50]:

$$f_e(r^*) = \int_S U_e(r) \frac{\sin 2\pi r r^*}{2\pi r r^*} dr \tag{2.13}$$

where $U_e(r) = 4\pi r^2 \rho_e(r)$ is the radial distribution, and S the volume of the integrating sphere.

Considering now the whole atom, the atomic probability distribution is the sum of the contributions of all electrons:

$$\rho_a(r) = \sum_{j=1}^{Z} \rho_{ej} \tag{2.14}$$

and the Fourier transform of $\rho_a(r)$ is called the *atomic scattering factor*, denoted by f_a. In general, $\rho_a(r)$ does not show spherical symmetry, but, in first approximation, the deviation from it can be neglected and one can use an equation analogous to 2.13.

Molecular form factor

The next step consists in calculating the scattering factor of an *ensemble* of atoms, which can be a molecule or a unit cell in a crystal; if the j-th atom is located at the position $\mathbf{r}_j$, its electron density is $\rho_j(\mathbf{r} - \mathbf{r}_j)$ and the amplitude of the scattered wave is:

$$F_M(\mathbf{r}^*) = \int_S \sum_{j=1}^{N} \rho_j(\mathbf{r} - \mathbf{r}_j) \exp(2\pi i \mathbf{r}^* \cdot \mathbf{r}) dr = \sum_{j=1}^{N} \int_S \rho_j(\mathbf{R}_j) \exp(2\pi i r^* \cdot (\mathbf{r}_j + \mathbf{R}_j) d\mathbf{R}_j$$

$$= \sum_{j=1}^{N} F_j(\mathbf{r}^*) \exp(2\pi i \mathbf{r}^* \cdot \mathbf{r}_j) \tag{2.15}$$

where $F_j(\mathbf{r}^*)$ is the atomic scattering factor of the j-th atom and $\mathbf{R}_j = \mathbf{r} - \mathbf{r}_j$.

Sometimes, molecules in a crystal are not fixed, but can present a rotating motion about their centre of gravity; it is the case, for example, of fullerene C_{60} in the plastic state. In this case, approximations must be done, in order to represent their effective scattering factor $F_M(\mathbf{r}^*)$, which results in this case necessary different from that of the static case in eq. 2.15. Roughly approximations, which generally work quite well for fullerene systems, consist in representing the overall electronic density of the mole-

cule with symmetric distributions, as, for example, dense spheres of spherical shells. However, extensive studies [51] demonstrated that the dynamic electronic density $\rho(\mathbf{r})$ of the librating molecule must satisfy precise constraints, deriving both from the corresponding static distribution $\sigma(\mathbf{r})$ and the lattice symmetries. In Appendix A this analytical method used to treat librating molecules is discussed in more detail.

Structure factor

As known, a crystal is a regular periodic arrangement of unit cells. The mathematical representation of a lattice is given by:

$$L(\mathbf{r}) = \sum_{u,v,w=-\infty}^{+\infty} \delta(\mathbf{r} - \mathbf{r}_{u,v,w}) \tag{2.16}$$

where δ is the *Dirac delta function* and $\mathbf{r}_{u,v,w} = u\mathbf{a} + v\mathbf{b} + w\mathbf{c}$ (with u, v, w integers) is a vector of the lattice [50]. If $\rho_M(\mathbf{r})$ represents the electronic density of the unit cell, the electron density of the whole crystal is obtained by the *convolution*:

$$\rho_\infty(\mathbf{r}) = \rho_M(\mathbf{r}) * L(\mathbf{r}) \tag{2.17}$$

In the reciprocal space, the amplitude of the wave diffracted by the crystal is:

$$\begin{aligned} F_\infty(\mathbf{r}^*) &= T[\rho_M(\mathbf{r})] \cdot T[L(\mathbf{r})] \\ &= F_M(\mathbf{r}^*) \cdot \frac{1}{V} \sum_{h,k,l=-\infty}^{+\infty} \delta(\mathbf{r}^* - \mathbf{r}^*_{\mathbf{H}}) \\ &= \frac{1}{V} F_M(\mathbf{H}) \sum_{h,k,l=-\infty}^{+\infty} \delta(\mathbf{r}^* - \mathbf{r}^*_{\mathbf{H}}) \end{aligned} \tag{2.18}$$

where V is the volume of the cell and $\mathbf{r}^*_{\mathbf{H}} = h\mathbf{a}^* + k\mathbf{b}^* + l\mathbf{c}^*$ is a generic vector of the reciprocal lattice. Hence, in the presence of a lattice, the amplitude of the scattered radiation is non-zero only when $\mathbf{r}^*$ is equal to a vector of the reciprocal space. The value $\frac{1}{V}F_M(\mathbf{H})$ is a specific weight of the corresponndig measured intensity[1].

The dimensions of the crystal is obviously finite, and, if it is sufficiently small, the

[1] From the eq. 2.18 it is possible to obtain also the *Laue* conditions. In fact, the Dirac delta function imposes $\mathbf{r}^* = \mathbf{r}^*_{\mathbf{H}}$. Remembering the eq. 2.7 and multiplying scalarly per $\mathbf{a}$, $\mathbf{b}$ and $\mathbf{c}$, it is possible to obtain:

$$\mathbf{a} \cdot (\mathbf{s} - \mathbf{s}_0) = h\lambda \quad \mathbf{b} \cdot (\mathbf{s} - \mathbf{s}_0) = k\lambda \quad \mathbf{b} \cdot (\mathbf{s} - \mathbf{s}_0) = k\lambda$$

finiteness of the lattice can produce effects on the diffracted image. One can easily take into account these aspects by introducing a form function $\Phi(r)$, which is $= 1$ inside the crystal and $= 0$ outside. The electronic density of the crystal is then:

$$\rho_{cr} = \rho_{\infty}(\mathbf{r}) \cdot \Phi(\mathbf{r}) \tag{2.19}$$

and the new amplitude of the scattered wave becomes:

$$F(\mathbf{r}^*) = \frac{1}{V} F_M(\mathbf{H}) \sum_{u,v,w=-\infty}^{+\infty} D(\mathbf{r}^* - \mathbf{r}^*_{\mathbf{H}}) \tag{2.20}$$

where the distribution function D is the Fourier transform of the measure of the crystal.

The function $F_M(\mathbf{H})$ represent the *structure factor* and is expressed by the equation:

$$F_{\mathbf{H}} = \sum_{j=1}^{N} \exp(2\pi i \mathbf{r}^*_H \cdot \mathbf{r}_j) \tag{2.21}$$

where N is the number of atoms of the unit cell. It is in general a complex number.

2.1.4 The temperature factor

In a real crystal, atoms residing in their crystallographic positions are not fixed, but move around their equilibrium point, which correspond to the minimum of their potential energy; the motion is due to the thermal excitation. This gives rise to modifications of the intensity of the scattered waves, through the so called *Debye-Waller factor*.

If a thermally excited atom is considered, it is possible to define $p(\mathbf{r}')$ as the probability of finding the atom in $\mathbf{r}'$, and $\rho_a(\mathbf{r} - \mathbf{r}')$ as the electronic density in $\mathbf{r}$ when the atom is in $\mathbf{r}'$. The effective electronic density is obtained integrating all the contributions when the atom explores the whole volume S' during its motion:

$$\rho_{at}(\mathbf{r}) = \int_{S'} \rho_a(\mathbf{r} - \mathbf{r}') p(\mathbf{r}') d\mathbf{r}' = \rho_a(\mathbf{r}') * p(\mathbf{r}') \tag{2.22}$$

In the reciprocal space the convolution becomes a product:

$$f_{at}(\mathbf{r}^*) = f_a(\mathbf{r}^*) \cdot q(\mathbf{r}^*) \tag{2.23}$$

where $f(\mathbf{r}^*)$ is the atomic scattering factor of the fixed atom and $q(\mathbf{r}^*) = \int_{S'} p(\mathbf{r}') \exp(2\pi i \mathbf{r}^* \cdot$

$\mathbf{r}')d\mathbf{r}'$ is the *Debye-waller factor*. The probability function $p(\mathbf{r}')$ depends directly on the temperature, and inversely on the atomic mass and the strength of the bonds. For this reason it is in general anisotropic, but it can be assumed isotropic, for simplicity; in that case it can be approximated by a Gaussian function:

$$p(\mathbf{r}') = (2\pi)^{-1/2} U^{-1/2} \exp\left[-(\mathbf{r}'^2/2U)\right] \tag{2.24}$$

where $U = \langle r^2 \rangle$ is the mean shift of the atom with respect the equilibrium position. The corresponding Fourier transform is:

$$q(\mathbf{r}^*) = \exp(-B \sin^2\theta/\lambda^2) \tag{2.25}$$

where $B = 8\pi^2 U$ is the atomic temperature factor (measured in Å). Typical values of $\sqrt{U}$ are $0.05 \div 0.20$ Å for inorganic crystals, up to 0.5 Å for organic crystals [50]. The effect of the Debye Waller factor is to make the electronic density more diffuse and hence to reduce the scattering intensities for higher values of $\sin\theta/\lambda = |\mathbf{r}^*|$.

2.2 Experimental set-up in x-ray diffraction

This section focuses on the experimental instruments used for the x-ray production, both conventional generators and synchrotrons, and gives some information about the optical methods able to obtain a suitable x-ray beam on the specimen, necessary to produce diffraction, and the x-ray detectors.

2.2.1 X-ray sources

Conventional generators

To produce a flux of x-rays it is necessary to irradiate with energetic charged particles, for example electrons, a target of a specific material. The electrons, during the impact on the target, change quickly their velocity, and consequently emit a typical *bremmstrahlung* continuous electromagnetic spectrum. Moreover, if their kinetic energy is enough, they can also ionise the atoms of the target, and induce electronic transitions of the inner shells, thus promoting a superimposed *characteristic spectrum*: this consists of very narrow and intense peaks, whose spectral positions depend on the atomic species involved in the ionisation process. The two main typologies of conventional x-ray generators are the *sealed tubes* and the *rotating-anode generators*, and both are

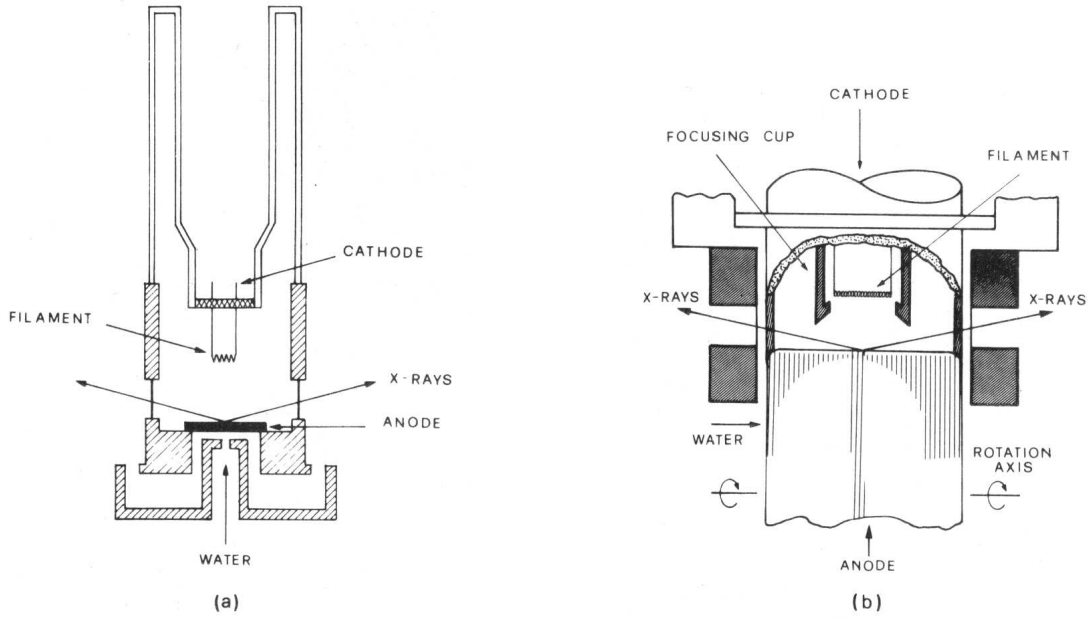

Figure 2.3: The schematic representation of a) a sealed-tube generator and b) a rotating anode generator for x-rays.

based on the phenomenon depicted above.

In particular, in the sealed-tube (see fig. 2.3a) electrons are produced by a cathode, which is a hot filament maintained at a high potential difference (usually several tents of KVolts) with respect to the anode; this consist of a metallic target, cooled by a refrigerant. The material of the anode is conventionally copper, or molybdenum. In the tube high vacuum level is required, otherwise the efficiency of x-ray production is dramatically reduced. The x-rays emitted by the anode reach the outside of the tube, passing through a beryllium window; beryllium is a very toxic element, but it is almost transparent to x radiation, due to its small atomic number.

In rotating-anode generators the geometry is practically the same, but the main difference is the conformation of the anode, which is cylindrical and can rotate around its axis. This permit to reach higher emitted energies than in a sealed-tube, because the target area is continuously changed, but at the same time introduces many mechanical difficulties, especially due to the high vacuum manteinance (see fig. 2.3b).

Choice of the radiation

As written before, the emitted x-ray radiation consists of two contribution, the first continuous, the second discrete. In a x-ray experiment the more useful is the second

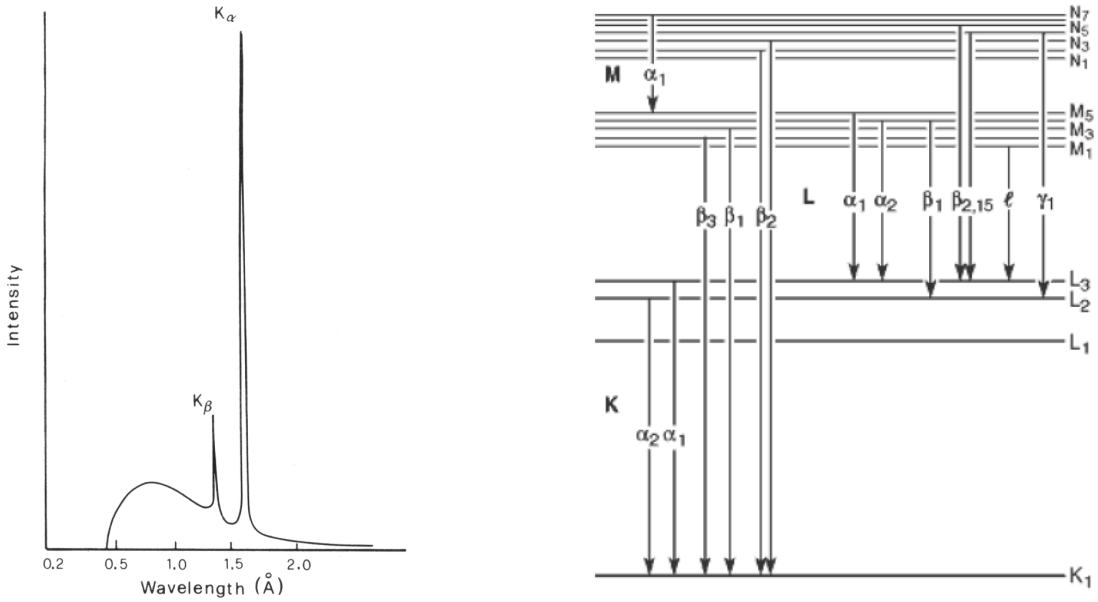

Figure 2.4: a) The intensity of the radiation emitted by a copper cathode, as a function of the wavelength. The two contributions of breemstrahlung (background) and the characteristic lines of K_α and K_β(sharp peaks) are well visible. b) Transitions which give rise to the various emission lines.

one, because the *characteristic* peaks are much more intense (of a factor ten) than the bremmstrahlung contribution (see fig. 2.4a); this, on the contrary, is a sort of background. The characteristic lines are called K, L, M, etc. and correspond to the electronic transitions from higher energy orbitals to respectively n=1,2,3... shells. Of course not all the transitions are permitted, due to the presence of selection rules. In particular, if the two orbitals involved in the transition are close, the line is labelled with α, if they are separated by another shell it is indicated with β. A further integer number indicates which orbital is involved in the transition, as shown in the fig. 2.4b.

The x-ray photon energy is obviously the difference of the energy of the two levels involved in the transition, and depends on the element which has been considered. For a given transition, the frequency can be obtained by the *Moseley's law*:

$$\nu = C(Z - \sigma)^2 \tag{2.26}$$

where C and σ are constants, while Z is the atomic number of the atomic species considered. Two very common transitions lines are the K_α of Copper ($Z = 29$) and Molybdenum ($Z = 42$), whose correspondent emitted radiations have the typical wave-

length respectively $\lambda = 1.5418$ Å and $\lambda = 0.7107$ Å. The intensity of a characteristic K line is expressed by the equation [50]:

$$I_K = B \cdot i \cdot (V - V_K)^{1.5} \tag{2.27}$$

where B is a constant, i is the electrical current, V_K is the excitation potential of the K series, strictly related to the ionisation energy of the atom, and V is the working potential. It can be shown that the highest ratio I_K/I_W, where I_W is the total bremmstrahlung energy, is obtained when $V = 4 \cdot V_K$; for copper $V_K = 8.981$ KV, hence the normal working potential of an x-ray generator is about 40 KV.

The choice of the best type of radiation, related to the characteristics K_α lines of the metals which are normally used as target, depends on several factors; on one hand, for a given geometry of the experimental set-up, the diffracted peaks will result more resolved on the detector if a longer wavelength is used. On the other hand, the larger is the wavelength, the weaker is the sensitivity of the x-ray probe to the molecular structure. A compromise between these two opposite phenomena leads to prefer copper when the structure displays large unit cell parameters, as in macromolecular systems, and molybdenum for the inorganic materials. Moreover, the use of a radiation rather than another depends on the presence of atoms in the specimen which display strong absorption in that range of frequencies.

Synchrotron light

The "state of the art" of x-ray diffraction is now reached in the *synchrotron radiation facilities*. A synchrotron is an installation in which electrons or positrons are accelerated at relativistic velocities and forced to a circular trajectory by magnetic fields ("bending magnets") inside a toroidal cavity ("storage ring") of several tenth meters of radius, in which high vacuum is maintained. During their accelerated motion, they emit in a wide frequency range, and also in the x-ray band. The essential structure of a synchrotron facility consists of a *linear accelerator* (LINAC), a *booster* in which the electrons are pre-accelerated, and finally the *storage ring*, in which the charged particles are maintained at a velocity constant in modulus through a radio-frequency cavity system synchronised with their motion (see fig. 2.5a). Along the ring there are several "windows", from which the synchrotron radiation can be extracted and guided by an optical system along the experimental apparatus, the *beam-line*; this is placed tangentially to the particles' trajectory; in a modern synchrotron there may be $20 - 50$ beam-lines, each designed for different experiments.

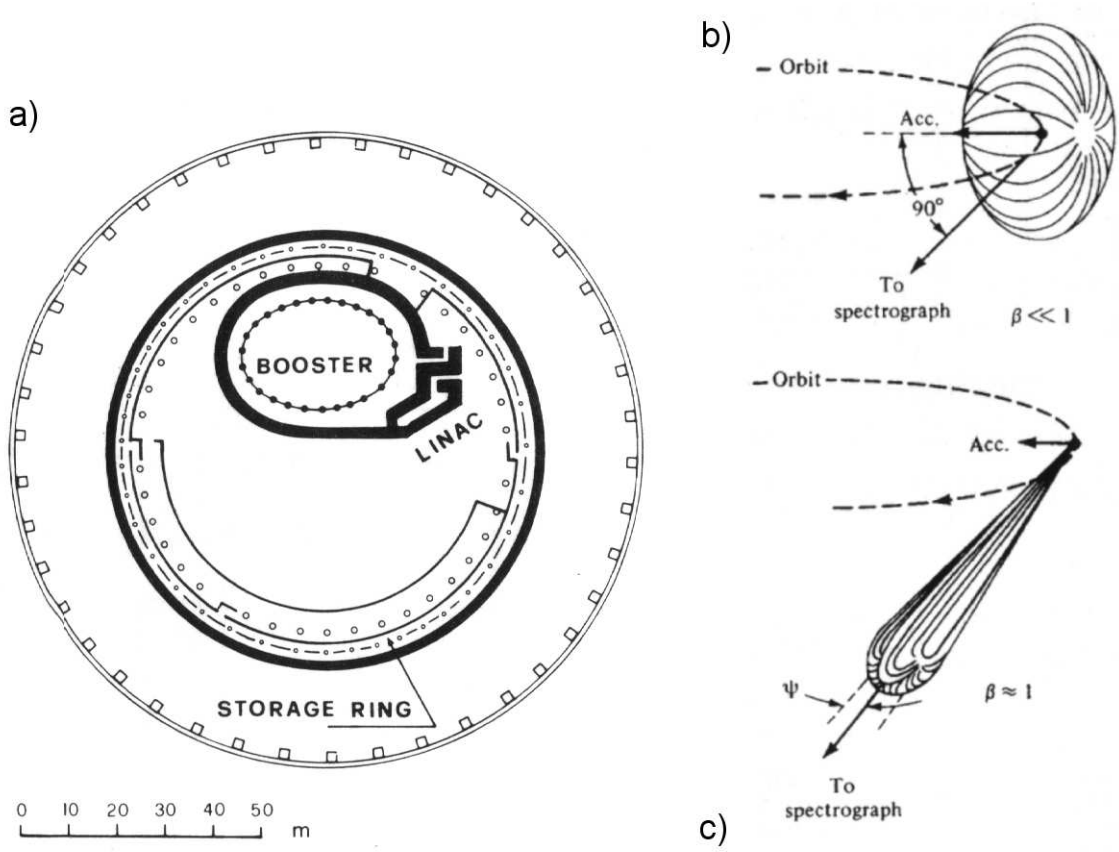

Figure 2.5: a) the scheme of a synchrotron. b) Radiation emitted by a charge which moves along a circumference. c) Radiation emitted by the same charge when $v \sim c$.

The radiation emitted by a moving charged particle which describes a circle is similar to one of an oscillating dipole with the maximum of intensity in the direction perpendicular to the acceleration (see fig. 2.5b). But, due to the relativistic velocities of the particles, the produced radiation becomes strongly anisotropic and emitted along a narrow cone parallel to the instantaneous velocity (see fig. 2.5c).

The power of the electromagnetic radiation for a single charged particle is given by the Schwinger's formula [52]:

$$P = \frac{2e^2cE^4}{3R^2(m_0c^2)^4} = \frac{2e^2c\gamma^4}{3R^2} \tag{2.28}$$

where $\gamma = \frac{mc^2}{m_0c^2}$. The radiation is emitted in a cone, whose the opening angle is $\Delta\psi \approx 1/\gamma$ (because of the relativistic effects). Hence, the total power emitted by the ring is obtained by multiplying for the number of particles and by dividing for the time

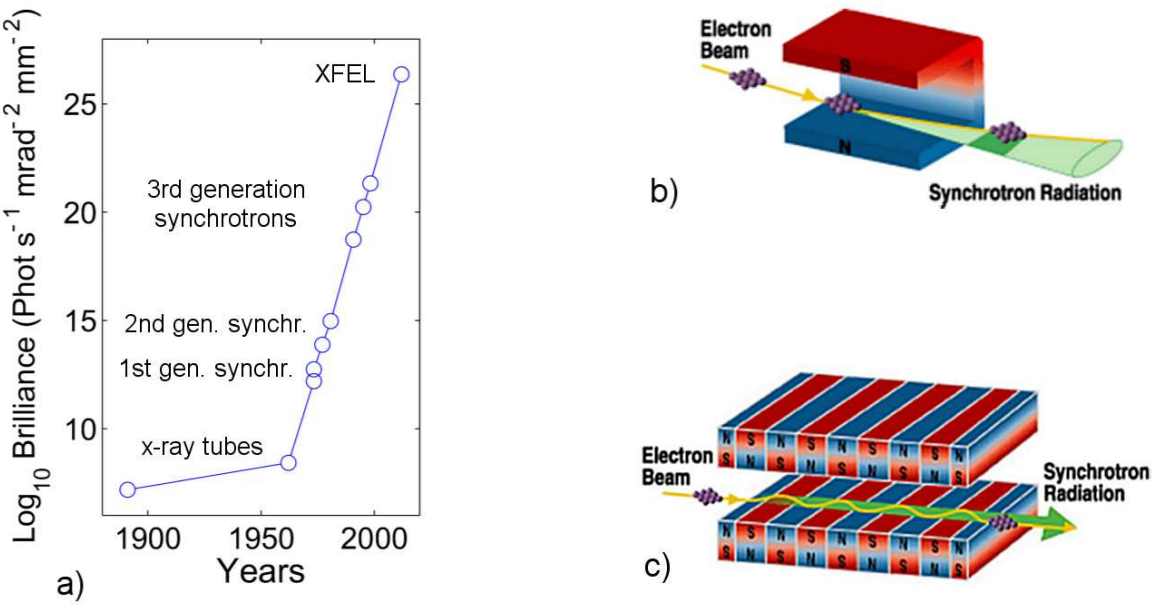

Figure 2.6: a) The brilliance of several x-ray generators in the twentieth century. b) Illustration of a bending magnet and c) of an insertion device.

taken during a complete revolution. It can be shown that this value is $P_{tot} = 26.6E^3Bi$ and hence is proportionally to the current of the storage ring.

A very important parameter which characterises the synchrotron light is the *brightness* or *brilliance*: this is linearly proportional to the emitted flux F (and hence proportional to P), and inversely proportional to the source size and the angular spreads. This quantity makes the difference with the other conventional sources and guarantees also the high coherence of the emitted radiation; for example, for the x-rays the brilliance of the synchrotron light is up to ten order of magnitude greater than an x-ray tube (see fig. 2.6a).

To improve the emission power and the brilliance, the radiation emitted in a modern synchrotron is actually extracted in correspondence of the maximum acceleration of the particles: for example in the proximity of a *bending magnet* (see fig. 2.6b); the spectrum of the radiation generated by a bending magnet is characterised by a rather broad curve. But also other devices, called *insertion devices*, can be intentionally inserted in the storage ring to provide a further enhancement. They consist in an array of small magnets (see fig. 2.6c) alternately oriented; thanks to the electrodynamics transformations, they are seen by the charged particles as a *back propagating* electromagnetic wave [53]. The interaction between the particle and the wave could be described with

the *inverse Compton scattering*; the backscattered wave is frequency-shifted twice by the Doppler effect, and if the length of the magnets is chosen properly, an intense x-ray beam can be produced. If the insertion device induces "gentle" transverse undulations on the moving particle is called *undulator*; this device provides a much more monocromatic and intense radiation than a bending magnet. On the contrary, if the transverse undulations are large, we have a *wiggler*, which is equivalent to an ensemble of bending magnets combined in series.

Synchrotron light presents many advantages as compared with the most common laboratory x-ray generators. Besides the early discussed tremendous brilliance of the beam, which permits to perform very fast and high resolution measurements, moreover the choice of the wavelength is not limited by the characteristic lines of the atomic species in the anode; the spectrum of the radiation emitted in a storage ring is very wide and can be tuned far beyond the range covered by the CuK_α and the MoK_α (see fig. 2.4b). In the following table the main characteristics of several synchrotrons are summarised.

	SLS (CH)	**ESRF (FR)**	**APS (USA)**	**SPring-8 (Jap)**
Energy	2.4 GeV	6.03 GeV	7 GeV	8 GeV
N° beam-lines	5	32	34	62
circunference	288 m	844 m	1104 m	1436 m
Beam current max	400 mA	200 mA	100 mA	100 mA

Table 2.1: Some characteristics of several synchrotrons today in operation.

2.2.2 Monochromatisation and collimation of x-rays

A common problem in a x-rays diffraction experiment is the need to provide a beam of monocromatic radiation. The monochromatisation of the beam can be obtained in several ways: by the use of filters or by introducing monochromators between the source and the sample.

In the first case, a specific material, which absorbs selectively in well definite x-ray bands is interposed; its thickness is calibrated so that the resulting absorption curve minimises the loss in intensity in the region of interest, but maximises it in the region of background.

An alternative, most efficient and more used method consists of a *crystal monochromator*. From the Bragg law, if one fixes the value of d and θ, the diffraction condition is satisfied for only a value of λ. The crystal monochromator should be sufficiently mechanically strong to mantain their physical characteristics during the x-ray beam

exposition; moreover, the interplanar distance d should allow to obtain the scattered monochromatised beam at a reasonable angle. The mosaicity of the crystal must be very low, to eliminate the dispersion of the beam. By bending the crystal, one can both monochromatise and focus the incident beam.

In order to obtain a x-ray beam as collimated as possible, it is necessary to use a *collimator*. It consists of a cylinder with two apertures, called *pinholes*, that define the divergence of the beam. A third aperture posed at the end of the device does not modify the beam size, but allows to eliminate excess of scattered radiation.

2.2.3 Detectors

The first method of detection of x-rays was represented by the use of photographic films; but due to the intrinsic low resolution and to the difficult of extracting digital data, they were substituted by more efficient proportional and scintillation detectors. The former provides an output voltage which is proportional to the x-ray photon, and is characterised by an higher energy resolution; the latter, on the contrary presents a good quantum counting efficiency and hence is more suitable for working with a monochromatic beam. On the other hand, most better performance are now reached by solid state detectors, usually Li-drifted silicon crystals, which present a quantum counting efficiency of ~ 100 % [54].

A very important class of detectors is represented by the position-sensitive detectors (PSD); these provide not only the number of countings, but also the spatial position of the single event. The early versions were formed by an array of proportional counters, hence they were linear and able to subtend an angle of $\sim 10°$. Now, also two-dimensional detectors are available, as for example the image plates. The main advantage of a PSD is the improvement in the acquisition rate; moreover, especially for powder experiments (see below) a two dimensional image of the diffracted radiation yields much more information, for example on the texture of the sample. On the other hand, PSD generally display lower resolution with respect to a point detector, even if it generally does not constitute a serial limitation.

2.3 X-ray diffraction for polycrystalline materials

The compounds studied during this work were in a polycrystalline form, due to the impossibility of obtaining a single crystal. Hence, the following section is devoted to an overview of the tecniques used for the powder diffraction analysis.

2.3.1 Powder diffraction applications

Powder diffraction is mainly used for both *qualitative* and *quantitative analysis* of multiphasic crystalline materials. This means that one can deduce from a powder pattern what are the crystalline phases contained in the sample, and also evaluate the percentage in weight of the various phases.

The *qualitative analysis* is based on the existence of the Powder Diffraction File (PDF), a data bank containing the crystallographic information of all the known structures; this file is daily updated and it is distributed by an International organisation called Joint Committee for Powder Diffraction Standards (JCPDS). For a phase analysis in a sample it is generally sufficient to map the positions of the diffraction lines.

On the contrary, the *quantitative analysis* is generally based on a *Rietveld refinement* (see cap. 4.2) of the diffraction pattern; in this case the check is complicated by the fact that different phases present different absorption of x-rays, and the simple assumption of a direct proportionality between the intensity measured and the amount of a given crystalline phase present in the sample is not correct. Several theoretical studies were performed, but the simplest approach is based on the addition in the powder of an *international standard* (for example corundum NIST 676). In this case the weight fraction of x_i of the i-th component is [50]:

$$x_i = x_f \frac{k_f}{k_i} \frac{I_i}{I_f} \tag{2.29}$$

where x_f is the weight fraction of the flushing agent, I_i and I_f their relative intensity, k_i and k_f the intensities relative to that the reference substance.

Recent improvements of the computer-based methods allows now also the *ab initio* determination, in some simpler cases, of the crystal structures from powder data, especially for substances for which suitable single crystals are not available. This particular topic will be discussed in detail in cap. 4.

2.3.2 Geometries used in powder diffraction

A *polycrystalline material* or *powder* is an ensemble of a high number of randomly oriented crystallites. This ensemble can be obtained simply grinding a single crystal, but very often the powder condition of the sample is the only available state, because it is impossible to obtain a sufficiently big single crystal during the synthesis process. The isotropic arrangement of the crystallites in the real space means that in the reciprocal lattice the scattering vectors does lie no more on the nodes, but form spherical surfaces

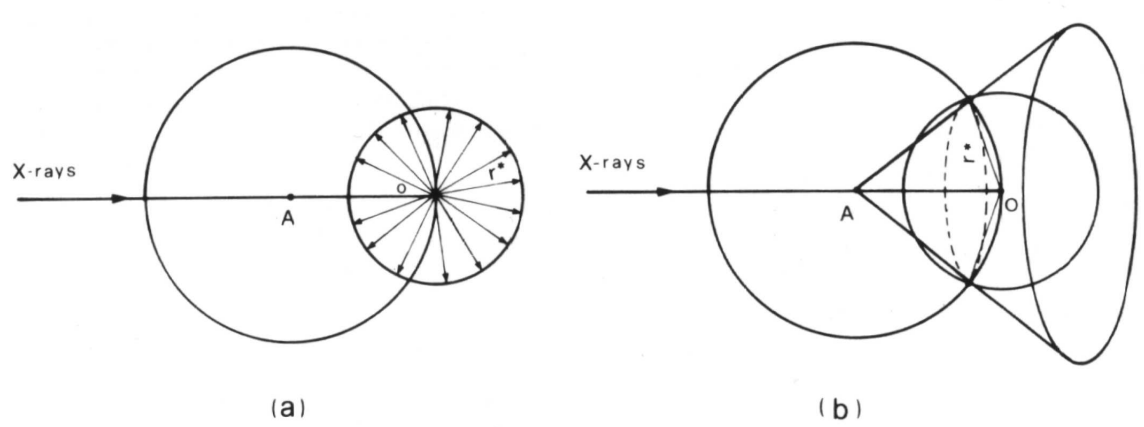

Figure 2.7: a) When a powder of isotropically oriented crystallites are irradiated with x-rays, the same reflection condition is satisfied by an high number of planes. b) The photons diffracted by these planes describe cones in the reciprocal space, called *Debye-Scherrer* cones.

whose radius is the lattice vectors $\mathbf{r}^*$ (see fig. 2.7a). In such a case, the Edwald sphere of radius $\frac{1}{\lambda}$, which represents the scattering condition of a monocromatic radiation whose wave vector is $K = \frac{1}{\lambda}$, intersects the scattering spheres along circumferences, which define the diffraction cones of the powder specimen (see fig. 2.7b).

The simplest way to record a powder diffraction pattern is represented by placing a photographic film perpendicular to the incident x-ray beam. But a more accurate technique, which permits to record also the reflection at angle 2θ greater than $\frac{\pi}{4}$, consists of the use of a *Debye-Scherrer camera*, in which the film covers the whole solid angle around the specimen, and the x-ray source is a parallel beam obtained by the use of a collimator (see subsect. 2.2.2). This geometry is used also in the modern powder diffractometers, in which the sensitive medium is replaced by a quantum counter position sensitive detector. The two main kinds of powder diffractometers are:

- *Debye-Scherrer diffractometers*: the monochromatic beam is collimated on the sample, which presents a cylindrical geometry (a capillary) and is in slow rotation at the centre of the goniometer (see fig. 2.8a). The data are collected by the use of a point or area detector. The advantage of this geometry, also called $\theta - 2\theta$, is that the detector can easily scan almost all the 2θ range, and, if an area detector is used, the acquisition is very fast. The disadvantages are represented by the low intensity of the x-ray beam, if conventional generator tubes are considered, due to the requirement of a parallel beam. This puts severe limits on the spatial

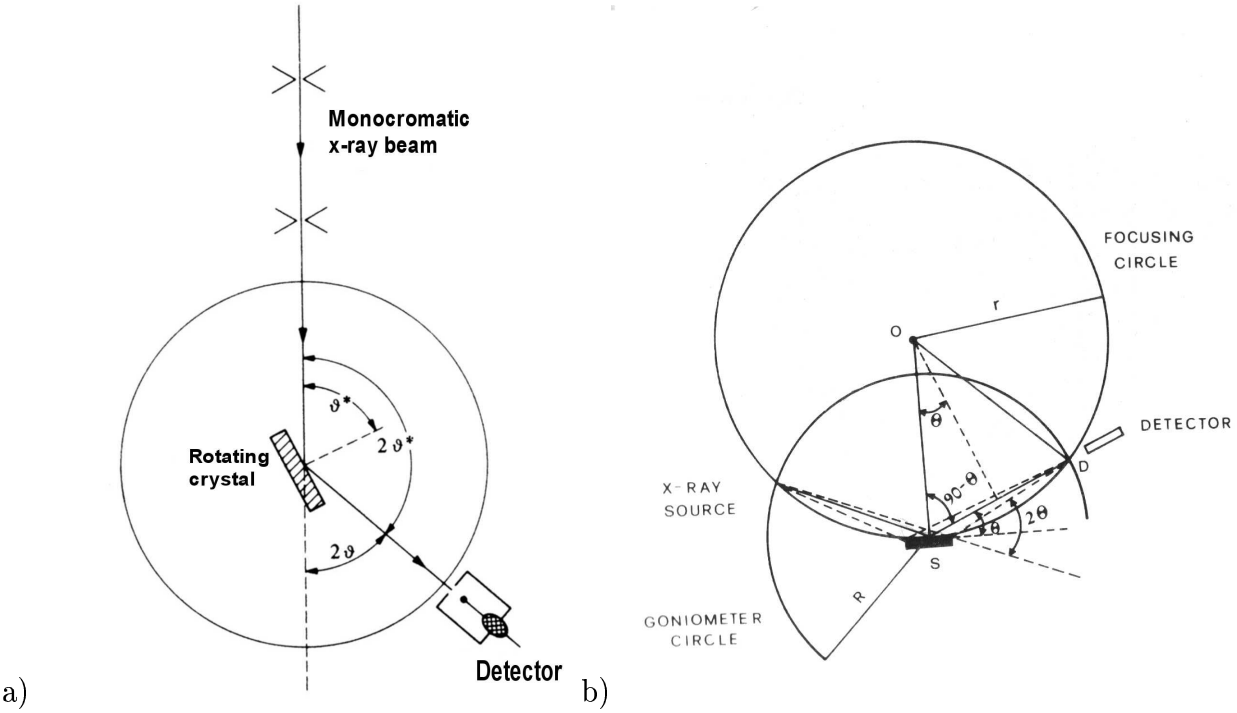

a) b)

Figure 2.8: Geometry of: a) a Debye-Scherrer diffractometer and b) a Bragg-Brentano diffractometer. In this second case the diffraction image must be taken only when the detector lies on the focusing circle. The condition is conserved only if the detector and the sample (or alternatively the detector and the x-ray source) rotate together of the same angle θ during the measurement.

resolution of the diffraction profile.

- *Bragg-Brentano diffractometers*: they use the Seeman-Bohlin parafocusing geometry, shown in fig. 2.8b. In this case the x-ray beam is defocused on the sample, whose dimensions can be higher than in the previous case, and then refocused on the detector. To ensure the refocussing, both the detector and the specimen must move during the data collection. In this geometry, also called $\theta - \theta$, an higher x-ray flux can be reached, together with an high data resolution, but the main disadvantage is the impossibility to span the whole 2θ range. Moreover, due to the impossibility of acquire data at $2\theta = 0$, the instrument can be calibrated only by using samples as standards.

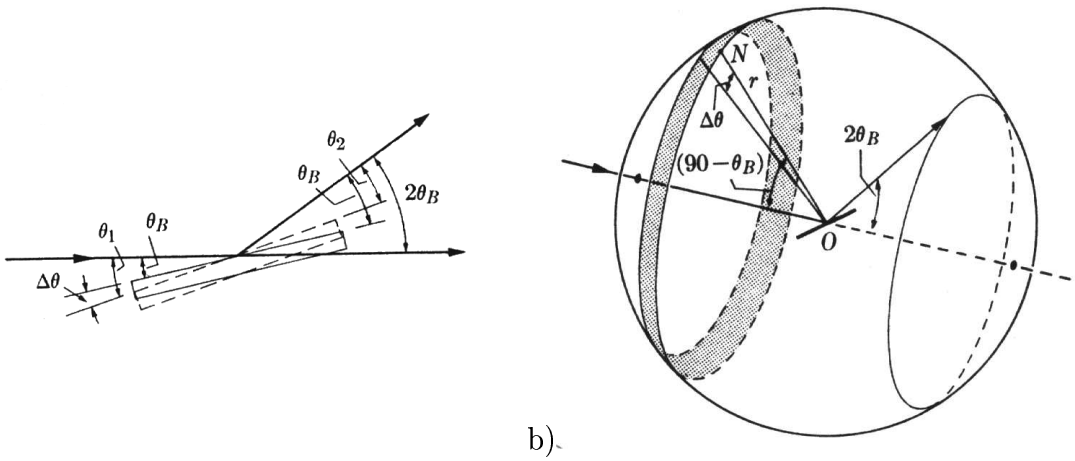

a) b)

Figure 2.9: A schematic representation of a) a non-ideal Bragg reflection, and b) the distribution of the plane normals of randomly oriented crystallites; Lorentz factor arises from these geometrical effects.

2.3.3 Data reduction in a powder x-ray experiment

The relationship between the square of the factor structure, which contains the information about the atomic arrangement in the unit cell, and the integrated intensity, which is the experimentally available data in a powder diffraction experiment, is not direct, but involves several other factors that vary from reflection to reflection. These factors can be summarised as in the eq. 2.30:

$$I_H = kmI_0LPT\,|F_{\mathbf{H}}|^2 \tag{2.30}$$

where k is a constant, which includes some constant factors. I_0 is the incident radiation intensity and $|F_{\mathbf{H}}|^2$ is the square modulus of the structure factor, comprehensive also of the thermal effects (see subsec. 2.1.4); m is the multiplicity factor of the considered reflection: actually it may be defined as the number of planes of the crystal which have the same spacing, and hence give rise to superimposing Debye-Scherrer cones. L, P and T are respectively the *Lorentz factor*, the *polarisation factor* and the *transmission factor*. It's worth to consider in detail these last three contributions.

The Lorentz correction

This factor takes into account some geometrical effects, which deeply influence the intensity of the reflection in a powder diffraction experiment. The so called Lorentz correction arises from three different contributions:

1. The powder particles in the specimen, since they are characterised by all the possible orientations, behave as a rotating crystal which, with its movement, probes the various Bragg reflections. Hence it is possible to consider, for simplicity, a crystal in rotation at a uniform angular velocity about an axis normal to the incident x-ray beam (see fig. 2.9a). In a not ideal experiment, the Bragg law will be satisfied not only at the angle θ_B, but also at slight different angles in the ranges $\Delta\theta$ around θ_B. It is possible to demonstrate [55] that, in these conditions, $\Delta\theta$, and hence the maximum intensity of the Bragg reflection I_{max}, are proportional to $\frac{1}{\sin\theta_B}$. On the contrary, the *breadth* B of the reflection is proportional to $\frac{1}{\cos\theta_B}$; hence the integrated intensity, rougly given by $I_{max}B$, will be proportional to:

$$I_H \propto I_{max}B \propto \frac{1}{\sin 2\theta_B}$$

2. A second geometrical factor arises from the fact that, in a completely random set of particles, the number of crystallites oriented at a definite direction is not constant, but depends on their orientation. Considering the mapping of the whole orientations on a sphere (see fig. 2.9b), it can be found that the number of particles favourably oriented for a Bragg reflection, and hence the integrated intensity, is proportional to $\cos\theta_B$.

3. A last third contribution depends on the geometry of the diffractometer. In the case of a Debye-Scherrer diffractometer, the measured integrated intensity is only a small part of the total intensity of the diffraction cone, due to the finite dimensions of the detector, and is proportional to $\frac{1}{\sin 2\theta_B}$ [55].

The overall effect of these three contributions is expressed by the *Lorentz factor*:

$$Lorentz\ factor \propto \frac{1}{\sin^2\theta\cos\theta} \tag{2.31}$$

The polarisation correction

It depends on the state of polarisation of the incident x-ray beam, and the angle of diffraction. As already shown in subsect. 2.1.1, even if the incident radiation is totally unpolarised, nevertheless the diffracted light results polarised, and the final intensity depends on the Bragg angle θ through the polarisation factor:

$$P = \frac{1}{2}(1 + \cos^2 2\theta) \tag{2.32}$$

More complex expressions describe the polarisation behaviour when the radiation is monocromatised by a crystal, or the radiation is produced by a synchrotron [56]. The Lorentz and the polarisation factor are usually treated as a single correction factor, called the LP correction. The global effect of the LP correction is to decrease the intensity of the reflections at intermiediate angles, compared to those in forward and in backward directions.

The absorption correction

The transmission factor T is related to the absorption of the incident and diffracted radiation, which, before and after the scattering event, crosses the specimen for a while. The intensity of the beam is reduced leading to the *Beer's equation*:

$$\frac{I}{I_0} = \exp(-\mu x) \tag{2.33}$$

where μ is the linear absorption coefficient of the sample. Obviously, the path length x depends on the point which scatters the x-rays and on the shape of the sample. The value of T, the transmission factor of the whole crystal, is obtained by integrating the previous expression over the total crystal volume:

$$T = \frac{1}{V}\int_V \exp(-\mu x) dV \tag{2.34}$$

On the other hand, the μ value can be evaluate from the mass absorption coefficient of the atoms present on the unit cell. The absorption coefficient is smaller for lighter atoms and for shorter wavelengths of the x radiation.

It is obvious that, if a rough estimate of T is easy to do, on the contrary the analytical resolution of the integral is much more difficult. Even if numerical approaches exist, absorption still remains one of the more serious source of error in the determination of the integrated intensities. Luckily, the fullerides studied in this work are characterised by molecules with light atoms (carbon, lithium and sodium); this fact permitted to ignore, in first approximation, the absorption effects.

2.4 Description of the experimental apparatus used

In this work, several powder x-rays diffractometers were used, both laboratory and in synchrotron facilities. In the following section a brief description of these instruments was given.

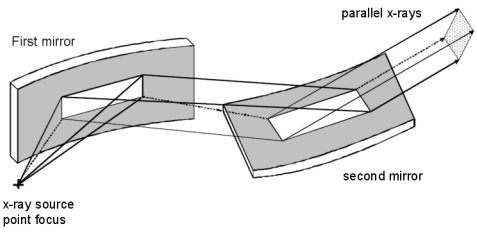

a)

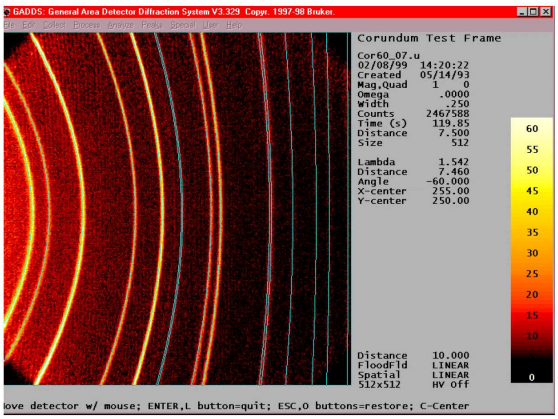

b)

Figure 2.10: a) The scheme of a double Gobel Mirror system. b) The main window in GADDS: the 2D image of the diffraction cones are well visible.

2.4.1 Laboratory x-ray diffractometer

The preliminary characterisation of the samples was performed on a *Bruker D8 discover* with *GADDS* diffractometer, operating in Debye-Scherrer geometry and using a sealed tube generator (CuK_α). The geometry imposes that a parallel monochromatic beam bears on the specimen. To obtain this feature, a sophisticated system of monochromatisation and focussing, consisting of a double *Gobel mirrors* (fig. 2.10a), is inserted between the generator and the specimen. The parallel and monochromatic beam obtained ($\lambda = 1.540612$ Å) passes through a collimator, whose pinholes diameters can be change, and reach the capillary placed in the centre of the goniometer. The most important feature of the apparatus is represented by the x-ray detection system, which consists of an *HI-STAR Area Detector*: this is a two-dimensional multi-wire proportional counter (MWPC), which provides a large imaging area (11.5 cm diameter) for the detection of x-rays. The chamber is filled with a Xe/methane gas mixture, which ionises when interacts with an x-ray photon in the range$3-15$ KV; the collected image, a data frame of 1024x1024 pixels, is sent to a PC, where the data processing is made by the GADDS program (see fig. 2.10b). The acquisition system is very efficient (80%) and can be 100 time faster than a traditional scintillation counter or than a PSD, even if the photon flux on the sample is not very high. Moreover, a 2D image of the diffraction pattern provides more information than a traditional 2θ scan, as for example a direct control on preferred orientations of the crystallites in the sample. The main disadvantage of an area detector is represented by the low angular resolution in 2θ ($\sim 0.03°$ with the detector at a distance of 20 cm from the sample, about ten time

Figure 2.11: A picture of the powder diffractometer at the beam-line ID31.

less than in a Bragg-Brentano diffractometer), which is limited by the density of the wires in the chamber. The fast acquisition of the x-ray diffractogram is particularly suitable for monitoring structural phase transitions in a sample, for example during a thermal treatment; this kind of study is available thanks to the presence of a furnace which can heat the specimen up to 800 K.

2.4.2 Synchrotron x-ray diffractometers

The main session of measurements was performed at ESRF (Grenoble, Fr) at the beam-line ID31, which represents the "state of art" of powder diffraction. The diffractometer (see fig. 2.11) presents the Debye-Scherrer geometry and is capable of operating with photon energies in the range $5-60$ KeV. The x-ray beam is generated by an undulator, and is characterised by very high brilliance (about 10^{22}photon/sec·mrad); hence the beam is monochromatised and hits the sample. The diffracted photons are collected by a series of 9 point-detectors, which guarantee a very high angular resolution.

The sample environment is represented, concerning the cryogenic apparatus, by a cold-nitrogen-gas blower, which permits to work in the range $80-500$ K, and a liquid-helium-cooled cryostat, which can lower the temperature of the specimen down to 2.5 K; for the high temperatures, diffraction measurements can be performed up to

$\sim 1500°$ C with a mirror furnace and Pt capillary; otherwise quartz capillary can be heated up to $950°$ C with an hot-air blower.

Several powder diffraction measurements were performed also at the *Swiss Light Source* of the Paul Scherrer Institute (SLS-PSI, Villigen-Zurich, CH), at the beam-line X04SA. This beam-line sequentially serves three end-stations: x-ray tomographic microscopy (XTM), *in situ* surface diffraction (SD) and powder diffraction. With respect ESRF-ID31, the performances of this beamline are sligthly worse: the energy range is between $5-40$ KeV, the photon flux results $\sim 10^{13}$ photon/sec at 10 KeV. The acquisition of the data is provided by a crystal analyser, consisting of 5 point detectors, which permits to obtain high resolution diffractograms (better than $0.005°$).

Chapter 3

Raman spectroscopy in fullerides

Introduction

Raman spectroscopy is an important and powerful tool of investigation of solids. The technique is based on Raman effect, discovered by C. V. Raman in 1928; this is a *non linear* scattering process, in which electromagnetic radiation interacts with the vibrational modes of the molecules of the sample.

In this chapter the most important features of the Raman spectroscopy and its application to fullerene systems will be discussed. In particular, first a qualitative interpretation of the scattering process is given (sec. 3.1), and a classical theory of Raman effect is exposed (sec. 3.2). Then, the main vibrational properties of C_{60} and fullerides are introduced (sec. 3.3), with particular attention to the physical information which can be inferred from a Raman spectrum. In the last part of the chapter, a brief description of the experimental apparatus used is given (sec 3.4).

3.1 The scattering processes

3.1.1 Rayleigh and Raman scattering

When monochromatic light is incident on a transparent solid (for simplicity the adsorption phenomenon is here ignored), the radiation is scattered. If the spectrum of the scattered light is analysed, not only the frequency ω_I of the incident radiation is observed, but also pairs of new frequencies of the type $\omega_I \pm \omega_M$ are present. In this simple example the two main contributions to the scattering phenomenon are present: the component *without* change of frequency with respect to the incident radiation is called *Rayleigh scattering*, whereas the components *with* change of frequency are due

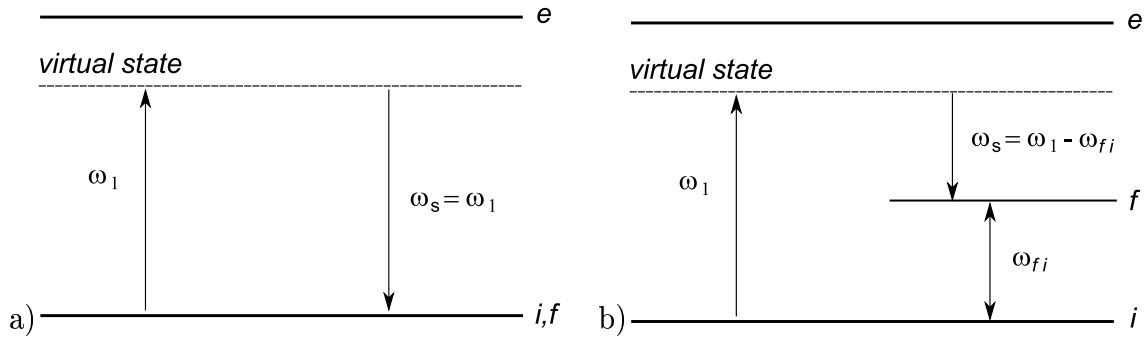

Figure 3.1: The schematic electronic transition during Rayleigh scattering a), and Raman (Stokes) scattering.

to the *Raman scattering*. In particular, the component at frequency $\omega_I - \omega_M$ is named *Stokes Raman band*, whereas the component at frequency $\omega_I + \omega_M$ is named *anti-Stokes Raman band*.

There exist several approaches for treating scattering phenomena: a purely classical one which is only partially exhaustive, but which is sufficient for our purposes and will be develop here. A quantum mechanical treatment which retains the classical model of the radiation permits to obtain quite satisfactory and complete explanation. Further, there is also a totally quantic approach, both for the radiation and the material system even more detailed and exhaustive [57].

3.1.2 A qualitative explanation

To understand qualitatively the Raileigh and Raman effects, it is useful a simple model based on the photon description of electromagnetic radiation (see fig. 3.1). Before the interaction, the radiation can be represented as a system of n_I photons with energy $\hbar\omega_I$ and frequency ω_I. The interaction of the radiation with the molecules of the sample leads to the annihilation of one photon of energy $\hbar\omega_I$, the creation of a new photon of energy $\hbar\omega_S$ and the transition of the molecule from the ground state with energy E_i to the excited state with energy E_f; it results $E_{fi} = \hbar(\omega_I - \omega_S)$ and $\omega_S = \omega_I - \omega_{fi}$. It is worth to note that in this process the energy $\hbar\omega_I$ does not correspond to any electronic transition energy of the molecule, and the incident photon is not absorbed in the strict spectroscopic sense. Hence there is no conservation of energy in this stage; absorption without conservation energy is called *virtual absorption* and the resulting state is called *virtual state*. The radiation after the scattering consists of $(n_I - 1)$ photons of energy $\hbar\omega_I$ and one photon of energy $\hbar\omega_S$. The process just described is

the *Stokes Raman scattering*, because $E_f > E_i$. But in general the molecules of the solid could be in an excited state already *before* the scattering with the photon; in this case the incident photon promotes a virtual transition which brings the molecule to the ground state, then $\omega_S = \omega_I + \omega_{fi}$ and the phenomenon is called *anti-Stokes Raman scattering*. Obviously, this event results less favourable with respect the Stokes scattering. Finally, when $E_f = E_i$, $\omega_S = \omega_I$ and the phenomenon is called *elastic Rayleigh scattering*. in all the cases, the role of the incident radiation consists of perturbing the molecule and opening the possibility of a spectroscopic transition, rather than providing a direct absorption.

3.2 Classical theory of Raman scattering

3.2.1 Dipole moment series expansion

When the electromagnetic field of the incident radiation hits a molecule, the most significant multipole source of the scattered radiation is the oscillating electric dipole. The intensity I of the emitted radiation of an oscillating dipole induced in the molecule by the radiation of frequency ω_I along a direction making an angle θ with the axis of the dipole is given by [57]:

$$I = \frac{1}{32\pi^2\epsilon_0 c_0^3}\omega_S^4 p_0^2 \sin^2\theta \tag{3.1}$$

where p_0 is the amplitude of the induced dipole with frequency ω_S, which in general is different from ω_I.

The *total time-dependent induced electric dipole moment vector* of a molecule may be written as the sum of a series of time-dependent induced electric dipole moment vectors $\mathbf{p}^{(1)}$, $\mathbf{p}^{(2)}$, $\mathbf{p}^{(3)}$...:

$$\mathbf{p} = \mathbf{p}^{(1)} + \mathbf{p}^{(2)} + \mathbf{p}^{(3)} + ... \tag{3.2}$$

with $\mathbf{p}^{(1)} \gg \mathbf{p}^{(2)} \gg \mathbf{p}^{(3)}$. They are connected to the incident electric field vector by tensorial relations:

$$\mathbf{p}^{(1)} = \alpha \cdot \mathbf{E} \tag{3.3}$$

$$\mathbf{p}^{(2)} = \frac{1}{2}\beta : \mathbf{EE} \tag{3.4}$$

$$\mathbf{p}^{(3)} = \frac{1}{6}\gamma\vdots\mathbf{EEE} \tag{3.5}$$

where α, β, γ are the *polarizability tensors*, respectively of second, third and fourth rank. Working in *dipole approximation* means ignore the terms higher than first order,

and consider only the part of the dipole moment vector which depends *linearly* on **E**. This term permits of explain the Rayleigh and Raman scattering, whereas the higher terms take in account higher order process, like *hyper-Rayleigh* and *hyper-Raman scattering*, *second hyper-Rayleigh* and *second hyper-Raman scattering* [57].

3.2.2 The first-order polarizability tensor

The next step is to calculate, for a molecule, the frequency-dependent linear induced dipole vector $\mathbf{p}^{(1)}$. As shown in eq. 3.2, this vector depends both on the electric field vector of the incident radiation which oscillates at the frequency ω_I, and on the polarizability tensor α of the molecule. This last term, in general, will be a function of the nuclear coordinate of the molecule, and hence of the molecular vibrational frequencies. For simplicity, a molecule which is free to vibrate, but does not rotate, is considered. The variation of the polarizability with vibrations of the molecule can be expressed by a series expansion of each component $\alpha_{\rho\sigma}$ of the polarizability tensor α with respect to the *normal coordinates* of vibration:

$$\alpha_{\rho\sigma} = (\alpha_{\rho\sigma})_0 + \sum_k \left(\frac{\partial \alpha_{\rho\sigma}}{\partial Q_k}\right)_0 Q_k + \frac{1}{2}\sum_{k,l}\left(\frac{\partial^2 \alpha_{\rho\sigma}}{\partial Q_k \partial Q_l}\right)_0 Q_k Q_l + ... \tag{3.6}$$

where $(\alpha_{\rho\sigma})_0$ is the value of $\alpha_{\rho\sigma}$ at the equilibrium configuration and Q_k, Q_l are the normal coordinates of vibration of the molecule associated to the vibrational frequencies ω_k, ω_l. The sum is over all normal coordinates. In the *electrical harmonic approximation* the terms which contain powers of Q higher than the first are neglected. Moreover, focussing only on the contribution to the polarizability from one normal mode of vibration Q_k:

$$(\alpha_{\rho\sigma})_k = (\alpha_{\rho\sigma})_0 + (\alpha'_{\rho\sigma})_k Q_k \tag{3.7}$$

where $(\alpha'_{\rho\sigma})_k = \left(\frac{\partial \alpha_{\rho\sigma}}{\partial Q_k}\right)_0$. The last equation is valid for all the tensor components, it is possible to write:

$$\alpha_k = \alpha_0 + \alpha'_k Q_k \tag{3.8}$$

3.2.3 Stokes and anti-Stokes bands

In the approximation of simple harmonic motion, the time dependence of Q_k could be expressed as:

$$Q_k = Q_{k_0} \cos(w_k t + \delta_k) \tag{3.9}$$

where δ_k is a phase factor and Q_{k_0} is the amplitude of the vibration. Then the polarizability tensor results:

$$\alpha_k = \alpha_0 + \alpha'_k Q_{k_0} \cos(\omega_k t + \delta_k) \tag{3.10}$$

Introducing now the time dependence in the electric field, $\mathbf{E} = \mathbf{E}_0 \cos \omega_I t$ and the time-dependent vector $\mathbf{p}^{(1)}$ results:

$$\mathbf{p}^{(1)} = \alpha_0 \mathbf{E}_0 \cos(\omega_I t) + \alpha'_k \mathbf{E}_0 Q_{k_0} \cos(\omega_k t + \delta_k) \cos \omega_I t \tag{3.11}$$

By the use of trigonometric considerations, it is possible to express $\mathbf{p}^{(1)}$ as a sum of *three* terms:

$$\mathbf{p}^{(1)} = \mathbf{p}^{(1)}(\omega_I) + \mathbf{p}^{(1)}(\omega_I - \omega_k) + \mathbf{p}^{(1)}(\omega_I + \omega_k) \tag{3.12}$$

Here, the first contribution $\mathbf{p}^{(1)}(\omega_I) = \alpha^{Ray} \mathbf{E}_0 \cos \omega_I t$ represents the Rayleigh scattering, where the second and the third terms are responsible of the Raman scattering, respectively the Stokes and the anti-Stokes band:

$$\mathbf{p}^{(1)}(\omega_I \pm \omega_k) = \alpha_K^{Ram} \mathbf{E}_0 \cos(\omega_I \pm \omega_k \pm \delta_k) t \tag{3.13}$$

Rayleigh scattering can be coherent or incoherent, depending on the situation, whereas Raman scattering is *intrinsically incoherent*; in fact the term δ_k is in general different for every molecule in the medium.

3.2.4 Selection rules

The necessary condition for Rayleigh scattering is that α^{Ray} is non-zero; but all molecules are polarizable, then all exhibit Rayleigh scattering. On the contrary, the necessary condition for Raman scattering associated with the molecular frequency ω_k is that α_k^{Ram} is non-zero. This implies that *at least one of the components* $(\alpha'_{\rho\sigma})_k$ *of the polarizability derivative*, which respect to the normal coordinate Q_k, *is non-zero*; this fact is not always true, but depends on the geometry of the molecule.

This selection rule, just derived from classical considerations, is simple in concept, but is progressively more difficult to apply as the complexity of the molecule increases. It is instructive to consider a comparison between Raman and infrared activity. The condition for vibrational infrared activity is that *at least one of dipole moment component derivatives,* with respect to the normal coordinate Q_k, *is non-zero.* If the molecule has a centre of symmetry, as for example fullerene C_{60}, those vibrations which are Raman active, are infrared inactive, and vice versa (rule of *mutual exclusion*). On the

contrary, for molecules with relatively low symmetry, all or almost all vibrations are both infrared and Raman active. Moreover, for high symmetry systems, some vibrations may be both Raman and infrared inactive.

3.3 Molecular dynamics of fullerene C_{60} and fullerides

3.3.1 C_{60} molecule and fullerite

C_{60} molecule is characterised by the presence of 174 vibrational modes ($3 \times 60 - 3$ translations -3 rotations), but the high I_h icosahedral symmetry reduces to 46 the number of the distinct eigenfrequencies. In the following table are listed the complete group of symmetry labels for the vibrational modes of C_{60}, with their multiplicity and degeneracy [58]:

I_h **group label**	**Multiplicity**	**Degeneracy**	**Activity**
A_g	2	1	Raman
T_{1g}	3	3	
T_{2g}	4	3	
G_g	6	4	
H_g	8	5	Raman
A_u	1	1	
T_{1u}	4	3	IR
T_{2u}	5	3	
G_u	6	4	
H_u	7	5	

Table 3.1: Eigenmodes of the C_{60} molecule.

the corresponding normal modes on the molecule are far from being intuitive, despite the high symmetry of the system; this because of the presence of a large number of carbon atoms in the C_{60} unit.

At the beginning, the whole vibrational frequency set of C_{60} molecule was obtained by measures of inelastic neutron scattering [59]; this provided directly also the degeneracy of the modes, which resulted proportional to the integrated intensity of the peaks. But in practice, optical spectroscopies, both infrared and Raman, even if they are subjected to the restriction of the selection rules, yielded more detailed and less ambiguous results [60].

In particular, IR spectroscopy allows the study of the four T_{1u} vibrational modes, whereas the Raman active modes in C_{60} consist of the two A_g and of the eight H_g

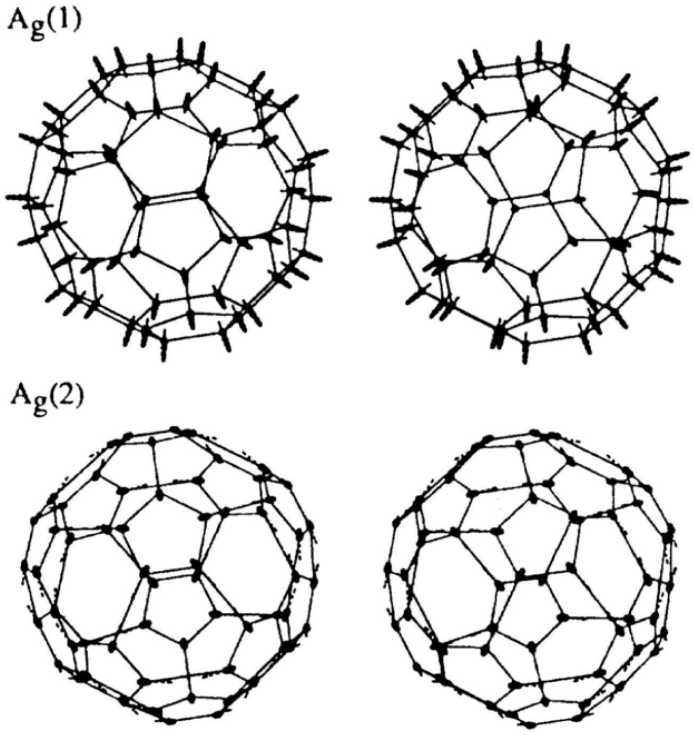

Figure 3.2: The fully symmetric A_g modes in fullerene C_{60}, from [58].

vibrations.

Focussing on the last two, the fully two symmetric A_g modes (see fig. 3.2) are called respectively the *breathing* mode, in which each carbon atom moves radially from the centre of the molecule, thus letting the whole molecule "breath"; and the *pentagonal pinch* mode, in which the two different bond lengths b_{hh} and b_{ph} of C_{60} (see sec. 1.1) are modulated, and therefore the pentagonal faces vary their area. On the contrary, the eight quadrupolar H_g modes, each fivefold degenerate, retain an axis of fivefold symmetry; their representation is more complicated. Some of the deformations induced by these vibrational modes are associated to the Jahn Teller distortions of the buckyball [58] (see sec. 1.3.2).

The experimental identifications of the vibrational frequencies were performed on fullerene C_{60} in the gas, solution, thin films and crystalline phases. When fullerenes are arranged to form the solid fullerite, the presence of crystal field makes some silent molecular vibrations weakly Raman and infrared active. However, due to the low interactions among the C_{60} units in the Van der Waals solid, these crystal effects, especially at room temperature, are very small, and a typical Raman spectrum of

pristine C_{60} contains only the ten active modes previously described.

The *intramolecular* modes extend typically from 30 to 200 meV. Usually, in a Raman spectrum the energy scale[1] is given by cm^{-1}; in this unit the interval corresponds to $240 - 1600$ cm^{-1}. The $A_g(2)$ pentagonal pinch mode is hard, at 1470 cm^{-1}, whereas the breathing mode $A_g(1)$ is at 490 cm^{-1}. The eight H_g modes range in energy from the very soft squash mode $H_g(1)$ at 270 cm^{-1} to the hard Jahn Teller mode $H_g(8)$ at 1575 cm^{-1}. As comparison, the four infrared T_{1u} active modes are located respectively at 527, 577, 1183 and 1428 cm^{-1}. Below 30 meV are placed the *intermolecular* modes, characteristic of the fullerite crystal.

3.3.2 Fullerides A_xC_{60}

Fullerides are molecular crystals, in which the C_{60} structure is only slightly affected by the presence of the alkali atoms. Hence, the vibrational frequencies can be directly related to those of the isolated molecule. However, several differences in the dynamic spectrum between the fullerides and fullerite are present, mainly arising from the charge transfer from the metal to the molecule. The charge transfer produces many effects:

- It alters the bond-stretching and bond bending force constants, thus varying the resonance frequency of several modes.
- It can change the structure of the molecule, both by Jahn Teller distortions, and by relaxation of the molecule; this can induce the broadening of some peaks due to the lifting of their degeneration.
- It introduces ionic forces in the lattice, thus modifying the intermolecular optical modes

Moreover, if the fulleride displays metallic behaviour, the vibrational modes can directly couple with the conductions electrons, which, as already stressed in cap. 1, in fullerene based systems present quite the same energy; the strength of coupling of the Raman modes and the conduction electrons is an important parameter for understanding the transport properties of the compound and its superconductive behaviour. Typical features in the Raman spectrum due to electron-phonon coupling are the broadening or the disappearance of the resonance involved in the coupling (see later).

[1]The conversion between the two energy scale units is: 10 meV = 80.1 cm^{-1}, 100 cm^{-1} = 12.5 meV.

A direct comparison of the Raman active modes in fullerite C_{60} and in charge-transfer fulleride salts shows that, in the latter, the hard "tangential" modes are generally softer, because of the charge transfer induced elongation of the intramolecular bond lengths. On the contrary the soft breathing $A_g(1)$ mode results harder [61], probably as a consequence of the changes in the curvature of the molecule. A very used empirical rule involves the hard $A_g(2)$ mode; from measures performed on the A_xC_{60} systems, by varying the stoichiometry level, it was observed that the pentagonal pinch mode displays a downshift of $\sim 5-6$ cm^{-1} per electron transferred on the C_{60} molecule [62], with an almost linear trend. Hence, the measure of the $A_g(2)$ shift with respect the reference value of pristine C_{60} (1469 cm^{-1} at 300 K) is a quite confident method used to evaluate the *effective* charge transfer in a fulleride.

In metals, the Raman line width could be increased because of the presence of two main scattering channels; a two-photon decay channel, which is associated with the presence of an anharmonic crystal potential, effect which is usually small in C_{60} compounds [63]; and a electron-phonon scattering channel. This last effect has been extensively studied in fullerene systems, and a strong coupling between conduction electrons and the H_g modes was detected in A_3C_{60} (A=K, Rb) metallic fullerides [64, 63]. In particular, the broadening of the Raman modes can be used as a measure of the electron-phonon coupling strength; the phonon line width broadening $\Delta\Gamma$ is related to a dimensionless electron-phonon coupling constant λ by the formula:

$$\lambda = \sum_i \lambda_1 = \sum_i C \frac{\Delta\Gamma_i}{\omega_i^2} \left[\frac{1}{N(\epsilon_f)}\right] \tag{3.14}$$

where ω_i is the discrete phonon frequency for the i-th mode, $C = \frac{d_i}{\pi}$, and d_i is the degeneracy of the ith mode. Typical values of λ found in A_3C_{60} are $0.5 - 0.6$, in good agreement with the theoretical prediction.

Some vibrational modes in metallic compounds can also display asymmetrical broadening, due to the presence of *Fano resonances*. This shape arises when a *discrete* vibrational mode couples with a *Raman-active continuum*, which is represented by the conducting electrons. In this case the line-shape is described by the equation [63]:

$$I = I_0 \left[1 + \frac{\omega - \omega_0}{\Gamma}\frac{1}{q}\right]^2 / \left[1 + \frac{(\omega - \omega_0)^2}{\Gamma^2}\right] \tag{3.15}$$

where ω is the renormalized discrete phonon frequency, $\frac{1}{q}$ is the strength of the coupling between the continuum and the discrete mode, Γ is the width of the resonant

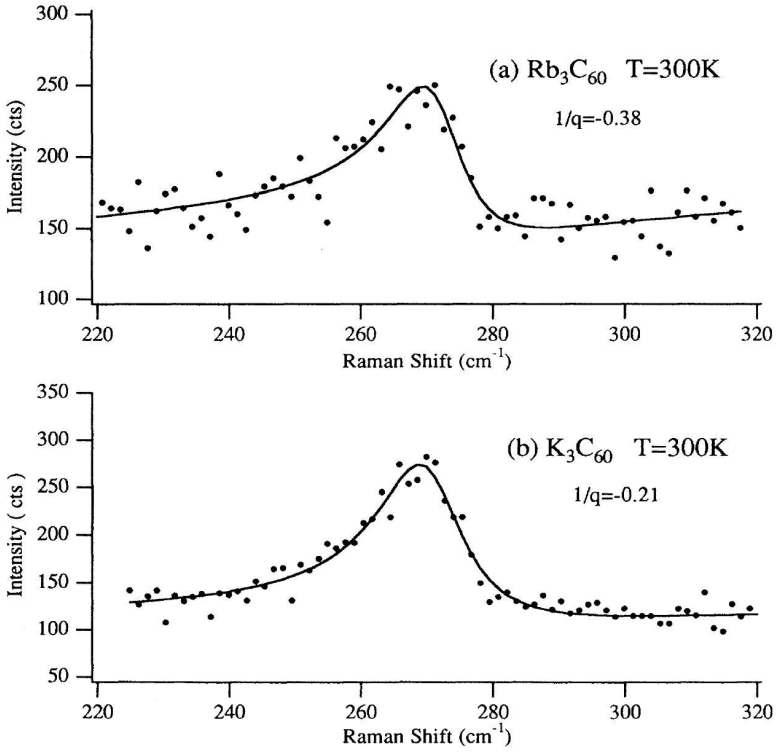

Figure 3.3: The asymmetric broadening of the $H_g(1)$ mode in a) Rb_3C_{60} and b) in K_3C_{60} conducting films, well fitted with a Fano line-shape [63].

interference between the continuum and discrete scattering channels. A typical Fano line-shape is shown in fig. 3.3.

3.3.3 Polymerised fullerenes

Raman spectroscopy is a powerful method also to characterise and study C_{60} polymeric structures, both doped and undoped phases. When covalent bonds estabilish among the fullerene units, strong changes are obviously expected in the dispersion curves of the intermolecular phonons, in the low energy range, because the force constants of the libration modes are different in a polymer, with respect a Van der Waals solid. Nevertheless, the deformation of the fullerene cage induced by the sp^3 hybridised carbons causes further changes also in the intramolecular modes. Furthermore, polymerisation generally induces a lowering in the crystal symmetry and hence a modification of the crystal field on the molecule, thus making these effects no more negligible.

The main feature of the Raman spectra of polymeric system is generally the presence

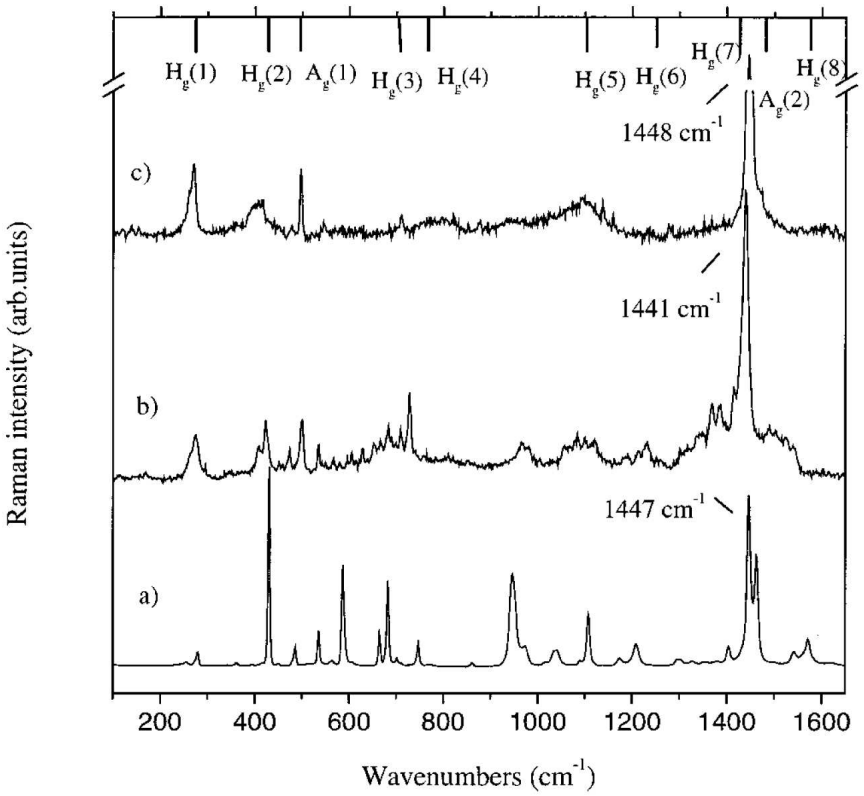

Figure 3.4: Raman spectra for a) pure 2D tetragonal polymerised C_{60}, b) 2D polymerised Na_4C_{60} and c) metallic K_3C_{60} taken at 300 K. The thick lines at the top of the figure show the positions ot the ten Raman active modes of pristine C_{60} [65].

of many peaks in the intramolecular frequency range $200-1600\ cm^{-1}$ (see fig. 3.4). Due to the lift of the H_g modes five-fold degeneracy, up to ~ 40 peaks could be detectable. The $A_g(2)$ resonance is downshifted by the presence of covalent bonds in the buckyball, in analogy with the charge transfer; a similar empirical rule suggests a downshift from the value of pristine unpolymerised C_{60} of $\sim 5.5\ cm^{-1}$ per intermolecular bond [66, 65]. Nevertheless, the application of this rule is still debated, especially in systems both charged and polymerised, where it seems to fail [11]. A further ambiguity arises from the difference of the shift for the two bonding motives of C_{60}, which should lead to different downshifts of the pentagonal pinch mode [65].

Another fingerprint of fullerene polymerisation is given by the presence in the Raman spectrum of a typical resonance at $\sim 1000\ cm^{-1}$, which is not detectable in unpolymerised systems; this mode seems to arise from the four-membered carbon ring stretching, which forms when two fullerenes link by [2+2] cycloaddition reaction [67].

The same stretching mode is also observed in the Raman spectrum of cyclobutane. However, the presence of this resonance also in the single bonded 2D polymer Na_4C_{60} [65] (at 974 and 980 cm^{-1}) put some doubt on this assignment and lead to the hypothesis that this mode could represent also some other vibrations, and may be associated to the generic presence of sp^3-type intermolecular bonds.

3.4 Description of the experimental apparatus

The Raman measurements during this work were recorded in backscattering geometry (see fig. 3.5) with a Renishaw 1000 microRaman and a Jobim-Yvon spectrometers, both equipped with charge coupled device (CCD) camera and microscope lens of different magnification ($\times$50 and $\times$100). The excitation source consisted alternatively of an Ar^+ laser with lines at 488.0 nm (corresponding to 2.54 eV) and 514.5 nm (2.14 eV), or an He-Ne laser with wavelength of 632.8 nm (1.96 eV). The resolution of the spectrometers in both cases was 1 cm^{-1} and the accuracy better than 0.5 cm^{-1}. In order to avoid photo-damage of the investigated samples, care was required to control the effective laser power density, which was limited by the use of filters.

The Raman measurements were performed both at room and at high temperature; in this second case, an home made temperature controlled plate, capable to heat the sample up to 650 K, was placed on the x-y-z automate moving stage of the microscope and the temperature was controlled electronically.

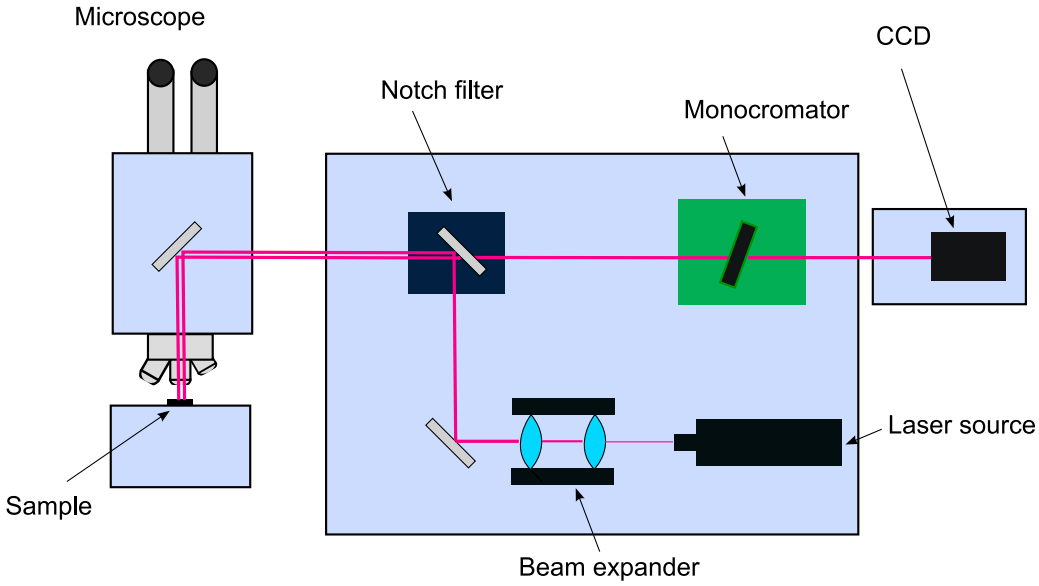

Figure 3.5: A schematic representation of a Raman spectrometer in backscattering configuration.

Chapter 4

Crystallographic analysis

4.1 Introduction

Structure determination starting from powder x-ray diffraction has known a recent surge in the last years, thanks to the development of efficient software routines and to the enhanced power of the new generation of computers. On one hand, the use of powder x-ray data allows structural elucidation of materials impossible to obtain as good quality single crystals; on the other hand, if a suitable starting model is available, structure refinement from powder x-ray diffraction data is a routine procedure, even with standard software toolkits.

Nevertheless, the *ab initio* approach with powder diffraction represents still a challenge, even in case of simple structures, consisting of a few atoms. In fact, the "projection" of information from the three dimensional reciprocal space into just one dimension inevitably introduces overlapping peaks and hence uncertainties in defining the correct structure factor. On the contrary, the generation of a starting model from *single* crystal x-ray diffraction is almost trivial, even for molecules with hundreds of atoms in the asymmetric unit.

In this chapter, the main steps and the most common techniques necessary for an *ab initio* structural analysis, starting from a powder x-ray spectrum, are explained (sec. 4.2). In particular, the Rietveld method, extensively used during this work, is presented (par. 4.2.4). Finally, an overview of two widely used routines, GSAS-EXPGUI and FULLPROF, is given (sec. 4.3).

4.2 Structure determination via powder x-ray diffraction

Ab initio structure determination from powder diffraction data involves a series of steps which are summarised as follows:

- *Careful sample preparation and good data collection strategy*: the compound to be investigated should be finely ground (e.g. by the use of a mortar), until the dimension of crystallites is sufficiently small (usually $<$60 μm). The preferred orientations of the crystallites, which would cause an erroneous assignment of the diffraction peak intensities, should also be minimized; for instance by using a cylindrical capillary and spinning the sample during data acquisition in a Debye-Scherrer geometry. Obviously, a high-resolution diffractometer would also provide better quality data.

- *Powder pattern indexing*: this is a very important step, which allows to assign the crystal cell, the starting values of the lattice parameters and the correct spatial group.

- *Powder pattern decomposition*: permits the extraction of the structure factor amplitudes $|F_{\mathbf{H}}|$ from the indexed reflections, and hence provides the data for the subsequent analysis.

- *Structure solution*: Once the integrated peak intensities are known, this step can be performed by several methods: direct methods, Patterson function, Fourier maps, maximum entropy techniques, etc.

- *Refinement of the atomic positions*: this task is almost always tackled by using the Rietveld method, based on a least square routine.

Depending on the level of knowledge of the starting model, one or more of these steps could be skipped. For example, if the structural model is already well known, only the refinement of the atomic positions is requested and the structure solution could be rather trivial. It is also possible that the initial knowledge is only partial; for example the structure of the molecules in the solid is known, but the information about their arrangement in the crystal is missing. This is usually the case of fullerene systems, where the geometry of the strongly bonded fullerene cage is normally unaltered or only partially modified in the solid state. This fact alone cannot *a priori* exclude any

of the steps in structure determination, nevertheless, *in practice* it allows a certain simplification of the overall analysis.

In the following, an overview of each step is given.

4.2.1 Powder pattern indexing

The indexing of powder diffraction patterns is not an easy task. Indeed, the overlap of degenerate reflections which, in a single crystal diffraction pattern, are well separated, makes the solution of the mathematical problem not unique. Nevertheless, the determination of the crystal symmetry, the unit cell dimensions and the *hkl* indices of each reflections remains a necessary step before starting the structural analysis of powder data.

Many efficient methods for indexing a powder pattern are now available. All of them consist of computer-based routines, which are implemented in various software suites, but the principal procedures are essentially three:

- The semi-exhaustive method proposed by Werner, Eriksson and Westdahl [68]. It is based on a permutation of Miller indices through a trial-and-error routine: the various typologies of cell (cubic, tetragonal, orthorhombic, etc.) are tested starting from the simplest, and for each of them the program tries to find the best match between the observed and calculated reflections. This method is implemented in TREOR.

- The dichotomy method, developed by Boultif and Louer [69]: it is based in the direct space variation of lengths, cell edges and angles values over a finite range, followed by a progressive reduction of these intervals with the dichotomy procedure. A typical program which operates according to this method is DICVOL91.

- The Runge-Ito-de Wolff method developed by Visser [70]: it uses specific relations in the reciprocal space. The program which implements this routine is ITO.

All these programs need precise and accurate starting data, but in no case they can guarantee error-free results. Usually the number reflections needed to index a powder spectrum does not exceed the first twenty. The proposed cell is always associated to a numerical value, the so-called *figure of merit* [54].

4.2.2 Powder pattern decomposition

The determination of the integrated intensities, unambiguously associated with the indexed reflections, provides the overall information which can be extracted from a powder diffractogram. Of course it is hard, or even impossible, to reach such a knowledge, because the exact overlapping of several peaks, very common in high symmetry cells, does not allow a unique assignment. To overcome this inherent difficulty new algorithms, based on different strategies, as for example the *maximum entropy method* (see below), have been developed.

The common strategy envisions the partition of the diffraction profile into individual reflections, whose shape and intensity are treated as free parameters. The fit of the experimental powder pattern with a curve, as similar as possible to the observed data, allows the extraction of the reflection intensities by an integration process. There are substantially two different approaches for the diffractogram fitting:

- The first approach does not put any restrictions on cell parameters; the starting positions of the peaks are generated based exclusively on the refined cell values (obtained by a preliminary indexing procedure), and the subsequent refinement of the curve goes on with a no constraint approach. The most widely used programs of this kind are based on the Maximum Likelihood Estimation (MLE) [71].

- In the second case the whole pattern decomposition proceeds with cell constraints. This approach characterises the most popular methods in current use, respectively due to Pawley [72] and Le Bail [73]. In the Pawley's approach, for each possible reflection an additional parameter is added to the refinement process. The advantage of this method is that all reflections are refined with equal weight, irrespective of the intensities they represent. In the Le Bail approach, the value of the integrated intensities is extracted by iterating a modified Rietveld decomposition formula (see further), in which an arbitrary set of structure factors is used as an input and only the non-structural parameters are refined. Thanks to their high efficiency, both methods have found an extensive use. In both cases only the cell and the profile parameters are involved in the fit.

The knowledge of the extracted intensities allows also the assignment of a correct space group to the structure, by the evaluation of the systematic absences throughout the whole pattern. This step, therefore, represents also the end of the indexing procedure.

4.2.3 Structure solution

Once the integrated intensities have been extracted, the most "time-consuming" procedure of finding a good structural model could start. Depending on the starting knowledge level of the structure and on the characteristics of the system under examination, also in this case several approaches are possible:

- The *traditional technique*: it is based on the adoption of methods conventionally used for structural investigation from single crystal data: hence the powder structure factor could be analysed by the combined use of *Patterson* and *Fourier* methods. The Patterson technique [50] allows to detect the heavier atoms of the structure, whereas the iterative running of difference Fourier maps leads to the location of the remaining lighter elements within the asymmetric unit. The main problem of this approach is that the Patterson method is heavily limited by the presence of overlapping peaks, which introduce a degree of uncertainty in the attribution of the correct structure factors. This factor is a constant of the powder diffraction, as already pointed out. Hence, in case of noisy or incomplete data, this method could lead to a wrong structure solution.

- The *Maximum Entropy Methods* (MEM): it represents a totally different approach, which does not suffer from the previous shortcomings. This strategy consists in searching the most probable and the least biased probability distribution which maximises the entropy of the system, starting from a partial knowledge of the diffraction data. This maximisation, however, is subject to the condition that there must be also the best agreement between calculated and observed intensities. The MEM algorithm was introduced by Takata and Sakata [74]; the thermodynamical approach often makes this method more efficient with respect to the Patterson and Fourier techniques.

- The *direct space methods*: thanks to the high calculus power of modern computers available nowaday, a totally new approach is possible. It consists in operating in the direct space rather than in the reciprocal one. If a fragment of the structure is known *a priori*, the exact model can be obtained by translating and rotating this fragment with Montecarlo based techniques, as *Simulated Annealing* [75]: the evolution of the model in this case is constrained by energy-cost functions, which take in account ideal interatomic distances, bond angles, etc. Complementary data can also arise from the combined use of many physical techniques: NMR, electron microscopy, spectroscopy investigations, etc.

4.2.4 Rietveld refinement

Hugo Rietveld proposed this technique back in 1967 [76]. The method requires the knowledge of a structural model, which consists of the approximate atomic positions, and the correct description of the Bragg reflections in the diffractogram, in terms of analytical *profile functions*. It provides the refined atomic positions inside the asymmetric units, starting from the powder diffraction data. The refinement procedure is based on the method of *least squares*.

The powder diffraction experiment yields a diffractogram, which consists of an array of i values y_{io} of the x-ray intensity equally spaced by increments δx of the independent variable x; this parameter could be the angle 2θ, or the photon energy E, depending on the kind of the experiment performed. These data contain the information about the structure factor $F_{\mathbf{H}}$, even though some corrections should be made to extract it (see par. 2.3.3). In the Rietveld method, the experimental data are fitted by the *calculated intensity function,* which includes all these factors:

$$y_{ic} = s \sum_k m_k LP_k \left|F_k\right|^2 G(\Delta x_{ik}) + y_{ib}, \tag{4.1}$$

where k is the index which identifies the reflection, s is a scale factor, m_k is the multiplicity factor; LP_k is the Lorentz polarisation factor, $|F_k|^2$ the square module of the structure factor. $\Delta x_{ik} = x_i - x_k$ is the difference between observed and calculated position of the Bragg peak, corrected for the zero-point shift of the detector; $G(\Delta x_{ik})$ is the reflection profile function and y_{ib} is the background intensity.

The least square method

The best agreement between the observed and calculated data is obtained with the *least square method*, a technique which is widely used in crystallography. It consists of a routine procedure based on the minimisation of the sum of the residuals:

$$S = \sum_i w_i \left|y_{io} - y_{ic}\right|^2 \tag{4.2}$$

by the variation of several parameters in the calculated intensity function, eq. 4.1. In eq. 4.2 y_{io} is the observed intensity in the i step-scan of the acquisition and w_i is a suitable weight (usually identified with the inverse sum of the squares of the standard deviation associated with the peak and that associated with the background intensity). Typical parameters which can be varied in a Rietveld refinement are: the unit cell, the

profile function G (see below), the background function and, of course, the atomic positions in the asymmetric unit.

The profile function

The accurate determination of the peak profile is of fundamental importance, especially nowadays, when the diffraction pattern is often obtained from high resolution synchrotron sources. The G function depends on several parameters: the radiation source, the wavelength distribution in the primary beam, the beam and optics characteristics, the detector system, the response of the sample.

There are many analytical peak-shape functions which are commonly used by the Rietveld routines [50]:

Gaussian: $\frac{C_0^{1/2}}{\pi^{1/2}H_k}exp(-C_0X_{ik}^2)$

Lorentzian: $\frac{C_1^{1/2}}{\pi H_k}(1+C_1X_{ik}^2)^{-1}$

Lorentz.1: $\frac{2C_2^{1/2}}{\pi H_k}(1+C_2X_{ik}^2)^{-2}$

Lorentz.2: $\frac{C_3^{1/2}}{2H_k}(1+C_3X_{ik}^2)^{-3/2}$

Pseudo-Voigt: $\frac{\eta C_1^{1/2}}{\pi H_k}(1+C_1X_{ik}^2)^{-1}+(1-\eta)\frac{C_0^{1/2}}{\pi^{1/2}H_k}exp(-C_0X_{ik}^2)$

PearsonVII: $\frac{\Gamma(\beta)}{\Gamma(\beta-0.5)}\frac{C_4}{\pi}\frac{2}{H_k}(1+4C_4X_{ik}^2)^{-\beta}$

where $C_0=4\ln 2$, $C_1=4$, $C_2=4(\sqrt{2}-1$, $C_3=4(2^{\frac{3}{2}}-1)$, $C_4=2^{\frac{1}{\beta}}-1$ are normalisation factors; $X_{ik}=\Delta x_{ik}/H_k$ and H_k is the full width at half maximum (FWHM) of the k-th reflection. Γ is the Gamma function. As one can easily see, the Pseudo-Voigt function is a mix between a Lorentzian and a Gaussian, determined by the parameter η. The Pearson VII, instead, becomes respectively a Lorentzian, a modified Lorentzian and a Gaussian when $\beta=1,2,\infty$. It exists also the pure Voigt, which is the convolution between a Lorentzian and a Gaussian.

The FWHM, in general is not constant in the diffraction profile, but depends on the x value. According to [77]:

$$(FWHM)_G=(Utan^2\frac{x}{2}+Vtan\frac{x}{2}-W)^{1/2} \tag{4.3}$$

for the Gaussian component, and according to:

$$(FWHM)_L=Xtan\frac{x}{2}+Y/cos\frac{x}{2} \tag{4.4}$$

for the Lorentzian component.

The *background contribution* arises from diffuse or incoherent scattering, amorphous phases in the sample and electronic noise in the detector system. The background function is usually defined by a power series in 2θ, whose coefficients b_r are parameters of the refinement:

$$y_{ib} = \sum_n b_n (2\theta_i)^n \tag{4.5}$$

The agreement factors

An indication of the agreement between the experimental data (y_{io}) and the calculated intensity (y_{ic}) is given by several discrepancy factors, which are listed below:

1. The *profile*: $R_p = \sum |y_{io} - y_{ic}| / (\sum y_{io})$
2. The *weighted profile*: $R_{wp} = [\sum w_i (y_{io} - y_{ic})^2 / \sum w_i y_{io}^2]^{1/2}$
3. The *Bragg*: $R_B = \sum |I_{ko} - I_{kc}| / (\sum I_{ko})$
4. The *expected*: $R_E = [(N - P + C)/(\sum w_i y_{io}^2)]^{1/2}$
5. The *goodness of fit*: $GoF = \sum w_i (y_{io} - y_{ic})^2 / (N - P + C) = (R_{wp}/R_E)^2$

where N is the number of the profile points, P is the number of the refined parameters, C is the number of constraints; w_i is a suitable weight for the i-th step, which usually consists of the inverse of the square standard deviation associated to the i-th step scan. The most meaningful for the monitoring of the progress of the refinement are the weighted profile R_{wp} and the goodness of fit GoF, because their numerator is proportional to the residuals S. The former represents the sum of the square discrepancies, weighted on w_i. The latter should approach the ideal value of unity, and allows to define the expected factor R_E; this represents the theoretical minimum value for R_{wp} which can be obtained. It has been demonstrated that, since R_{wp} and R_p include a background contribution (incorporated implicitly in the observed y_{io} values), they could lead to misleading results if they are obtained from datasets with different background levels. On the contrary, the factors R_B and R_F, based on the integrated observed I_{ko} and calculated I_{kc}, are not influenced by the background, and provide a more suitable check for the validity of the crystal structure.

In summary, the factor R_{wp} is appropriate in order to follow the progress of the structure refinement; the comparison with the expected R_{exp} permits to evaluate the goodness of the fit. But, if a comparison among different datasets is necessary, then

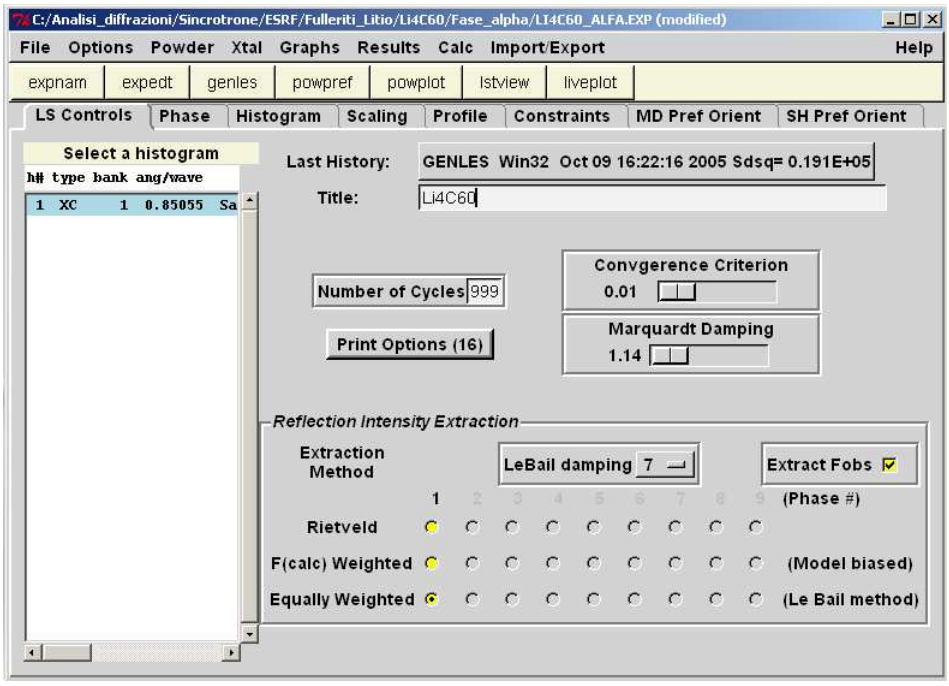

Figure 4.1: A typical window panel of GSAS/EXPGUI.

only the structure model factors R_B and R_F should be used; they provide also a correct evaluation of the structural model.

4.3 Overview of software utilities

During this work, the analysis of powder diffraction data was performed by using two very common software packages, the GSAS/EXPGUI and the FULLPROF suites. Both of them are freeware and easily downloadable from the web. In the next paragraph a brief description of these packages is given.

4.3.1 GSAS/EXPGUI software

GSAS is an acronym for General Structure Analysis System; it was created by Allen C. Larson and Robert B. Von Dreele, of Los Alamos National Laboratory (LANL) in 1985. The program distribution is free and it is available for a series of operating systems (Windows, Unix, Macintosh, VMS) on the web site http://www.ccp14.ac.uk. This suite is a comprehensive system for the refinement of structural models to both x-ray and neutron diffraction data. It can be used to fit powder data either from constant wavelength (CW), or from neutron time-of-flight and energy dispersive x-ray

experiments; but also single-crystal analysis can be performed. Up to 99 different datasets can be used in combination and, for a single sample, a maximum of nine crystallographic phases can be refined. Besides structure determination, GSAS is also used for texture analysis, lattice constant determination and simulation of powder diffraction data.

The GSAS package consists of approximately fifty programs, but the data input is done exclusively through EXPEDT. The latter requires very extensive user interaction, since the parameters can be introduced only by visiting the many levels of shell dialogs. For this reason GSAS is a very complete, but also a rather complex package. In an effort to simplify the package use, in 2001 Bryan H. Toby (of NIST) introduced a General User Interface (GUI), called EXPGUI. It is a free software written as Tcl/Tk scripts. Since the scripts are not pre-compiled, it guarantees high performance and good compatibility. The EXPGUI program consists of a main window (see fig. 4.1), divided into three sections: a *menu bar* on the top, that allows to run the various GSAS programs; a *button bar* just below, that provides a fast access to the most frequently used commands. Finally, in the *bottom section* of the window the contents of the experiment file are displayed. The GSAS/EXPGUI routine needs, as input, two files: the data, in *gsa* format, and an ascii instrumental file. It is easy to convert the *raw* data into the *gsa* file, by the use of the many freely available conversion routines. As far as the second file is concerned, it should provide the starting values of the refined parameters characteristics of the instrument, such as the polarisation factor, the profile coefficients, etc.

4.3.2 FULLPROF suite

FULLPROF was developed at the Saclay-CEA laboratories by Thierry Roisnel and J. Rodriguez Carvajal in 1990. The latest versions of the source code have been developed in Fortran 95, and are freely available on the site: http://www.llb-cea.fr/fullweb/fp2k.htm for the main OS. The program was primarily developed for Rietveld analysis of neutron and x-ray powder diffraction data, both in constant and in variable step of 2θ, but it can be used also for single crystal refinement. The FULLPROF routine is embedded in a suite which includes also the viewer WINPLOTR, a utility which allows to visualise the diffraction profiles (see fig. 4.2).

The main advantage of this suite, as compared with GSAS, is represented by the possibility of form-factor refinement, even for complex objects. In particular, FULLPROF proves particularly suitable for studying molecular crystals, such as fullerides

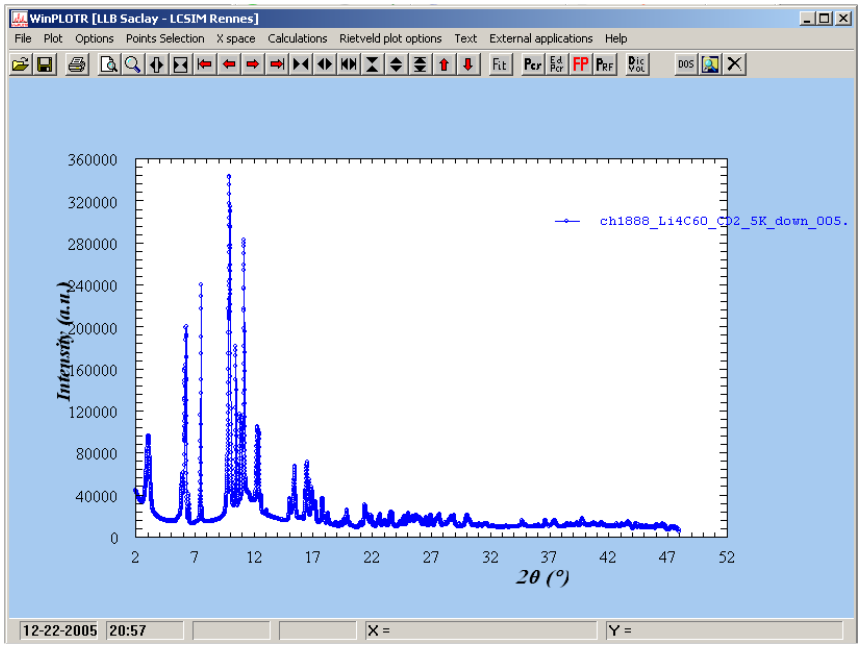

Figure 4.2: A image of WINPLOTR, the viewer of the FULLPROF suite.

in their plastic state, where molecules are in constant motion. The form factor of the molecular unit, in fact, can be modelled either with a series of spherical shells, dense spheres, ellipsoids or disks, or, more accurately, with a series expansion of symmetry adapted spherical harmonics (SASH). On the other hand, FULLPROF generally turns out to be less stable than GSAS and it is more difficult to reach convergence during the refinement.

Moreover, the data input is less user-friendly if compared with the GSAS/EXPGUI software. In this case the two input files needed are the *raw* experimental data and an ascii *pcr* file, containing all the parameters which can be changed (background, atomic positions, profile parameters, etc.). The latter file is updated after each refinement cycle, and can be edited by a generic text editor. Since this step has to be repeated many times during the refinement procedure, it results quite time-consuming.

Chapter 5

Sample preparation

Introduction

An important part of this work was devoted to the preparation of the samples, which was performed in the Fullerene Laboratory, at the Physics Department of the University of Parma. The need of obtaining good quality samples required high attention to avoid to introduce any type of contaminants during the preparation, due also to their extreme sensitivity to air and moisture. In this chapter some information about the reagents (sec. 5.1), the sample handling methods (sec. 5.2) and the main preparation techniques used (sec. 5.3) are given.

5.1 Reagent preparation

C_{60} 99.9 % purity was provided by MER corporation (http://www.mercorp.com/mercorp), whereas lithium and sodium, either in metallic form, or in form of salt, or in form of azide (AN_3), were bought by Sigma-Aldrich (http://www.sigma-aldrich.com) and Strem (http://www.strem.com/code/index.ghc); all the reagents required further purification. C_{60}, before the use, was purified by an annealing at 250° C per 12 hours in dynamic vacuum, in order to eliminate any possible trace of solvents. Lithium azides (see later) were generally supplied in acqueous solution; to obtain the crude compound, it was necessary to evaporate the water. In particular, to extract LiN_3, the product was subsequently dilute in ethanol and then filtered, to eliminate the impurities (usually NaN_3). The final compound was extracted by precipitation, after having added to the solution nine volumes of ether. Alternatively, LiN_3 was obtained by cationic exchange

Figure 5.1: The glove box used for the sample preparation.

in a solution of lithium chloride and sodium azide in ethanol:

$$\mathbf{LiCl + NaN_3 \rightarrow LiN_3 + NaCl}$$

All the organic solvents used in these reaction were absolutely anhydrous, to avoid any water contamination.

5.2 Sample environment

Alkali intercalated fullerides are generally highly sensitive compounds to oxigen and H_2O; even a brief exposition to atmosphere could seriously compromise a sample. Although lithium is the less reactive alkali metal, due its small dimensions, which make its ionic state energetically less favourable (see tab. 5.1), lithium fullerides are extremely sensitive to oxigen and water. For this reason, all the sample manipulations were performed in inhert atmosphere (Ar or He), or under high vacuum (10^{-6} mbar). The reagents and the samples were stored in an Ar filled glovebox M. Braun Labmaster 130, shown in fig. 5.1, capable of mantaining an atmosphere with less than 1 ppm O_2 and less than 1 ppm H_2O. The glass and quartz capillaries, used for diffraction and Raman experiments, were prepared into the glove box; then, they were brought outside with an high-vacuum grase pre-sealing and definitely sealed with a torch, thus

Alkali	Ion. r. (Å)	M. p. (°C)	B. p. (°C)	V. p. (mbar)	E_1 (kcal/mol)
Li	0.6	108.5	1330	$3.78 \cdot 10^{-6}$	124
Na	0.95	97.8	892	$8.64 \cdot 10^{-3}$	119
K	1.33	63.7	760	0.64	100
Rb	1.48	38.9	688	7.07	96
Cs	1.69	28.7	690	21.17	90

Table 5.1: Main physical properties of alkali atoms: the ionic radius, the melting and boiling point, the vapour pressure calculated at 327° C (600 K), the first ionisation energy. The vapor pressure was calculated by the use of the Clausius-Clapeyron equation, except for lithium, for which the value was extrapolated by the Antoine equation.

mantaining an inhert atmosphere inside. The quartz ampoules, used for NMR, EPR and SQUID magnetometry measurements, were filled in the glove box, connected by a silicon tube to a vacuum valve, and then evacuated. They were sealed with a flame (oxigen-acetilene torch), after being filled with He low pressure ($\sim$ 10 mbar), in order to guarantee a good thermal contact during low-temperature measurements.

5.3 Sample preparation

The compounds which were investigated during this work were alkali doped fullerides, both with lithium and sodium, and ammoniated lithium fullerides. In the following sections, a detailed description of the main used preparation techniques is given.

5.3.1 Evaporation of alkali vapours in C_{60} powder

The preparation of alkali intercalated fullerides is generally obtained simply by thermally induced diffusion of the alkali atoms in the fullerene matrix [78, 79]. On one hand, the high electron affinity of C_{60} and the low ionisation potential of the dopants promotes the red-ox reaction; on the other hand, the presence of wide octahedral and tetrahedral voids in the *fcc* fullerite lattice, as compared with the alkali ionic radii, should encourage the diffusion process of the cations (cnf. tab. 1.1 and tab. 5.1). Actually, lithium, with respect other alkali atoms, is somewhat disadvantaged in this processes; besides the relatively high ionisation energy, it shows an very low vapour pressure at the common temperatures normally reached in this solid state reaction, due to the high melting and boiling point; this fact substantially limits the efficiency of this tecnique.

Alkali metal is preliminary reduced in small pieces with cleaned scissors or scalpel;

Azide	Formal ionicity	Solubility	Stability
LiN_3	67	water, alcohol, hydrazine	explodes at T>115°C
NaN_3	70	water	decomposes at 365°C
KN_3	74	water	decomposes at 360°C
RbN_3	74	water, slightly in ethanol	melts and decomposes at 317°C
CsN_3	76	water	melts and decomposes at 326°C

Table 5.2: Some main properties of the alkali azides. The stability of an azide is derived from formal ionicity. LiN_3 results the less stable among alkali azides [80].

then is mixed to a stoichiometric amount of powder of C_{60} in a agate mortar, by grinding for several minutes, until an homogenous powder is obtained. Care is requested to avoid that any amount of alkali metals remains on the mortar and the pestle, thus compromising the correct stoichiometry. The powder is then compressed in several pellets, by the use of a titanium pelletiser, which does not introduce any magnetic impurities in the sample. Hence the pellets are placed in tantalum small bags, and sealed under vacuum in a Pyrex ampoule. Finally they undergo a thermal annealing for three weeks at 270°C (543 K). Several intermediate regrindings are required to improve the homogeneity of the sample.

5.3.2 Thermal decomposition of lithium azide

A more efficient method, which permits to intercalate lithium atoms in the host fullerene lattice, is based on the use of lithium azides LiN_3. Metal azides are metastable compounds which easily react and explode, either spontaneously or after a shock, thus returning the metallic species and gaseous nitrogen. Depending on the metallic species involved, the stability of the compounds is different and changes with the *ionicity* of the elements-to-azide bonds: ionic azides are rather stable, heavy-metal azides explode quite easily, whereas covalent azides explode spontaneously [80]. The exothermal reaction can also happen in a safe way, for example by a slow-ramp thermal treatment; the result is a slow decomposition of the metal azides, which can be controlled in laboratory. In the tab. 5.2 the main physical and chemical properties of alkali azides is summarised.

Lithium azide is a white, highly hygroscopic water soluble salt. It can be obtained in several ways, as previously discussed [80]. It is the most reactive, among the alkali azides and the anidrous form explodes on thermal shock above 115° C; slow heating can increase the explosion temperature to about 298° C.

Stoichiometric amounts of LiN_3 and powdered C_{60} are mixed in the mortar until an homogeneous compound is obtained. The obtained powder is compressed in pellets, and termally treated in dynamical vacuum with a slow ramp, controlled by a PC connected to the oven; the experimental apparatus used was schematically represented in fig. 5.2a. The reaction, which can be schematically rapresented as:

$$\mathbf{C_{60} + x \cdot LiN_3 \rightarrow Li_xC_{60} + \frac{3}{2}x \cdot N_2}$$

was monitored by measuring the variation of pressure in the vacuum system during the annealing.

In fig. 5.2b both the thermal ramp and the measured pressure during the reaction are displayed; the azide decomposition is evidenced by the presence of a pressure peak. A further check of the sample comes out from the evaluation of the shape of the peak: good reaction is usually characterised by a narrow symmetrical peak. A further annealing for several hours improves the crystallinity of the sample.

With the thermal decomposition of lithium azide, a well crystallised sample could be obtained in approximately 25 hours, with respect ~ 3 weeks requested for the alkali diffusion, without significant differences in the obtained compound quality, as discussed in chap. 6.

5.3.3 Reactions with ammonia

Alkali metals dissolve easily in liquid ammonia; the resulting solutions were subject to extensively studies, due to their noticeable properties, such as their very low density and metallic behaviour [81, 82]. Concerning lithium, the A^+ cations are placed a well defined solvatation shell of coordinated NH_3 molecules [82], and the delocalized electrons give rise to a typical blue or bronze coloration of the liquid, depending on the concentration of the alkali.

C_{60}, which is not soluble in liquid ammonia, can enter in solution when it is in the anionic forms C_{60}^{n-} [83]. During this reaction, the intercalation of the alkali atoms in this case is accompanied also by that of ammonia, which generally plays an active role in the final product.

Anhydrous gaseous ammonia is condensed into a previously evacuated Schlenk tube containing alkali metal and powder of C_{60}, dipped into a methanol bath, which is maintained at the temperature of $\sim -70°$ C, by the use of a refrigerator. In fig. 5.3a the system of the vacuum-gas line and the cool bath is shown. The solution of the

metal is monitored by the typical coloration of the liquid. A quartz coated magnetic stirrer provides the necessary mixing of the reagents. Then the system is isolated and the temperature of the bath is progressively increased up to $\sim -35°$ C (at this temperature NH_3 vapour pressure is $\sim$ 1 bar); these conditions are maintained for $1-2$ hours, to let the reaction take place. As a next step, the excess of ammonia is pumped away, through the vacuum line. The amount of ammonia in the final product is controlled by warming the sample and by varying the pumping time. Finally, the obtained compound is removed from the Schlenk.

Alternatively, intercalation of NH_3 in lithium fullerides was also obtained by direct exposure of Li_xC_{60} samples to ammonia vapours. In this second case, a known mass of compound was placed in a tantalum vessel, then introduced into a Pyrex flask, by handling in inert atmosphere. To improve the ammonia uptake, the flask, after having been connected to the vacuum-gas line and evacuated, is heated up to $\sim 190°$ C (see sect. 6.4). Hence, the system was connected to a reservoir filled with ammonia, with a known volume, whose pressure is continuously monitored (see fig. 5.3b). A sizeable ammonia uptake is initially observed, indicated by the variation of pressure in the reservoir and the exactly amount of NH_3 can be easily determined by the knowledge of the thermodynamical parameters. The sample is then cooled at room temperature. Subsequent pumping cycles at various temperatures are performed on the sample, in order to modify the amount of ammonia in the final product. The heating of the flask, depending on temperature range considered, is obtained by thermal baths with ethanol ($T< 10°$ C) or water ($T= 10-90°$ C), or by the use of an oven ($T> 90°$ C).

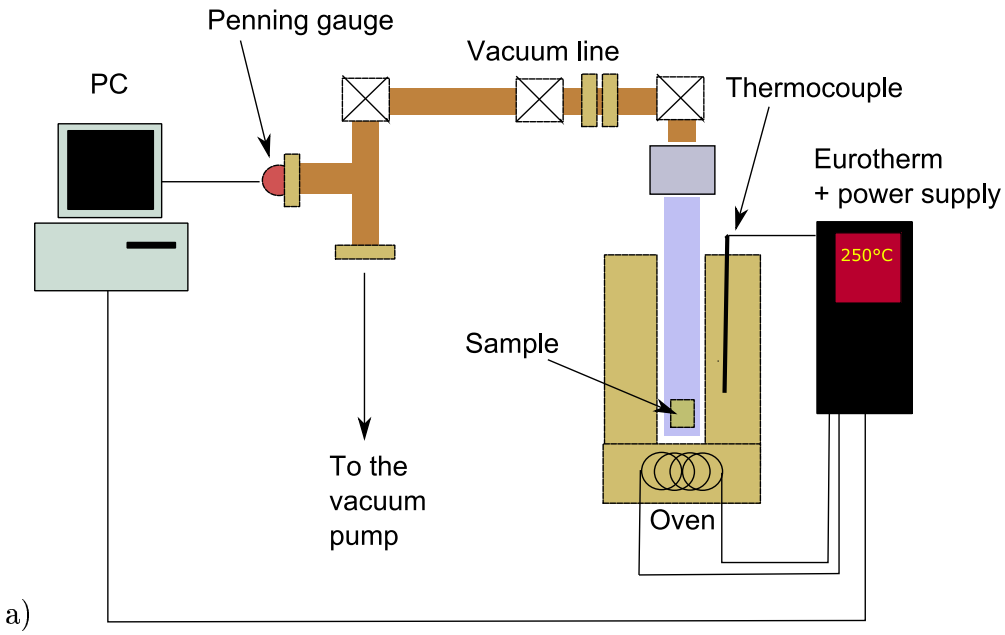

a)

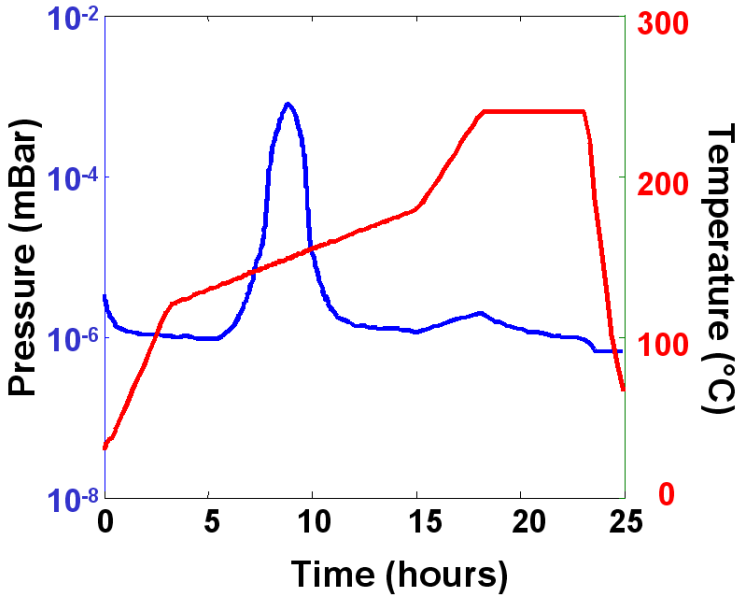

b)

Figure 5.2: a) The schematic diagram of the experimental apparatus used for the azide decomposition. b) The time evolution of the experimental parameters during the thermal decomposition of LiN_3 for the preparation of Li_4C_{60}: the *red* curve represents the sample temperature, whereas the *blue* curve shows the peak of pressure during the decomposition.

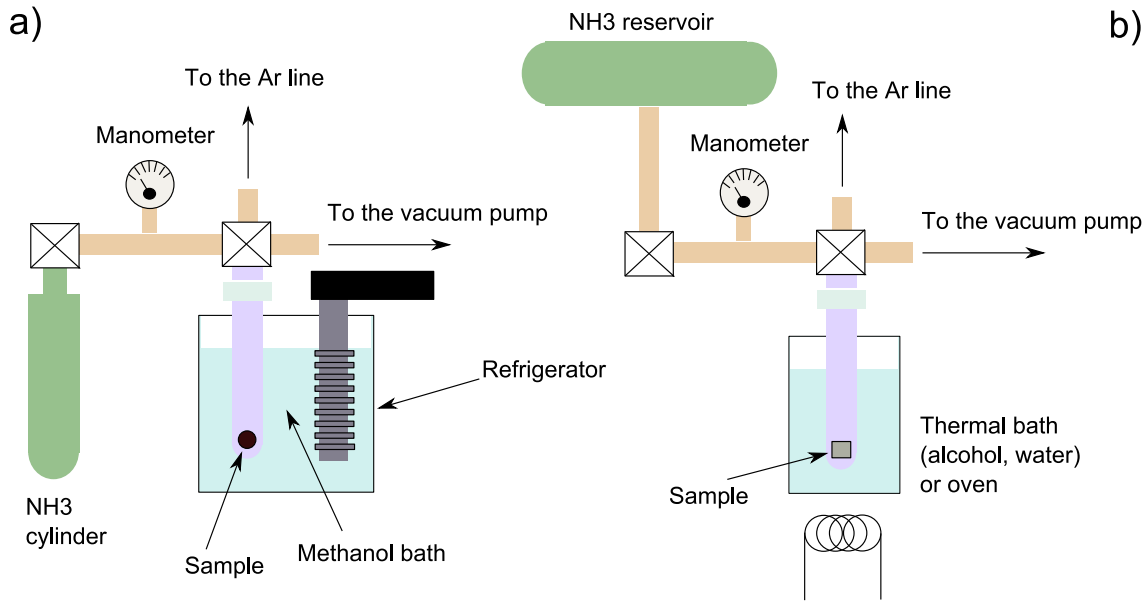

Figure 5.3: The schematic representation of the experimental set-up used during the reactions with ammonia; in a) the reaction is performed at low temperature ($\sim -35°$ C) in liquid ammonia, whereas in b) the uptake is obtained by exposition of the sample to NH_3 vapours.

Chapter 6

Experimental results

Introduction

In this chapter the experimental results obtained in this work are presented and discussed. The preliminary x-ray measurements were performed in the XRD laboratory of the University of Parma, whereas synchrotron data were collected mainly at the ESRF facility (Grenoble, Fr), and part at the Swiss Light Source facility (Zurich, CH). Raman spectroscopy was carried out at the ISMN-CNR Institute of Bologna. In order to give a more complete framework and to support the results achieved with these techniques, also some NMR, SQUID magnetometry and ESR measurements were presented, which were more extensively discussed in [12]; NMR/MAS measurements were performed at the Laboratory of Physical Chemistry ETH (Zurich, CH), whereas SQUID magnetometry was arranged in the SQUID laboratory of the University of Parma. Finally, ESR measurements were carried out at the Jozef Stefan Institute of Ljubljana (Slo).

In the first section (sec. 6.1), the complete structural analysis on the as-prepared Li_xC_{60} series with $1 \leq x \leq 6$ was presented in several steps: first, a preliminary investigation with laboratory CuK_α diffractometer is analysed; then, the *ab-initio* resolution of the Li_4C_{60} structure, a representative of these class of compounds, starting from synchrotron powder data, is treated in detail. Finally, the confirmations to the proposed structural model, coming from complementary NMR/MAS and Raman tecniques are presented and discussed. In the next section (sec. 6.2), the thermal evolution of Li_4C_{60} was studied by the use of high resolution powder diffraction data, and the parallel ESR investigation at high temperature was presented. The noticeable results emerged during this step induced to investigate accurately the high-temperature phase of Li_4C_{60}, by performing a structural analysis from high resolution synchrotron powder diffrac-

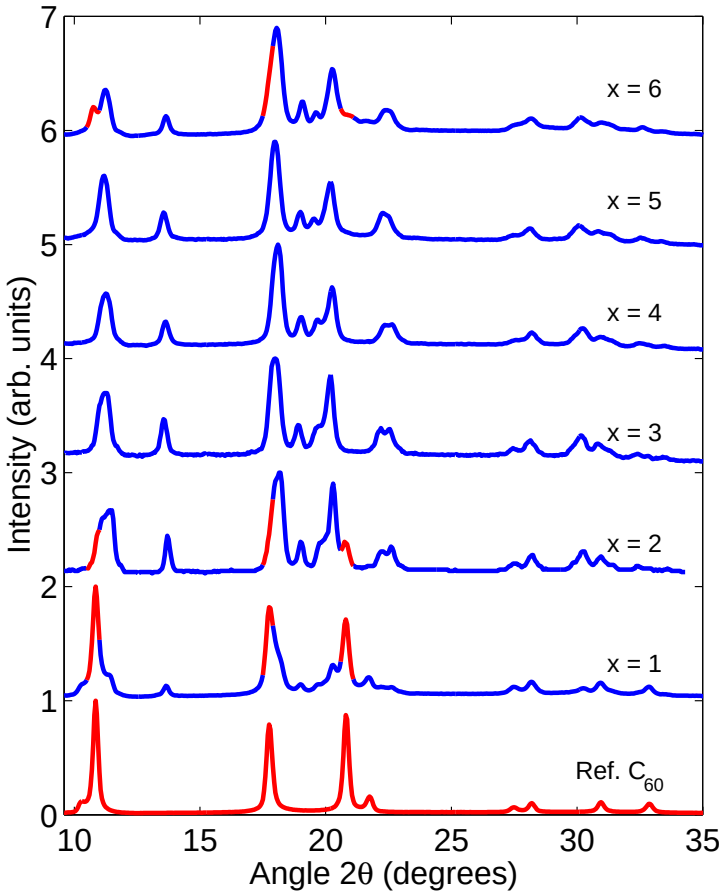

Figure 6.1: The laboratory x-ray diffraction patterns of the series Li_xC_{60} with $1 \leq x \leq 6$ (CuK_α). Only for $3 \leq x \leq 5$ the samples appear homogeneous and without unreacted C_{60}.

tion and Raman spectroscopy (sec. 6.3). The sec. 6.4 is devoted ot the study of the compounds obtained from the ammoniation of lithium fullerides; the investigation was supported either by x-ray diffraction and by SQUID magnetometry. Finally, in the last section (sec. 6.5), a preliminary structural and electronic investigation of the $Li_xNa_{4-x}C_{60}$ ($0 \leq x \leq 4$) series is presented.

6.1 Structural investigation of Li_xC_{60} ($1 \leq x \leq 6$)

6.1.1 Preliminary x-ray characterisation

The series Li_xC_{60} with $1 \leq x \leq 6$ was obtained both by evaporation of the alkali metal and by the thermal decomposition of lithium azides, as described in chap. 5. The

samples underwent a preliminary investigation with laboratory CuK_α x-ray diffraction at room temperature. At the level of resolution reached by the diffractometer ($\sim 0.05°$/step), both the two categories of samples appeared well crystallised and with practically the same structure (a more detailed comparison, starting from synchrotron data, will be made later). In fig. 6.1 the powder diffraction patterns of the whole series are shown. For the lowest stoichiometries, $x = 1, 2$, it is well visible the presence of an unreacted C_{60} phase, which is evidenced in *red* in the figure; to make easier the comparison, also the diffraction pattern of pristine C_{60} is displayed at the bottom. A similar spurious phase is present also for $x = 6$, even if the low angular resolution of the measurement does not allow to exclude the possibility that these peaks actually belong to another cubic phase, due for example to the lithium clusterisation [10]. On the contrary, for $x = 3, 4, 5$ the samples appear homogeneous and without unreacted C_{60}. Moreover, the spectra of this subgroup are practically the same, thus showing that the corresponding structure is quite insensitive to the amount of lithium in this range of doping.

From this preliminary analysis, it is clear that Li_4C_{60} is the representative of this class of compounds; for this reason, the following investigation will be focussed mainly on this compound.

The Li_4C_{60} laboratory powder pattern underwent a further investigation, in order to check on this sample the structures proposed in literature [9, 11]. The previous two analyses, both based on laboratory powder x-ray data, suggests that Li_4C_{60} should display a body centered tetragonal structure, in which the $h + k + l = 2n$ condition is satisfied as shown in tab. 6.1:

Li_4C_{60} structure	Refl. conditions	*a* (Å)	c (Å)	Ref.
bct	$h + k + l = 2n$	9.13(3)	14.85(7)	Wågberg et al. [11]
bct	$h + k + l = 2n$	9.33(2)	14.94(5)	Yasukawa et al. [9]

Table 6.1: A comparison between the two proposed structural model for Li_4C_{60} in [**?**, 9].

the low value of the C_{60}-C_{60} distance along the a direction seems to be compatible with a two-dimensional polymerisation of the compound, in which each C_{60} unit is linked to the four first-neighbours by [2+2] cycloaddicted bonds, as shown in fig. 1.7b. This bonding motif is analogous to that of polymerised tetragonal C_{60} [36, 84].

Nevertheless, the results of the two analyses disagree and are rather questionable. In fact, the planar C_{60}-C_{60} distance, corresponding to the a parameter, is profoundly

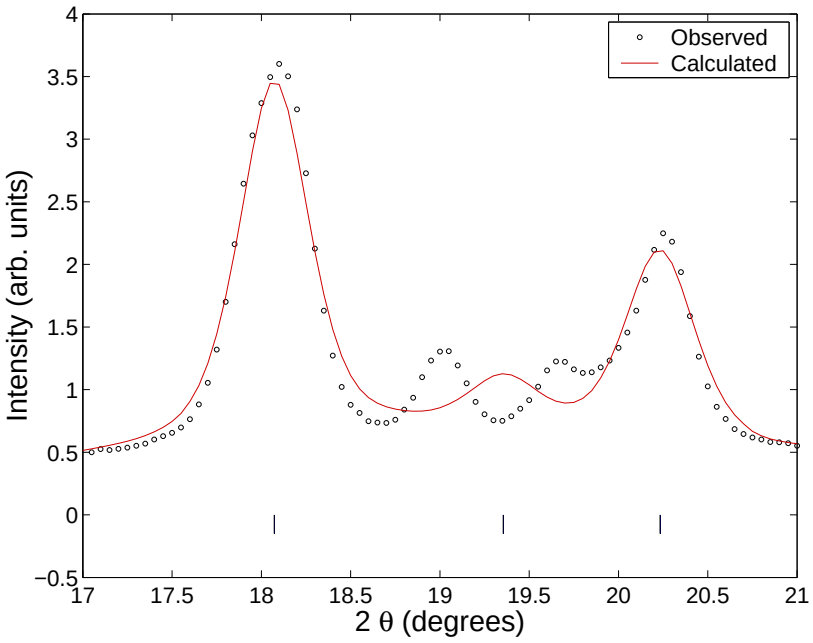

Figure 6.2: Comparison between measured (o) and fitted (solid line) powder diffraction profile of Li_4C_{60}, basing on a tetragonal cell (spatial group $\mathbf{I4}$). The ticks mark the refined reflections. The proposed model clearly does not match the diffractogram in the region $2\theta = 18.5° - 20°$.

different in the two cases; the value indicated by Wågberg et al. could be compatible with a two bridged bond, even if the value would be an upper limit. But the very high value obtained by Yasukawa et al. is hard to be referred to a cycloaddition distance ($\sim$ 9.1 Å in AC_{60}, A=K, Rb; $\sim$ 9.02 Å in polymeric C_{60}). The profile of Li_4C_{60} diffractogram in fig. 6.1 is almost identical to that obtained by Wågberg et al.. However, if the experimental reflections are compared to those simulated, only the most intense peaks are correctly predicted, whereas strong discrepancies are present at $2\theta = 18 - 20°$ (see fig. 6.2), thus indicating that a tetragonal cell is probably not correct. Because of the low resolution of the laboratory diffractometer, a deeper investigation was not allowed.

6.1.2 Synchrotron powder x-ray diffraction on Li_4C_{60}

As-prepared Li_4C_{60}, obtained from thermal decomposition of lithium azides, was investigated by synchrotron x-ray powder diffraction at the ESRF, beamline ID31. The wavelength used was fixed at $\lambda = 0.85066$ Å, a value chosen to maximise both the angular resolution and the number of reflections collected. The obtained diffractogram

is characterised by quite broad peaks and a non negligible background contribution; these are typical features of powder patterns obtained with fullerides, in which there is always a certain amount of disorder in the structure. Nevertheless, the peaks results sufficiently intense to certify a good crystallinity level of the sample.

Thanks to the high resolution of the diffractometer, the ambiguity of the previous analysis can be resolved. The obtained powder pattern shows that many "single" peaks of the preliminary laboratory diffractogram actually consist of group of different reflections, thus indicating that, if the sample is a single phase, the cell symmetry is probably lower than tetragonal.

Powder pattern indexing and powder pattern decomposition

The *ab-initio* investigation of Li_4C_{60} structure was performed in collaboration with Prof. Serena Margadonna, during a stage at the Chemistry Department of the University of Cambridge (UK).

The study started from the indexing of the powder reflections, extracted from synchrotron data collected at room temperature. The positions of the peaks were first refined with a fitting program; hence they were analysed with the DICVOL91 routine. To favour the convergence of the program, the number of the processed peaks was progressively increased. The program converged rapidly to one solution, and the proposed cell was monoclinic.

The obtained data were successfully checked by the powder pattern decomposition, performed with GSAS/EXPGUI. The extraction of the integrated intensities permitted to determine the correct space group, by checking the systematic extinctions. The proposed space group is $\mathbf{I\,1\,2/m\,1}$, which is one of the maximum non-isomorphic subgroups of the tetragonal group $\mathbf{I\,4/m\,m\,m}$ [85]. Le Bail analysis provided the refined values of the cell parameters and the profile: $a = 9.3267(3)$ Å, $b = 9.0499(3)$ $c = 15.03289(1)$ and $\beta = 90.949(3)^\circ$ ($R_{wp} = 4.24\%$, $R_{exp} = 1.53\%$).

Focussing now on Li_4C_{60} cell parameters, several considerations can be made. First of all, the cell is monoclinic, but actually the parameter values indicate that it is obtained by a slight distortion of a tetragonal cell: in fact the a and b edges are similar, and β is near to 90°. Moreover, by assuming that C_{60} units are centred in the points of the lattice, a and b result very small distances, even smaller than the outer diameter of C_{60}. This is a strong hint that Li_4C_{60} is polymerised. In particular, the distance along b axis is typical of [2+2] cycloaddition bond (see before). The contact of buckyballs along the a axis, on the contrary, represents an upper limit for polymerisation in fullerenes,

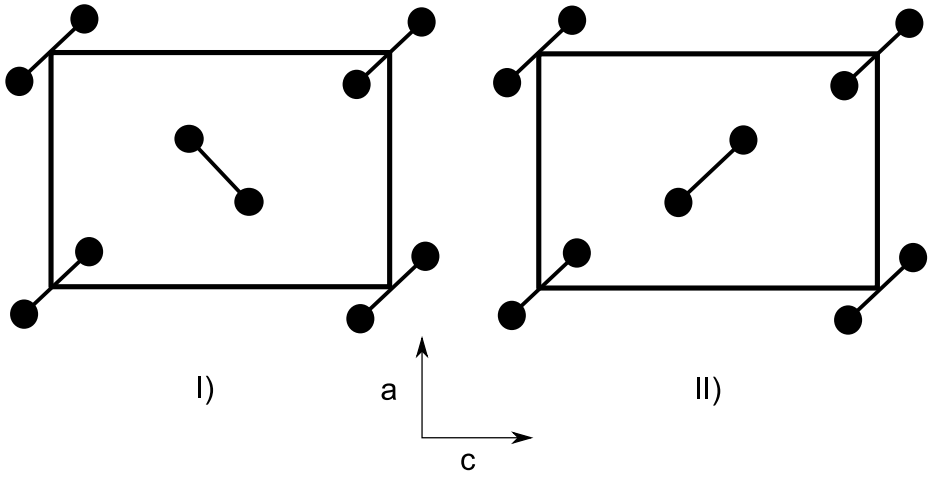

Figure 6.3: Two possible orientations of the polymeric chains in AC_{60} compounds: I) corresponds to KC_{60}, which presents a primitive orthorhombic structure, whereas II) is the arrangement in RbC_{60}, with a monoclinic body-centered cell.

and it will be discussed in detail later. The c axis is probably the stacking direction; its value causes a C_{60}-C_{60} contact between fullerene units along the diagonals of the polyhedron of ~ 9.95 Å, a typical value found in monomeric fullerenes.

The next step consisted in the introduction of the atoms in the structure.

Structure solution

The similarity between Li_4C_{60} and RbC_{60} structures induced to assume the latter as a good starting point for the structural analysis. In fact, both present the same spatial group and the presence of a short center-to-center C_{60} contact, compatible with a cycloaddicted bond, as shown in tab. 6.2.

Sample	**S. G.**	**a**	**b**	**c**	β	Ref
KC_{60}	**P n m n**	9.9525(09)	9.0917(08)	14.3740(12)	90°	[86]
RbC_{60}	**I 1 2/m 1**	10.1257(03)	9.0865(01)	14.2070(04)	90.317(02)°	[86]
Li_4C_{60}	**I 1 2/m 1**	9.3267(3)	9.0499(3)	15.03289(1)	90.949(3)°	This work

Table 6.2: The lattice parameters for the one-dimensional polymers KC_{60} and RbC_{60}, compared with those obtained for Li_4C_{60} from Le Bail analysis from synchrotron data.

The starting carbon atomic positions were chosen as in the work of Huq et al. [86], which performed high resolution neutron powder diffraction on both KC_{60} and RbC_{60}. RbC_{60} structure consists of one-dimensional chains, connetted by four membered car-

bon rings. The monoclinic body-centered cell imposes the same orientation for all the chains, unlike the primitive orthorhombic structure of KC_{60}, in which the chains orientations are alternate along the c packing direction (see fig. 6.3) [5].

First, the atomic coordinates of the asymmetric unit were transformed accordingly with the geometry of the Li_4C_{60} cell. Note that the symmetries of the spatial group do not put any constraint on the orientation of the chains. Hence, the next step of the investigation consisted in searching the best atoms arrangement, by rotating the polymeric chains along their axis in step of 5°, and at the same time monitoring the agreement with the experimental data by simulating the corresponding diffraction pattern. In fig. 6.4a the agreement factors of the fit, with respect the axial rotational angle ϕ in the range $0 - 180°$ are shown (the two-fold axis of the $\mathbf{I\,1\,2/m\,1}$ symmetry guarantees the same behaviour for the range $180 - 360°$). $\phi = 0$ corresponds to the four carbons of the polymeric ring lying in the bc plane. The R_{wp} value has a strong minimum for $\phi = 100°$; in this case, the simulated profile reproduces quite well the experimental pattern also at highest 2θ, where the information about the details of the electronic density are present. The obtained structure consists then of linear polymeric chains, where the plane detected by the cyclobutane rings curiously forms an angle of only 10° with the ab plane.

It is important now to point out that, for this particular atomic arrangement, buckyballs belonging to neighbouring chains bring a couple of carbons (shared by one pentagon and two hexagons) very close (see fig. 6.4b); thus, a further bond could be extablished between the distorted C_{60} units. To shed light on this guess, a Rietveld refinement of the atomic positions was performed.

Rietveld refinement

An accurate Rietveld refinement of as prepared Li_4C_{60} was performed with the EXPGUI suite. The analysis started from the carbon atomic positions obtained from the previous investigation, in which RbC_{60} polymeric chains are slightly rotated with respect the ab plane. In the first step, lithium atoms are neglected; in fact, due to its small electronic density, as compared to C_{60}, lithium presence represents only a very small perturbation in the x-ray scattering factor of the sample. With this starting carbon positions, the fit provided a relatively poor agreement ($R_{wp} \sim 10\%$).

Hence the carbon positions of the cage were allowed to vary; soft constraints [56, 50] on the C-C distances and on the angles, based on the typical values of the fullerene cages, were fixed, in order to avoid that the refinement diverges. Moreover, the obtained

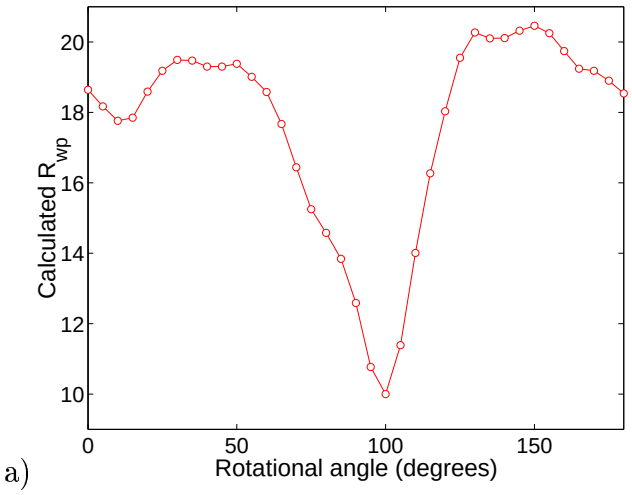

a)

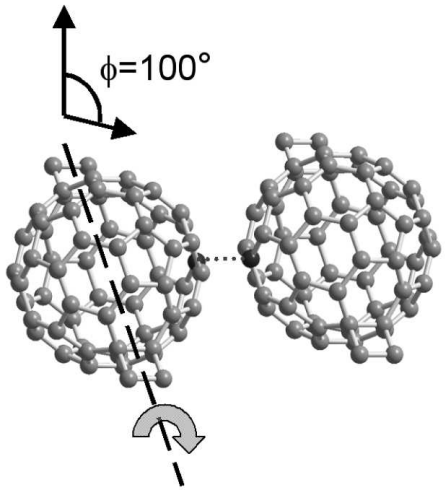

b)

Figure 6.4: a) Evolution of fit residuals as fullerene molecules rotate along the chain axis. A Strong minimum is observed for $\phi = 100°$, when b) neighbouring buckyballs bring a couple of carbon atoms very close.

results were continuously checked, after each cycle, so that unrealistic cage distortions in the model could not form. The strategy followed was: first, the position of C15 atom (see fig. 6.5a), suspected to be involved in the further bond, was refined. Then the first neighbours, C16 and C5, and finally the whole asymmetric unit (16 atoms). During the refinement, a strong improvement of R_{wp} and R_{F2} was noted, and the constraint factors values progressively decreased, until a stable condition was reached.

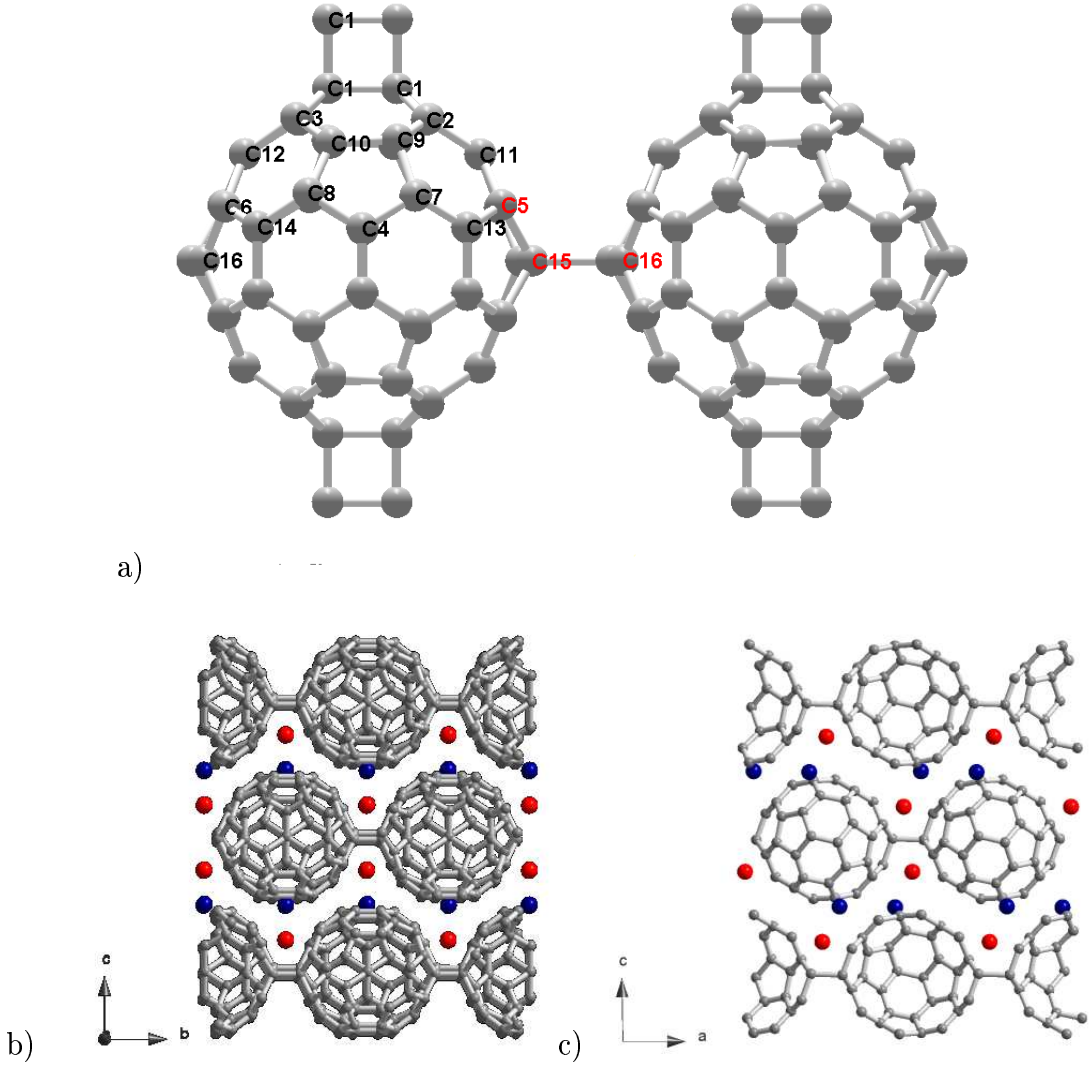

Figure 6.5: a) The schematic representation of the carbon atoms involved in the Rietveld refinement. b) The position of lithium atoms, as identified by the use of Fourier maps: alkali atoms in pseudo-octahedral voids are in *red*, while those in pseudo-tetrahedral are in *blue*.

The final step consisted in the introduction of the lithium atoms. Fourier difference analysis performed with the GSAS routine [56] allowed to locate electronic density in correspondence of the pseudo-tetrahedral and pseudo-octahedral sites, derived by transformation of the tetrahedral and octahedral voids of the *fcc* fullerite lattice (see fig. 6.5b and c). The position refinement indicated that the pseudo-octahedral void is occupied by two lithium atoms, placed symmetrically to the center. The occupancies of the two crystallographic positions are compatible with a stoichiometry $x \sim 3.49$,

whereas the refined temperature factors indicated an extremely high mobility of the small alkali atom ($B_{iso} \sim 11$ Å^2); this value is in agreement with the ^{7}Li NMR measurements performed on these systems, in which a single motional narrowed line was observed [87]. The final C15-C15 distance obtained is ~ 1.75 Å, a value compatible with a single C-C bond between buckyballs. Hence the proposed structure of as prepared Li_4C_{60} is that of an unusual two-dimensional polymer, in which two different bonding motives, both [2+2] cycloaddicted four membered carbon rings and single C-C bonds, coexist. These two different bonds propagate along two orthogonal directions, thus giving rise to a planar network, as shown in fig. 6.6a., whereas in fig. 6.6b the final result of the Rietveld refinement on Li_4C_{60} is displayed. In tab. 6.3, the extracted structural parameters of as prepared Li_4C_{60} are summarised.

Dependence on the preparation

Previous analysis was performed on a sample obtained by thermal decomposition of lithium azides. Subsequent high resolution powder x-ray diffraction performed also on Li_4C_{60} obtained by thermal evaporation of alkali metal substantially confirmed the preliminary laboratory analysis, thus indicating that both the two types of preparation lead to a similar structure. Synchrotron powder pattern of the sample achieved with the "traditional" technique appears substantially identical to that obtained with thermal decomposition of lithium azides. At a more accurate analysis, it shows more narrow and resolved reflections at the lowest angles, due to a better crystallinity, but at the same time evidenced the presence of several "bumps" in the background profile, which could be ascribed to a minoritary unknown phase, which occasionally superimpose to the main phase, as subtle "shoulders". The difficulties encountered in isolate this contribution substantially did not allow to perform an accurate structural investigation on this sample; nevertheless, the agreement of these data with the Li_4C_{60} structural model is quite satisfactory as well, as shown in tab. 6.4.

Low temperature measurements

Synchrotron diffraction at low temperature was performed on as prepared Li_4C_{60}, in order to investigate possible structural changes of the polymer. The diffraction profile collected at 5 K perfectly matches the data at room temperature, thus indicating that no structural phase transitions occur at low temperature (see tab. 6.4). The lattice parameters show a very weak contraction along a and b direction in the range $300-5$ K (respectively 0.023(3)% and 0.024(3)%), about one order of magnitude with respect the

c stacking direction (0.209(3)%), thus confirming the proposed 2D polymeric nature of the compound.

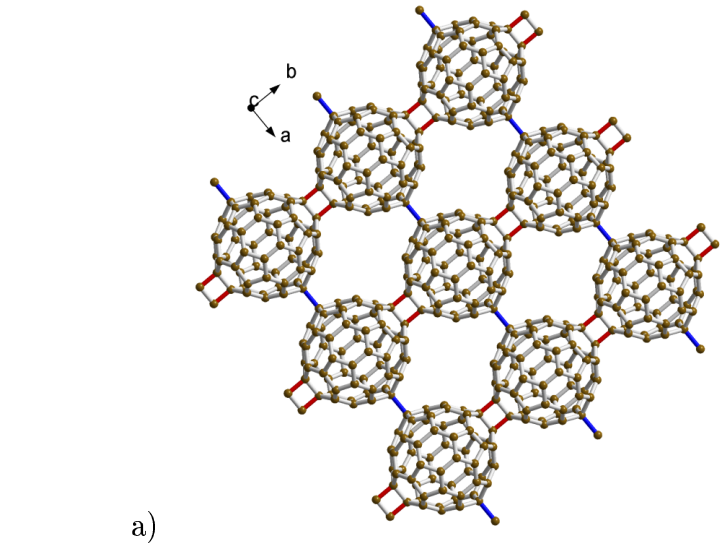

a)

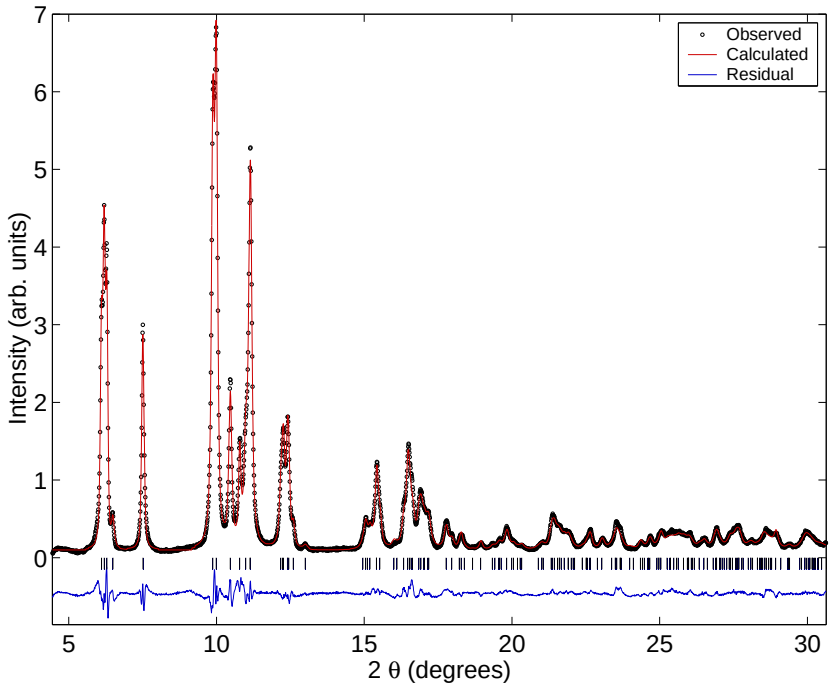

b)

Figure 6.6: a) An image of the 2D structure of as-prepared Li_4C_{60}; the two different types of bonds, either single (in *blue*) or "double" (in *red*), propagate along two orthogonal direction. b) Measured (o) and calculated (solid line) powder diffraction pattern of Li_4C_{60} at 300 K. The lower solid line in *blue* shows the difference profile, whereas the ticks mark the reflection positions.

Atom	**n**	**x**	**y**	**z**	**Position**	B_{iso} (Å^2)
C(1)	1	-0.083(1)	0.418(1)	0.011(1)	*8j*	1.01(6)
C(2)	1	-0.170(2)	0.337(1)	-0.056(1)	*8j*	1.01(6)
C(3)	1	-0.123(1)	0.343(1)	0.098(1)	*8j*	1.01(6)
C(4)	1	-0.072(1)	0.078(1)	-0.221(1)	*8j*	1.01(6)
C(5)	1	-0.350(1)	0.135(1)	-0.056(1)	*8j*	1.01(6)
C(6)	1	-0.283(1)	0.129(1)	0.136(1)	*8j*	1.01(6)
C(7)	1	-0.185(1)	0.155(1)	-0.179(1)	*8j*	1.01(6)
C(8)	1	-0.058(1)	0.161(2)	0.216(1)	*8j*	1.01(6)
C(9)	1	-0.130(1)	0.292(1)	-0.143(1)	*8j*	1.01(6)
C(10)	1	-0.022(1)	0.283(2)	0.162(1)	*8j*	1.01(6)
C(11)	1	-0.285(1)	0.257(1)	-0.012(1)	*8j*	1.01(6)
C(12)	1	-0.253(1)	0.258(1)	0.084(1)	*8j*	1.01(6)
C(13)	1	-0.295(1)	0.080(1)	-0.139(1)	*8j*	1.01(6)
C(14)	1	-0.184(2)	0.081(1)	0.201(1)	*8j*	1.01(6)
C(15)	1	-0.407(1)	0	-0.002(1)	*4i*	1.01(6)
C(16)	1	-0.347(2)	0	0.095(1)	*4i*	1.01(6)
Li(1)	0.980(20)	0.416(6)	0	0.748(5)	*4i*	11(1)
Li(2)	0.1765(17)	0.023(7)	0	0.380(5)	*4i*	11(1)

Selected distances	**Distance (Å)**	**Notes**
C(1)-C(1)	1.59(2)	distance between two C_{60} bridged by "double" bonds
C(1)-C(1)	1.49(2)	On-ball distance within the four-membered ring
C(1)-C(2)	1.47(1)	
C(1)-C(3)	1.52(1)	
C(9)-C(10)	1.45(1)	
C(2)-C(11)	1.46(1)	
C(11)-C(5)	1.42(1)	
C(5)-C(15)	1.55(1)	
C(15)-C(16)	1.55(2)	
C(16)-C(6)	1.45(1)	
C(6)-C(12)	1.43(1)	
C(12)-C(13)	1.45(1)	
C(15)-C(15)	1.75(2)	distance between two C_{60} bridged by single bonds
Li(1)-C(6)	2.45(6)	
Li(1)-C(10)	2.43(4)	
Li(1)-C(14)	2.42(5)	
Li(1)-C(16)	2.45(6)	
Li(2)-C(4)	2.54(6)	
Li(2)-C(8)	2.95(6)	
Li(1)-Li(2)	4.49(8)	
Li(2)-Li(2)	3.65(14)	distance between Li^+ ions in the octahedral void

Table 6.3: Refined parameters and selected bond distances of Li_4C_{60}, by Rietveld refinement of synchrotron data at 300 K. The symmetry of the lattice is described by the space group $\mathbf{I\,1\,2/m\,1}$, and the cell parameters are: $a = 9.3264(4)$ Å, $b = 9.0478(4)$ Å, $c = 15.03294(2)$ Å, $\beta = 90.967(3)°$. The agreement factors are: $R_{wp} = 5.12\%$, $R_{exp} = 1.53\%$, $R_{F2} = 3.46\%$ [88].

Other stoichiometeries

High resolution synchrotron powder diffraction at room temperature was performed on the series Li_xC_{60} with x = 3, 3.5, 4.5, 5 at the Swiss Light Source (Zurich, CH). The obtained diffraction profiles for these stoichiometries do not show any particular difference with respect to Li_4C_{60}. The cell analysis, performed with Le Bail pattern decomposition, indicates that no significant changes in the intermolecular distances occur, thus confirming the substantial independence of the structure from the lithium amount. The results are summarised in tab. 6.4.

Sample	a	b	c	β	R_{wp}(%)	R_{F2}(%)	T **(K)**	**Pr.**
$\mathbf{Li_4C_{60}}$	9.3145(1)	9.0546(1)	15.0004(2)	90.930(2)	7.61	10.21	300	E
$\mathbf{Li_4C_{60}}$	9.3124(2)	9.0524(2)	14.9690(4)	90.872(2)	7.49	10.76	5	E
$\mathbf{Li_3C_{60}}$	9.3331(5)	9.0223(5)	15.0216(7)	91.106(3)	3.96		300	A
$\mathbf{Li_{3.5}C_{60}}$	9.3212(2)	9.0317(2)	15.0036(3)	90.993(1)	3.19		300	A
$\mathbf{Li_{4.5}C_{60}}$	9.3055(2)	9.0446(2)	14.9933(3)	90.967(2)	5.28		300	A
$\mathbf{Li_5C_{60}}$	9.3095(3)	9.0793(4)	15.0003(5)	90.891(3)	4.35		300	A

Table 6.4: Refined data from synchrotron radiation diffraction for Li_xC_{60}, x = 3, 3.5, 4, 4.5, 5. In the last column the type of preparation is shown: E indicates intercalation by evaporation of Li in fullerene matrix, whereas A indicates intercalation by thermal decomposition of LiN_3.

6.1.3 Complementary ^{13}C NMR/MAS measurements on Li_4C_{60}

The structure of as prepared polymeric Li_4C_{60} is rather interesting because of the unusual coexistence of both single and "double" C-C bonding schemes in the polymeric network. This model hence required also another strong proofs, which were provided by nuclear magnetic resonance and Raman spectroscopy. ^{13}C NMR, both in static and magic angle spinning (MAS) configuration, were performed on the sample at room temperature.

In the static case, the data obtained (not shown here) consist of a broad spectrum, with a line-shape typical of a chemical shielding powder pattern [12, 89]. The lack of the motional narrowing, which on the contrary is observed in C_{60} at room temperature, is a clear confirmation that the compound is polymerised.

The dynamical MAS measure provides much more evidences to the proposed structural model. In fig. 6.7, the spectrum obtained with a 8 KHz spinning rate is shown. The "magic angle spinning" configuration allows to mediate to zero all the anisotropic contributions of the chemical shift [90]; hence the resultant spectrum consists of narrow

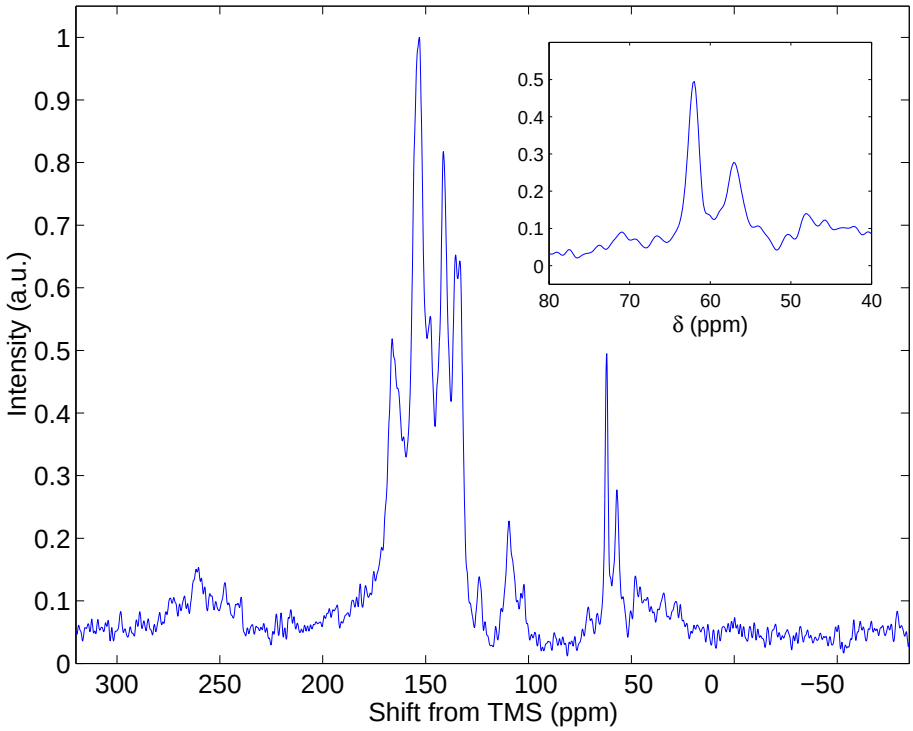

Figure 6.7: ^{13}C NMR/MAS spectrum at 300 K of Li_4C_{60}. The main group of peaks centered at $\sim$ 150 ppm is due to sp^2 hybridised carbons of the distorted fullerene cage. Inset: the two peaks in the sp^3 region, due to the two different types of polymerisation.

resonances, whose shift from the reference (TMS) depends on the chemical environment [12]. In particular, two main groups of peaks, centered respectively at $\sim$ 150 ppm and $\sim$ 60 ppm, are well visible; the former arises from the sp^2 hybridised carbons forming the cage, whereas the latter falls in the typical region of the sp^3 carbons and represents the contribution of the atoms directly involved in the bonds. The lift of the degeneracy of the sp^2 contribution is a further fingerprint of the polymerisation in Li_4C_{60}. In fact, thanks to the suppression of the broadening effects induced by the anisotropic chemical tensor, each carbon atom gives rise to a nuclear resonance; but the distortions of the fullerene cage produce some differences in the chemical environment, thus introducing a frequency shift in the spectrum. Moreover, focussing on the sp^3 contribution (see inset of fig. 6.7), the appearance of two peaks in this region, whose intensity ratio is approximately 1 : 2, is an unexpected strong confirmation of the particular hybrid bonding scheme of Li_4C_{60}: in fact the sp^3 carbon atoms involved in the single and "double" bonds reside into unequivalent crystallographic positions, whose multiplicities perfectly match the measured intensities. Also the position of the two resonances in the spectrum appear correct: in fact, the weaker peak reflects its

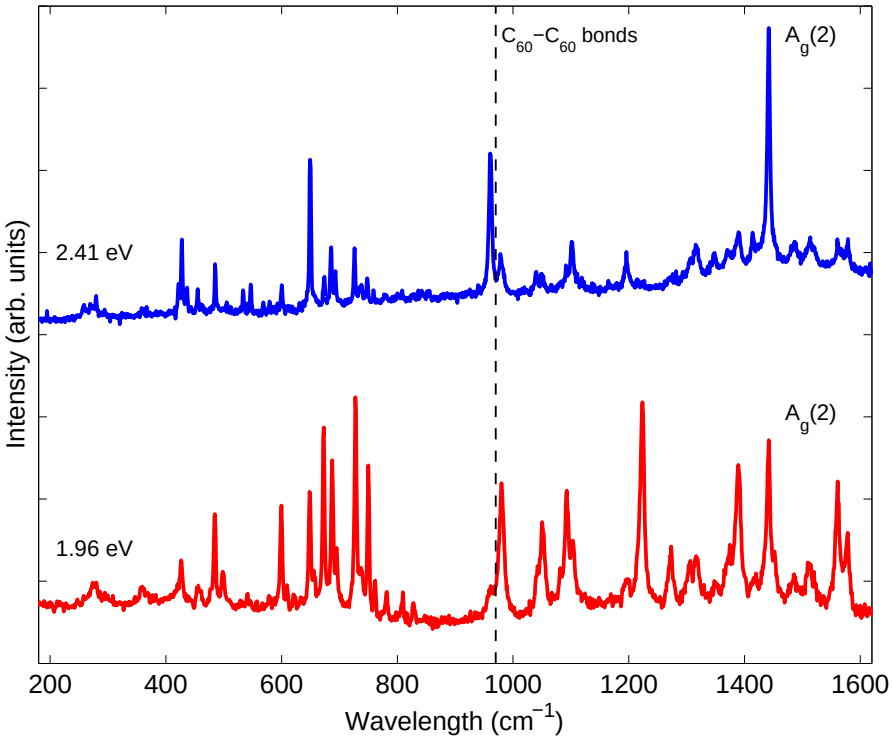

Figure 6.8: Raman spectra of Li_4C_{60} at room temperature for two laser excitation energies: 2.41 eV and 1.96 eV. The two peaks arising from carbon polymerisation are shown in the boxed area.

"single bond" nature, since the more spherical hybridised electronic shell can shield more efficiently the external field.

Both the static and MAS NMR spectra evidenced a negligible effect of the Knight shift tensor, either for its isotropic, or for the anisotropic part. This lead to conclude that as prepared Li_4C_{60} at room temperature presents an insulating behaviour. Further SQUID magnetic measurements performed on this compound indicated a clear diamagnetic response of the polymer, a small contribution from ferromagnetic impurities and a negligible contribution from paramagnetic impurities, as discussed in detail in [12].

6.1.4 Raman spectroscopy on as prepared Li_4C_{60}

Raman spectroscopy was performed on as prepared Li_4C_{60} at room temperature. The work was carried out in collaboration with Dr. Giampiero Ruani and Dr. Dimitri Palles, at the ISNM-CNR institute of Bologna. Two different laser excitation energies were used: 2.41 eV (corresponding to $\lambda = 514.5$ nm) and 1.96 eV ($\lambda = 632.8$ nm).

Both the spectra, shown in fig. 6.8, are characterised by a wealth of narrow peaks (at last 41 discernible bands) which indicate that the probed structure is strongly anisotropic, and confirm the polymerisation of the compound. In fact, on one hand, the lowering of the site symmetry reinforces the effects of the crystal field, which contribute to the lift of the degeneracy of the eight H_g modes; on the other hand, the distortion of the carbon cage, induced by the presence of covalent bonds, changes the selection rules, so that also previously forbidden modes now can acquire Raman activity.

More in detail, it is noticeable the presence of a double peak, in the region $940 - 980$ cm^{-1}; as previously discussed (see chap. 3), these peaks are fingerprints of the presence of the bridging [2+2] cycloaddicted carbon bonds [67], or more generally, of the presence of sp^3 bonds in the structure [65]. In Li_4C_{60} the peaks are positioned respectively at 961 cm^{-1} and 979 cm^{-1}, with $\Delta\omega = 18$ cm^{-1}. Both the positions and the splitting, if compared with tetragonal C_{60} (946 and 974 cm^{-1}, $\Delta\omega = 28$ cm^{-1}), rhombohedral C_{60} (959 and 978 cm^{-1}, $\Delta\omega = 19$ cm^{-1}) and Na_4C_{60} (966 cm^{-1} and 980 cm^{-1}, $\Delta\omega = 14$ cm^{-1}), suggest the hybrid nature of the polymer. Moreover, their relative intensity is strongly dependent on the laser energy, differently from what is found in the Na_4C_{60} case. The feature could be ascribed to the mixed nature of the bonds in the former, which can induce in that case a different distribution of the vibrational energies, depending on the energy of excitation [89].

The narrowing of the lines, detected in both spectra of Li_4C_{60} at room temperature, indicates that the structure is ordered and that the electron-phonon interaction is negligible, as in the case of non metallic systems, thus confirming the insulating nature found with the NMR analysis [89].

Further information follow by the analysis of the position of the $A_g(2)$ mode with respect pristine C_{60}. As already stressed, the downshift of this mode could be related to the charge transfer on the buckyball and also to the cage polymerisation, by the use of some empirical laws (see sec. 3.3). In this case, the $A_g(2)$ parent mode was found at 1442 cm^{-1}. If one evaluates the $A_g(2)$ softening by $6 - 7$ cm^{-1} per electron transferred, and, respectively ~ 2.5 cm^{-1} per single and ~ 5.5 cm^{-1} per "double" C-C bond [11], it results that the total number of electrons on C_{60} is $[1469 - (2 \times 5.5 + 2 \times 2.5) - 1442]/6 \sim 2$, a very low value compatible with a partial charge transfer. On one hand, as already seen in sec. 1.5, this phenomenon was already observed in other lithium doped fullerides [8]. On the other hand, as already discussed in sec. 3.3, the empirical rule involving $A_g(2)$ shift seems to fail in systems both charged and polymerised [65, 11, 91]. Moreover, an incomplete charge transfer in this system is rather questionable, because the large mobility of lithium atoms at room

temperature, as indicated both by diffraction and by ^{7}Li NMR, seem not compatible with the existence of hybrid electronic states between Li and C_{60}.

6.1.5 Discussion

A complete experimental investigation, which involved different and complementary techniques, was performed on the as prepared Li_4C_{60}. The results provide a solid proof that this compound is an unusual polymer, in which both four-membered carbon rings and single C-C bonds coexist and propagate along two orthogonal directions, thus giving rise to a 2D network. The bridging C-C bonds refined distance resulted of 1.75(2) Å, which actually is a somewhat longer than typical covalent single bond, but is still consistent with bonding interactions between neighbouring fullerene units. This feature has never been observed before in any other fullerene based polymer [88] and seems to arise from the particular lithium characteristics.

First of all, the small Li^+ ion dimension (0.6 Å) is a key parameter which allows the buckyballs to get sufficiently close and polymerise with this particular scheme. Here, the smallest Li^+-C distances (2.42(5) Å and 2.54(6) Å for the tetrahedral and the octahedral sites respectively), found in the proposed structure, are larger than the sum of the ionic radius of Li^+ and the Van der Waals radius of C ($\sim$ 1.7 Å), but it would be incompatible with the presence of a bigger alkali cation.

Secondly, the hybrid nature of the polymer seems to be compatible with an effective charge state of the buckyball corresponding to *less than* 4 electrons. In fact, as previously discussed in chap. 1 and in [35], the presence of single C-C bonds in a fullerene polymer can be stabilised only if a high charge transfer on the buckyball is established; on the contrary, cycloaddition reaction does not need any extra charge. Hence, Li_4C_{60} could not have the same structure as the single-bonded polymer Na_4C_{60}, also because of the partial charge transfer from the small alkali atom to the fullerene. However, the last inference is still debated. On one hand, as demonstrated also by other works, Raman investigation seems not to be a suitable technique to investigate the entity of the charge transfer, when the fullerene is both charged and polymerised. On the other hand, both diffraction experiments and NMR spectroscopy clearly show an extreme lithium ion mobility, in contrast with presumed covalent bonding between the alkali and the fullerene.

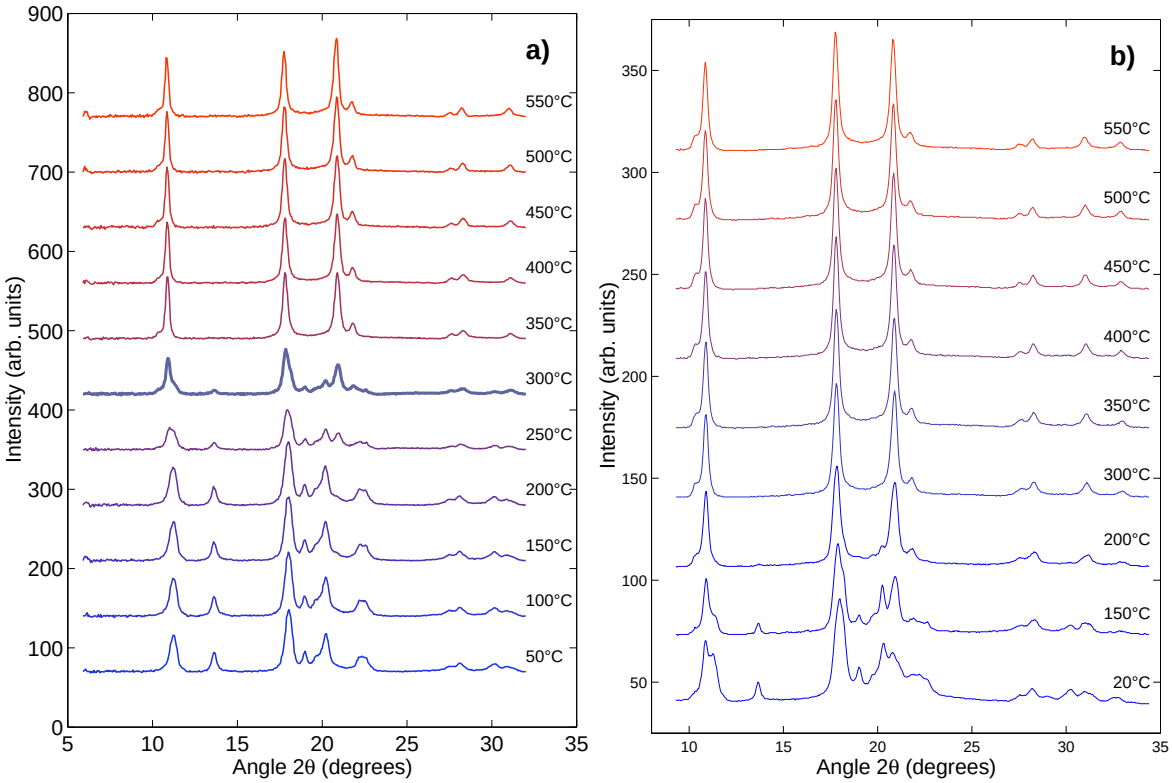

Figure 6.9: a) Thermal evolution on warming of laboratory (CuK_α) diffraction profiles of Li_4C_{60}. The polymer-to-monomer transition is completed at 325° C. b) Structure evolution on cooling. The monomer phase persists down to $\sim$ 180° C, then the compound partially repolymerises into the original phase.

6.2 Thermal treatments on Li_4C_{60}

6.2.1 Structural evolution

A detailed study of the thermal depolymerisation process in Li_4C_{60} was performed by treating the polymeric phase at high temperature. It is well known, in fact, that the strength of the bonds of fullerene polymers is usually sufficiently weak to be broken by the thermal excitations induced by a moderate annealing [42, 36, 5]. In this case, the analysis of the depolymerisation dynamics can give further new insights in the knowledge of the unusual structure of Li_4C_{60}.

Thermal cycles were performed on as prepared Li_4C_{60} and the structure of the sample was monitored by simultaneously collecting x-ray powder diffractograms, both from laboratory (CuK_α) and synchrotron source (ESRF - Grenoble). The compound was sealed in a quartz capillary, and heated respectively by an oven or a gas blower. In

both the cases, the temperature was controlled by a thermocouple, placed very close to the sample, which, after a preliminary calibration, guaranteed a good reproducibility and discrete accuracy (errors within 2%). In fig. 6.9, was shown the powder pattern of Li_4C_{60} obtained by laboratory diffraction at different temperature, corresponding to a complete thermal cycle 50° C - 550° C - 50° C in step of 50° C. On heating, the polymeric phase gradually disappears, as depicted by the progressive lowering of the reflection at $2\theta \sim 13°$, while a more symmetrical phase grows up. The transition is complete at $T \sim 325$°C.

The new phase resembles very well *fcc* pristine C_{60}; indeed, it was easily indexed with a face centered cubic cell, spatial group $\mathbf{F\,m\,\overline{3}\,m}$. Preliminary investigation with Le Bail pattern decomposition, performed on laboratory data, indicated that the refined cell parameter at 350° C results $a = 14.10(1)$ Å, which yields an effective distance among C_{60} centres of ~ 10 Å; this value indicates that the high temperature phase should be in the monomer form [92]. Moreover, the cell parameter turn out to be even smaller than pristine C_{60} (~ 14.17 Å at room temperature), despite the presence of lithium atoms which crowd the lattice interstices; this contraction could be ascribed to the strong electrostatic interaction among the alkali ions and the fullerene units, generated by the charge transfer, which at room temperature yields the polymerisation of the buckyballs.

Subsequent analysis of synchrotron data provided more precise results. The extracted parameters were obtained by refining the powder diffractograms, taken at different temperatures, with a two-phase Le Bail pattern decomposition (both the polymeric monoclinic and the monomer cubic phases); the obtained data allowed a detailed study of the thermal evolution of the polymer. In fig. 6.10 the refined values of the three edges of the polymer cell, and the cubic *fcc* parameter of the monomer, as a function of the temperature, are shown. The temperature range was constrained by the presence of a sufficient amount of the two phases in the sample, necessary to perform the fit. In all the case, the extracted cell parameters turn out to be linearly dependent on the temperature with discrete approximation; hence a linear fit provided the values for the thermal expansions α, which for the generic K parameter is defined as:

$$\alpha_K = \frac{1}{K}\frac{\partial K}{\partial T} \tag{6.1}$$

The values obtained for the three monoclinic and for the cubic parameters are respectively: $\alpha_a = 4.4(2) \cdot 10^{-6}$ K^{-1}, $\alpha_b = 1.7(3) \cdot 10^{-6}$ K^{-1}, $\alpha_c = 2.2(1) \cdot 10^{-5}$ K^{-1} and $\alpha_{a-cub} = 0.9(1) \cdot 10^{-5}$ K^{-1}. The thermal expansion of the polymeric phase results

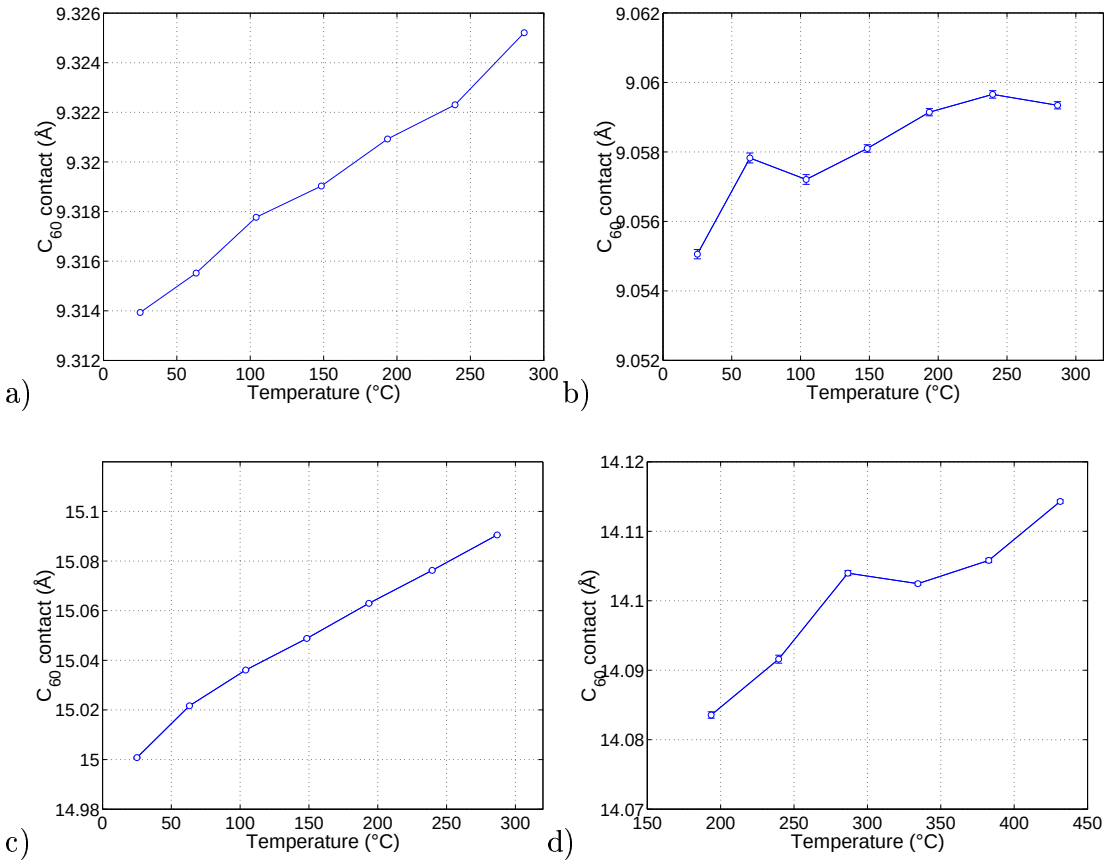

Figure 6.10: Thermal evolution of the cell parameters in the polymeric and monomer phases during the heating treatment. a), b) c) are respectively the trends for *a, b, c* parameters of the monoclinic cell (*a* and *b* are the direction of the two bonds), whereas d) is the evolution of the *fcc* parameter in the monomer phase. Also the extracted values of the thermal expansion are indicated.

strongly anisotropic. Concerning the expansion of the c stacking direction and of the cubic parameters, their values are of the same order of magnitude of other monomeric alkali fullerides [93]. On the contrary, these referred to the a and b parameters of the monoclinic cell, along which polymerisation occurs, are approximately ten times smaller, due to the presence of the covalent bonds which enhance the rigidity of the structure. In particular, the $\alpha_a : \alpha_b$ ratio is approximately $1 : 2$, in very good agreement with the hybrid polymeric model of Li_4C_{60}.

Focussing now on the thermal evolution of a and b parameters of the monoclinic cell, the roughly linear dependences of their value with the temperature suggest that the two types of bond should break simultaneously, despite their different strengths. This fact seems to be confirmed also by the absence of any other phases, during the

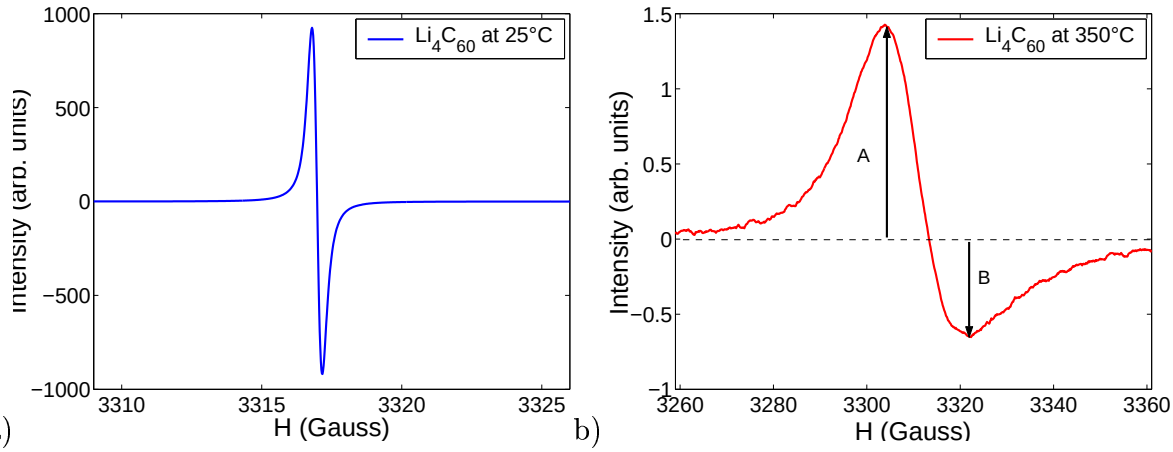

Figure 6.11: A comparison of the ESR line-shapes measured in Li_4C_{60} at a) 22° C and b) 348° C. In the former case the signal is well fitted by a Lorentzian, whereas in the latter by a Dysonian, thus indicating a metal-to-insulator transition in the sample.

depolymerisation process.

On cooling, the monomer phase persists down to $\sim$ 180° C, thus showing a clear hysteresis. Below this temperature, the compound partially repolymerises into the original phase, even though the reflections in the diffraction profile result broader, probably due to the increased number of lattice defects. A minor amount of the sample undergoes an irreversible process, which leads to the formation of a new structural phase, not yet investigated.

6.2.2 Electronic behaviour

The electronic properties of Li_4C_{60} were probed during a polymer-to-monomer transition by Electron Spin Resonance (ESR) in (x band, 9.6 GHz) in CW configuration. The measurements were performed at the Jozef Stefan institute of Ljubljana, with the collaboration of Dr. Denis Arčon, and are treated in more detail in [12].

ESR is a powerful instrument to investigate the electronic and magnetic state in a paramagnetic compound which presents uncoupled electrons. The spectrum obtained at 25° C on the as prepared Li_4C_{60} consists of an unexpected very narrow peak, well fitted by a Lorentzian line-shape (ΔH_{pp} = 0.27(3) G), as shown in fig. 6.11a; the presence of this resonance could seem to be in contrast with the diamagnetic behaviour of the compound, as detected by SQUID magnetometry measurements. Actually, it probably arises from the presence of few defects (e.g. breaking of polymeric bonds), which are present in the polymeric network already at room temperature, as discussed

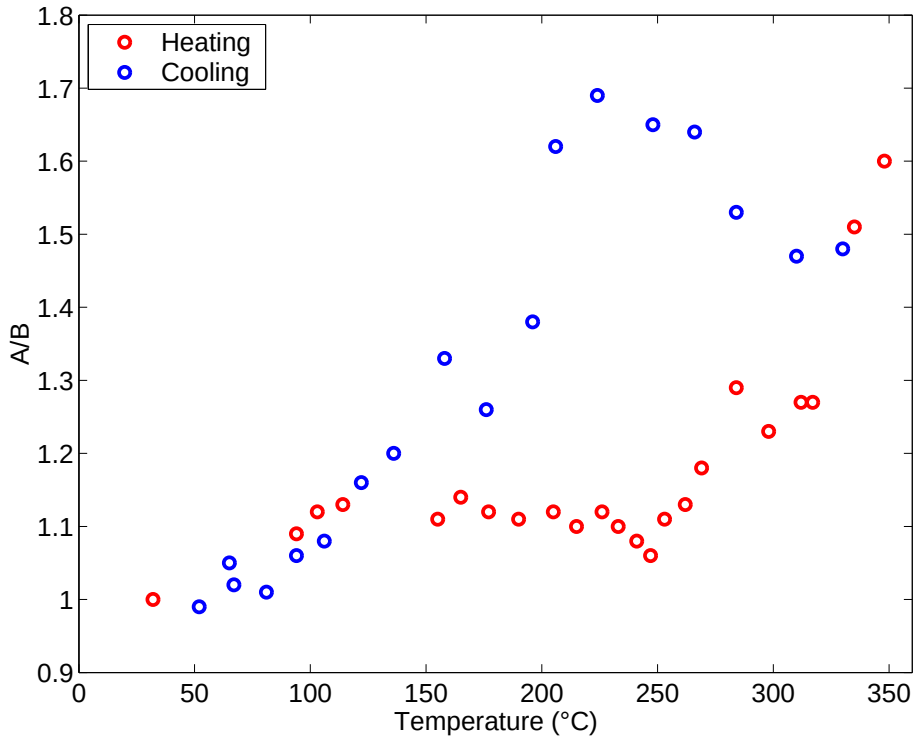

Figure 6.12: The temperature dependence of the line-shape asymmetry ratio A/B for heating (*red* circles) and for cooling (*blue* circles).

in more detail in [12].

When the temperature of the sample increases, also the intensity of the ESR signal enhances, but, surprisingly, this is also accompanied by the growth of an anisotropic contribution in the line-shape. This effect becomes extremely marked at temperatures above 250° C, in the proximity of the polymer-to-monomer transition of the compound. The asymmetry of the signal can be roughly measured as the ratio A/B, where A and B are respectively the height of the positive and negative peaks. In fig. 6.12, the temperature dependence of the asymmetry ratio is plotted for a complete thermal cycle which leads to the depolymerisation of the sample. At room temperature $A/B = 1$ and, after a first increase to 1.10(4) at 100° C, it remains constant up to 250° C. Above this threshold, it start to increase dramatically and reaches $A/B = 1.6(1)$ for T$\sim$ 350° C. For this temperature, the measured line-shape is well fitted by a *Dysonian* [94], which is a typical feature of metals (see fig. 6.11b). Furthermore, if the compound is cooled, the asymmetry persists down to $\sim$ 200° C, thus showing a clear hysteresis, in analogy with the structural behaviour. Below this temperature, the original value $A/B = 1$ is progressively recovered, together with the polymeric state of the sample.

These data provide a strong proof that the metallicity is a feature of the monomer Li_4C_{60} and induced to a more detailed investigation of this phase.

6.3 Monomer phase of Li_4C_{60}

6.3.1 Structural analysis

Monomer phase of Li_4C_{60} underwent an accurate structural analysis, starting from synchrotron x-ray diffraction data. The diffractogram was collected at ESRF - ID31 at 500°, $\lambda = 0.85055$ Å. The compound was sealed in a 0.5 mm quartz capillary, and heated with an air blower. The measurement was performed after having guaranteed the correct thermalisation of the sample; no particular care was used to define the warming ramp, because it was found not to affect the depolymerisation process. Due to the plastic state of the high temperature monomer phase, the structural investigation was performed with the FULLPROF suite (see par. 4.3.2).

Powder pattern indexing and powder pattern decomposition

First, analysis of the cell symmetry yielded surprisingly an hexagonal cell, rather than cubic, as found during the preliminary study from laboratory x-ray diffraction data; nevertheless, a second more accurate investigation pointed out that the cell is indeed cubic, but the structure resulted highly faulted. This means that the ideal stacking sequence ABCABCABC... of the (1 1 1) crystal planes of the *fcc* lattice is modified as ABC**BC**ABC... (stacking fault) or ABCABC**BA**CBA... (twin fault). This effect, which is present also in pristine C_{60} [95], results particularly evident for monomer Li_4C_{60}, and introduces several distortions in the measured powder pattern. For example, the shoulder at the left of the first main (1 1 1) reflection resulted very intense and in principle was erroneously confused with a real peak; however, the typical asymmetric profile and the impossibility of indexing it, indicated that it actually results from a stacking fault contribution, hence it was excluded by the fit. Other more subtle distortions emerged during the powder pattern decomposition analysis, by taking into account only the *fcc* phase: in particular some problems were encountered to fit both the (2 2 0) and the (2 2 2) peak. These features represented serious problems during the Le Bail analysis, and were overcome only by accepting the presence of a further minority hexagonal phase; actually it contributes only as almost amorphous background, and represents an almost negligible part of the sample. It was not possible to index it,

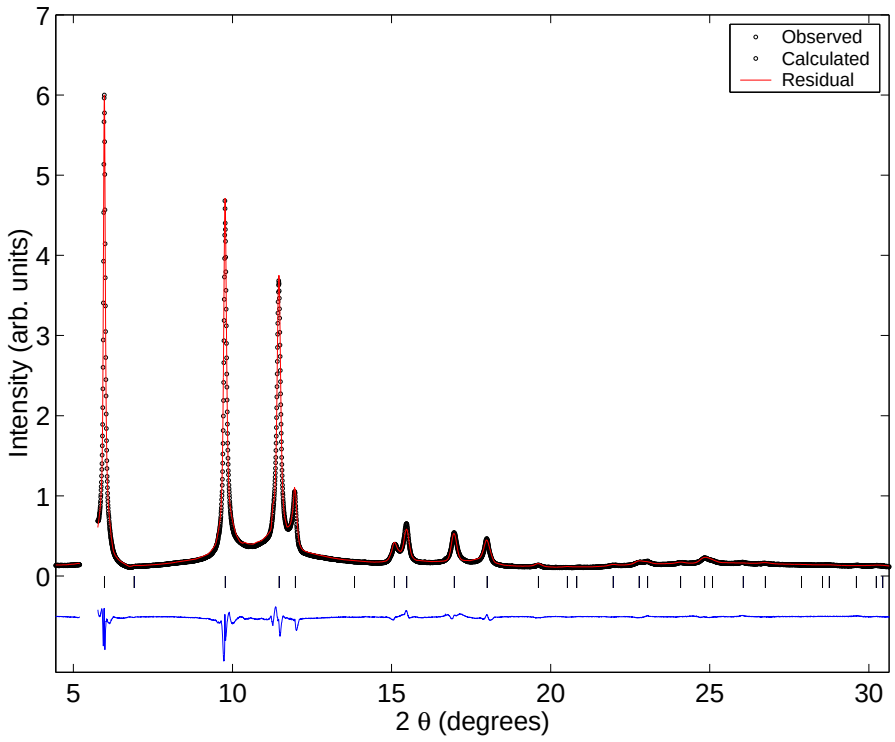

Figure 6.13: Measured (o) and calculated (solid line) powder diffraction pattern of Li_4C_{60} at 500° C (a = 14.1228(1) Å). The lower solid line in *blue* is the difference profile, whereas the ticks mark the reflection positions.

but it was simply incorporated into the background signal. The refined cell parameters obtained from this analysis are for the main cubic phase: spatial group $\mathbf{F\,m\,\overline{3}\,m}$, $a = 14.12454(9)$ Å, $R_{wp} = 4.90\%$.

Rietveld refinement

The starting model for the Rietveld refinement of monomeric Li_4C_{60} is analogous to K_3C_{60}, in which rotating fullerenes are packed in a *fcc* structure, and the octahedral and tetrahedral voids are filled by alkali ions. But in this case, thanks to the smaller lithium dimensions, more than one ion can occupy the interstices.

In the structure buckyballs undergo a rotational motion, as observed in plastic crystals. C_{60} electronic distribution was approximated with a multipole expansion of symmetry adapted spherical harmonics (SASH); this method allowed to obtain a more precise description of the molecular shape, with respect the rough spherical shell approximation. As discussed in detail in Appendix A, the coefficients of the spherical harmonics, which determine the electronic density in a rotating molecule, are defined

by several selection rules; they depend on both the site and the static molecular symmetry. For an icosahedral molecule, like C_{60}, which is placed in a cubic site (symmetry **m3m**), the electronic density can be expressed as a series expansion of cubic harmonics, which are linear combination of spherical harmonics satisfying the cubic symmetry [96]. FULLPROF suite allows to expand on the SASH the molecular form factor of the diffracting molecules. In detail, the program separates the rotating molecule in N shells, each in general corresponding to an atom. Hence, the molecular form factor $f(\mathbf{Q})$ can be expressed in spherical coordinates as [97]:

$$f(\mathbf{Q}) = 4\pi \sum_{slj} c_{lj}^{s} i^{l} j_l(Qr_s) b_s K_{lj}(\theta, \phi) \tag{6.2}$$

where the index s runs from 1 to N and labels the s-th spherical shell; $j_l(x)$ is the spherical Bessel function of order l. $K_{lj}(\theta, \phi)$ represent the cubic harmonics of order l and index j, as defined in [51]; b_s is the x-ray scattering factor of the atom. The coefficients c_{lj}^{s} are "weight" factors of the individual terms of the series, and are the fitted parameters during the Rietveld refinement.

Due to its conformation, C_{60} was approximated as one shell ($s = 1$), containing 60 carbon atoms. The expansion was limited at the tenth order, which is a reasonable compromise between the resolution available by the data and a exhaustive description of the electronic density [10, 93]; it means to consider the cubic harmonics of indices $i, j = (0, 1), (6, 1), (10, 1)$ (see Appendix A). Also the radius of the shell was refined. The refined coefficients c_{lj} are shown in tab. 6.5 and are discussed below.

Concerning lithium atoms, several positions were checked during the refinement, in order to reduce the value of the agreement factors; the best agreement was reached with the alkali atom is in the octahedral site with full occupation, and another disordered in a off-centering position of the tetrahedral site; this last position was obtained from a transformation of the polymeric pseudo-tetragonal position. The best fit is represented in fig. 6.14. The refined cell parameter, the shell and lithium positions, the SASH coefficients and the agreement factors are summarised in tab. 6.5. In particular, the agreement factors were referred only to the pattern sectors in correspondence of the Bragg reflections, because of the background modifications discussed above. The satisfactory results obtained definitely confirm that the structure of Li_4C_{60} is cubic.

In an attempt to give physical insight to the refined parameters, a part of the work was dedicated to visualise the refined electronic distribution on the shell surface. The output of FULLPROF is the molecular form factor, expressed in spherical coordinates in the reciprocal space (see eq. 6.2); in order to transpose the results in the direct lattice

Parameters	**Li_4C_{60}**	**$Li_{12}C_{60}$ [10]**	**Li_2CsC_{60} [93]**
Temp. (°C)	500	277	18
a (Å)	14.1228(1)	14.09(1)	14.004(1)
Radius (Å^2)	3.5218(9)	3.559(2)	3.552(5)
$c_{0\,1}$	1	1	1
$c_{6\,1}$	0.058(2)	0.038(4)	0.048(10)
$c_{10\,1}$	-0.101(11)	0.226(27)	-0.26(3)
R_{wp}, R_{exp} (%)	4.08, 0.96*	10.9, 2.4	9.8, 5.9

	x	**y**	**z**	**Pos.**	B_{iso}(Å^2)	**Frac.**
C shell	0	0	0	*4a*	1.8(2)	1
Li1	0.5	0	0	*4b*	15(6)	1
Li2	0.3130(7)	0.3130(7)	0.3130(7)	*32f*	15(6)	0.088(1)

Table 6.5: Refined structural parameters for monomer Li_4C_{60} derived from the Rietveld refinement (space group $\mathbf{F\,m\,\overline{3}\,m}$) of the synchrotron x-ray diffraction data taken at T=500° C (ESRF-ID31). As a comparison, also the extracted values of the coefficients for $Li_{12}C_{60}$ at 277° C [10] and for Li_2CsC_{60} at 25° C [93] were shown. * The weighted profile and expected factors are referred only to the pattern sectors in correspondence of the Bragg reflections.

and allow their visualisation, it was developed a program, in MATLAB environment, capable of providing a Cartesian mapping and the three-dimensional Fourier transform in the real space of these data, by the use of FFT algorithm. The result, in fig. 6.14, clearly shows the presence of an interaction between alkali ions placed in the tetrahedral voids and C_{60}, which suggests a concentration of the electronic density along the [1 1 1] directions. The entity of this contribution results from the negative value of the term $c_{10\,1}$ in the serial expansion , and is proportional to its absolute value [10]. It is useful to compare the value of $c_{10\,1}$ of monomeric Li_4C_{60} with those obtained for monomer $Li_{12}C_{60}$ and Li_2CsC_{60}, which underwent an analogous study [10, 93] (see tab. 6.5). In $Li_{12}C_{60}$ at high temperature (> 277° C), alkali atoms are placed into the octahedral voids, to form a cluster; hence they do not perturb the electronic density of C_{60} along the [1 1 1] directions as indicated by the $c_{10\,1}$ coefficient, which turn out to be positive. On the contrary, in the analysis of Li_2CsC_{60}, performed at room temperature, $c_{10\,1}$ was refined with a negative value, thus indicating a not negligible Li^+-C interaction for the lithium atoms located in the tetrahedral sites. This fact provides an explanation to the partial charge transfer from the alkali atom to the fullerene, which was found in this compound [8]. In monomer Li_4C_{60} the value of this term results negative, but smaller than in Li_2CsC_{60}, and suggests that the electronic transfer in this case should be on

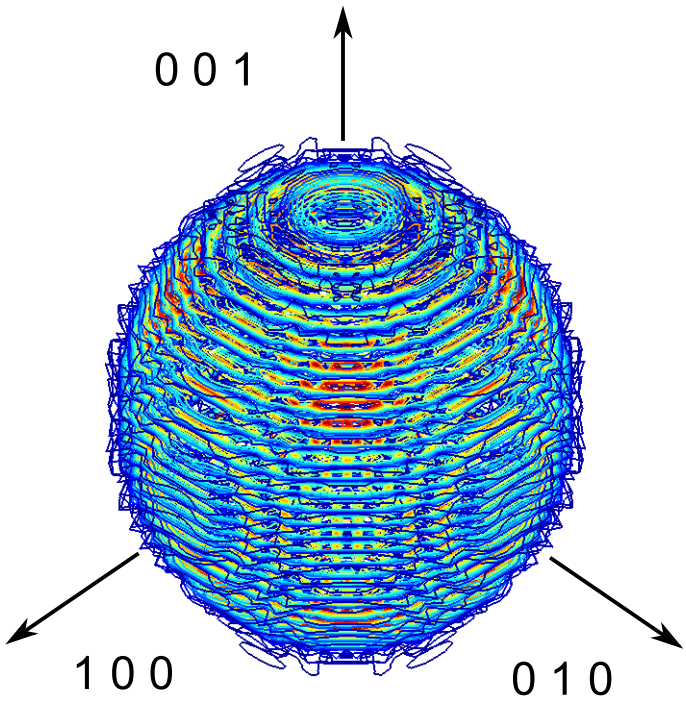

Figure 6.14: Orientation distribution functions for C_{60} ions in Li_4C_{60} at 500° C, viewed down the [1 1 1] direction. *Red* colour indicates the zones with the maximum electronic density.

the contrary almost complete.

6.3.2 Raman investigation at high temperature

Li_4C_{60} in monomer phase underwent accurate Raman investigation. The measures were performed in collaboration with Dr. Giampiero Ruani at the ISMN/CNR, Bologna. The spectra were collected in backscattering geometry and the excitation source consistes in a He-Ne laser whose wavelength was fixed at 632.8 nm (1.96 eV). The light was focused on the sample with a microscope lens of magnification ×50; care was spent to avoid photo-damage of the sample, and the laser power density was kept below 200 W/cm^2.

The heating apparatus consisted in a home made temperature controlled plate, on which the samples,contained in 0.5 mm quartz capillaries, were fixed with a glue capable to assure a good thermal contact. This system was able to easily reach the temperature of 400° C, with an accuracy better than 2° C.

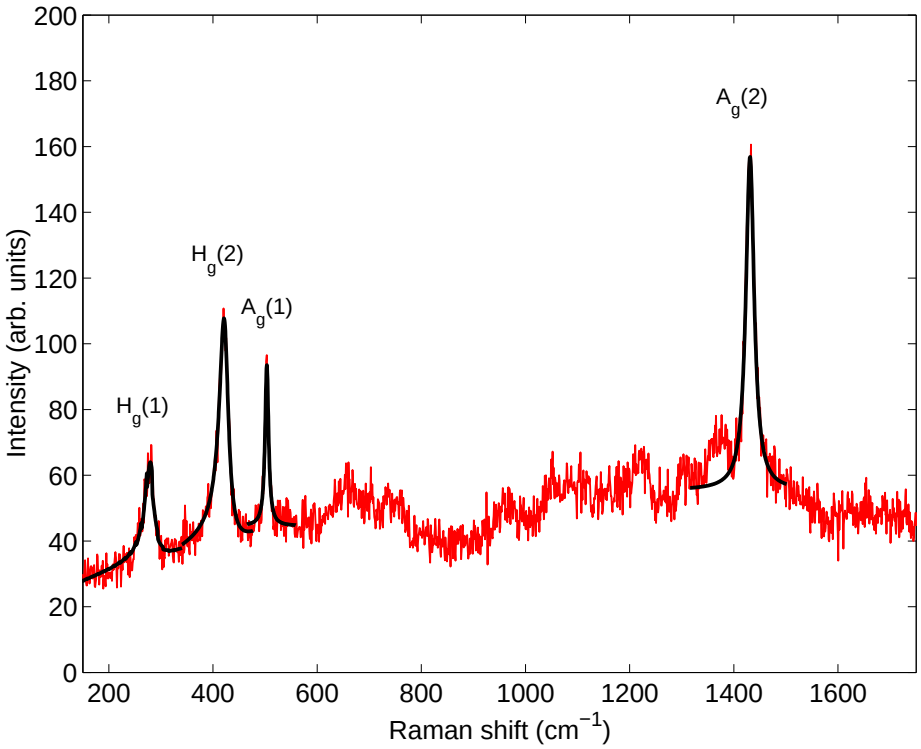

Figure 6.15: Raman spectrum of monomer phase of Li_4C_{60} taken at 375° C with laser energy of 1.96 eV (He-Ne). The H_g peaks (on the left) appear broadened and asymmetric, thus confirming the metallic behaviour of the compound.

The Raman spectrum of Li_4C_{60} at 375° C, a temperature corresponding to the monomer plastic state, is shown in fig. 6.15. This indeed results very different from that collected on the as prepared sample at room temperature; in fact, despite the presence of a large number of narrow lines characterising the polymeric phase, in the monomer spectrum only four resonances are detectable at about 280, 420, 500 and 1430 cm^{-1}, respectively referred to $H_g(1)$, $H_g(2)$, $A_g(1)$ and $A_g(2)$ modes. Of these, the two Hg modes present asymmetric shape, whereas the Ag result symmetric. The absence in the spectrum of several Hg modes and their asymmetrical broadening are features observed also for A_3C_{60}, which shows a Raman spectrum very similar to Li_4C_{60} [64, 63], and are strong confirmations of the metallic nature of the compound (see chap. 3.3.2).

Then the analysis was focussed on the energy shift of the well detectable $A_g(2)$ of Li_4C_{60} with respect pristine C_{60}, which is connected to the effective charge transfer on the buckyballs. In order to separate this contribution from that due to the thermal softening of the Raman modes, simultaneous measurements were taken at the same temperature also on pristine C_{60}; a measure of the undoped system provided a reference

either for the mode shifts or for the line broadening. The pristine C_{60} spectrum (not shown here) presented only three detectable resonances, with Lorentzian line-shape: $H_g(1)$ at 275.9(1) cm^{-1} ($\Gamma_{Hg1} = 5.8(5)$ cm^{-1}), $A_g(1)$ at 497.6(1) cm^{-1} ($\Gamma_{Ag1} = 3.5(3)$ cm^{-1}) and $A_g(2)$ at 1458.8(2) cm^{-1} ($\Gamma_{Ag2} = 5.6(7)$ cm^{-1}). Likewise, the $A_g(2)$ peak in Li_4C_{60} can be fitted with a Lorentzian profile, and is placed at 1431.1(2) cm^{-1} ($\Gamma_{Ag2} = 19.2(5)$ cm^{-1}), thus showing an effective energy shift of 27.8 cm^{-1}. This value is totally compatible with a full charge transfer of four electrons per C_{60} unit (6.9 cm^{-1} per electron). This is a very important result, which allows to compare monomer Li_4C_{60} to the other A_4C_{60} systems, and will be discussed in detail later. Further insights arises from the detailed analysis of the line shapes in the two H_g modes. In analogy to [63], their asymmetric broadening was interpreted as the effect of a Breit-Wigner-Fano (BWF) resonance (see par. 3.3.2), which indicates an interaction between the phonon modes with free electrons, as expected in a metallic phase. The fitting of the intensities of the peaks with a BWF-like curve:

$$I = I_0 \left|q + \epsilon\right|^2 / \left(1 + \epsilon^2\right) \tag{6.3}$$

$$\epsilon = (\omega - \omega_0)/(\Gamma/2)$$

yields the following data: $H_g(1)$ at 279.5(7) cm^{-1} ($\Gamma = 21(1)$ cm^{-1}, $q = -8(2)$), $H_g(2)$ at 422.5(4) cm^{-1} ($\Gamma = 21.0(6)$ cm^{-1}, $q = -7.5(1.1)$). From the knowledge of the resonance frequency ω_i and the line-width broadening of the i-th mode, it is possible to evaluate the corresponding electron-phonon coupling constant λ_i, by the eq. 3.14. Assuming a reasonable value for $N(\epsilon_f) \sim 13$ state/eV molecule [98], it resulted $\lambda_{Hg1} = 0.2$ and $\lambda_{Hg2} = 0.08$, and a negligible contribution for the A_g modes; these values are of the same order of magnitude of those obtained for other fullerides: $\lambda_{Hg2} = 0.6$ for K_3C_{60}, $\lambda_{Hg2} = 0.5$ for Rb_3C_{60} [63], $\lambda_{Hg1} = 0.3$ for Na_4C_{60} [11]. Nevertheless, for Li_4C_{60} and Na_4C_{60} the main electron-phonon coupling contribution arises from $H_g(1)$, whereas in A_3C_{60} the larger part is due to the $H_g(2)$ mode. The high electron-phonon coupling in monomer Li_4C_{60} suggests that, if the monomer metallic state could be quenched down to low temperatures, a superconducting phase could be observed at relatively high transition temperature.

6.3.3 Discussion

Sample	Cell	C_{60} dist. (Å)	Temp. (°C)	Metal. char.	Ref.
Li_4C_{60}	*fcc*	9.974(1)	380	Yes	This work
Na_4C_{60} (*)	*bct*	9.80	277	Yes	[42]
K_4C_{60}	*bct*	9.98	25	No	[99]
Rb_4C_{60}	*bct*	10.10	25	No (Yes HP)	[99, 100, 30]
Cs_4C_{60}	*bct*	10.27	25	No	[79]
$Li_2Na_2C_{60}$ (**)	*hcp*	10.03(1)	300	No	This work

Table 6.6: The main physical properties of A_4C_{60} compounds. * Monomer Na_4C_{60} presents also a minority cubic *fcc* phase, as reported in [42]. ** Monomer phase of $Li_2Na_2C_{60}$ is treated in detail later.

The study of the polymer-to-monomer transition in Li_4C_{60} provided unexpectedly important results on the electronic properties of this compound: in fact, the monomer phase turn out to be a genuine metal both from ESR and Raman data. Preliminary ^{13}C NMR spectroscopy performed on monomer Li_4C_{60} yielded a further confirmation, as discussed in [12]. This feature assumed even more importance, after that Raman spectroscopy clearly indicated the presence of a full charge transfer of four electrons to C_{60}. This fact was supported also by a detailed structural investigation, which also evidenced that in Li_4C_{60} fullerenes are close packed in a cubic lattice.

As far as the class of the A_4C_{60} fullerides is concerned, Li_4C_{60} features are then very atypical and can potentially shed more light on the strongly correlated behaviour of these compounds. As already seen, in these systems, the presence of a highly correlated electronic state and (dynamical) Jahn Teller distortions were indicated as the origin of the unusual diamagnetic insulating state (see chap. 1.3) [25, 26]. In this framework, the metallic behaviour of the monomer Na_4C_{60} could be explained, if the influence of the smaller interfullerene distance is taken into account, as an important parameter capable to shift the U/W ratio below the critical value. Confirms of this phenomenon arose also from the metal-to-insulator transition induced on Rb_4C_{60}, simply by applying a moderate external pressure on the compound. In monomeric Li_4C_{60}, this simple argument seems not to be sufficient to explain the metallic behaviour, because, as shown in tab. 6.6, C_{60}-C_{60} distance is practically the same as K_4C_{60}. Probably, in our case, it is the higher symmetric *fcc* lattice of Li_4C_{60}, with respect the *bct* arrangement observed in all the other known A_4C_{60} compounds, which plays a fundamental role to enhance the value of $(U/W)_C$, thus favouring the electron hopping between neighbours buckyballs [25]. This effect seems to overcome the Jahn Teller effect, which in these

systems should favour an insulating non magnetic state. In the tab. 6.6 the main physical properties of the A_4C_{60} systems are summarised.

6.4 Ammoniated phases of Li_xC_{60}

The metal-to-insulator transition observed in Li_4C_{60} is a clear demonstration of the fact that lithium fullerides are highly correlated systems; a small variation in the structural parameters of those compounds can indeed yield new interesting phases with a wealth of physical properties.

As shown in sec. 1.6, intercalation of molecular ammonia in fullerene based systems is a powerful method for chemically controlling the structural properties of the host lattice. The introduction of the NH_3 spacer into the Li_xC_{60} is expected to prevent the polymerisation already at room temperature, thus giving rise to new phases in which alkali electrons are no more involved into the formation of covalent bonds, but can fill the LUMO band of the fulleride.

The ammoniated compound $(NH_3)_yLi_xC_{60}$ $(3 \leq x \leq 6)$ were prepared in two different ways, as previously described in chap. 5: by alkali solution in liquid ammonia at low temperatures and by direct exposure of Li_xC_{60} samples to ammonia vapours. In particular, in this second case, the polymeric phase of Li_4C_{60} was first heated at $\sim 350°$ C, thus allowing the polymer-to-monomer transition. Then, the temperature was lowered at 190° C, where the compound preserve the monomeric character, but the reaction can be conducted more safely. The monomer state of the compound guaranteed a better uptake of ammonia and allowed to obtain a metastable phase with approximately $10 - 12$ molecules per C_{60} units, depending on the lithium stoichiometry considered. Subsequent pumping of the sample at controlled temperature for several minutes permitted to vary the amount of ammonia and yielded a stable phase, discussed below, which was obtained alternatively also with the first "conventional " preparation method.

Structural properties

All the per-ammoniated samples $(NH_3)_yLi_xC_{60}$ discussed before, with $3 \leq x \leq 6$, underwent a preliminary structural characterisation with laboratory x-ray diffraction (CuK_α). Their behaviour turn out to be substantially similar, hence the following discussion is focussed on the stoichiometry $x = 4$. In fig. 6.16 was shown the powder diffraction patterns of $(NH_3)_yLi_4C_{60}$ collected at room temperature, after having

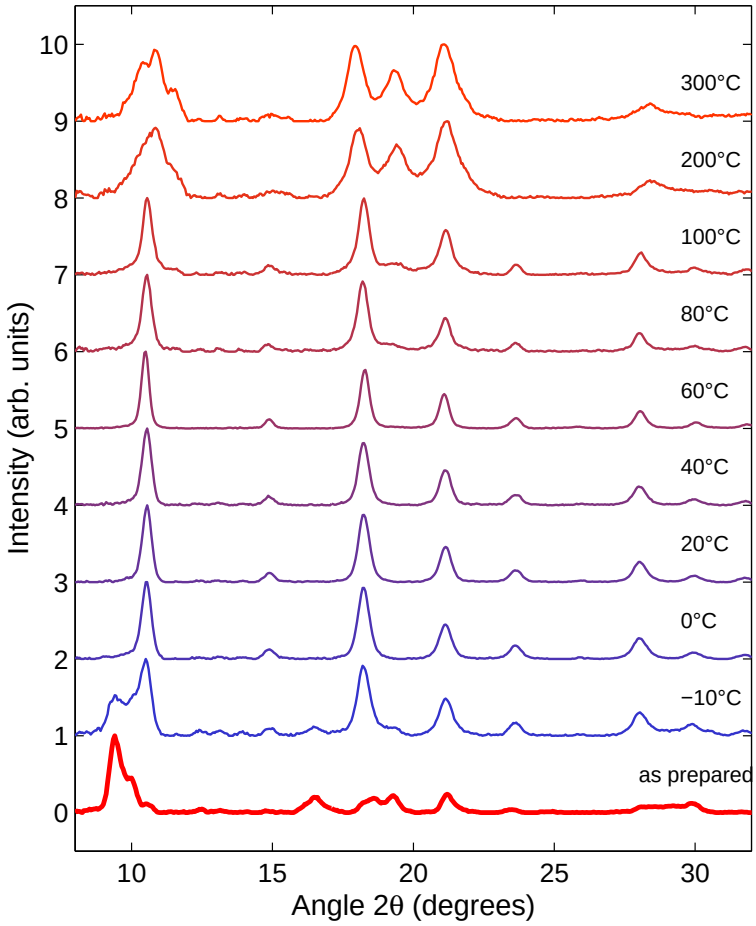

Figure 6.16: Structural evolution of $(NH_3)_yLi_4C_{60}$, by pumping the as-prepared perammoniated phase (in *red* at the bottom of the figure) at different temperatures. The stable *bcc* phase decomposes for temperatures higher than 100° C.

pumped the as prepared sample at different temperatures for 1/2 hour. The starting metastable compound presents a diffraction profile with a large background fraction; the low number of peaks which can be separated is not sufficient to perform a crystallographic analysis, but probably more than one phase is present. Successive pumping treatment provides the gradual transformation to a new phase, which is almost complete for tratments at T$>$ 0° C. This phase is totally different both from those of polymeric and monomer Li_4C_{60}, and is compatible with $\sim$ 6 ammonia molecules per C_{60} unit; it was easily indexed with a *bcc* lattice, with parameter $a = 11.92(1)$ Å. The same compound was recently observed also by Durand and co-workers [101, 102]. Furthermore, the phase is rather stable, and progressively deteriorates after pumping treatments up to $90 - 100°$ C. Above these temperatures, the disorder in the structure

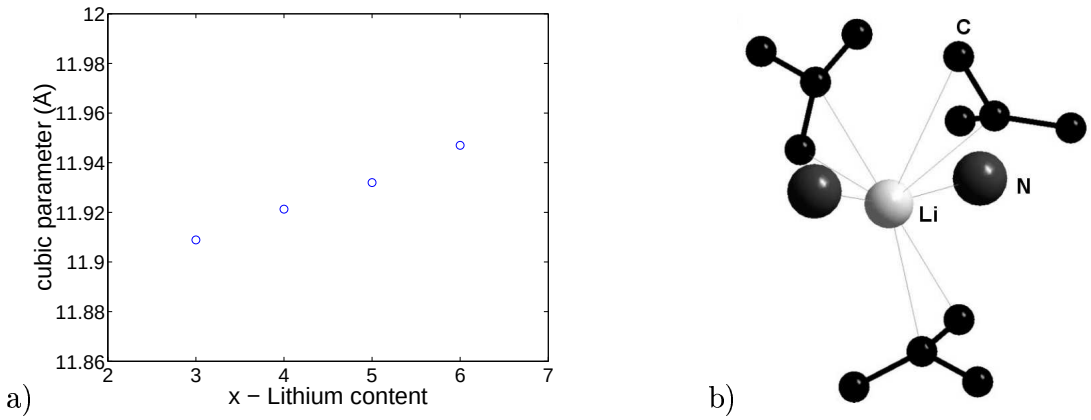

Figure 6.17: a) The dependence of cubic parameter of $(NH_3)_6Li_xC_{60}$ cell in function of the Li stoichiometry. b) The coordination of ammonia molecules and fullerenes with respect lithium atoms in the structure proposed by Durand et al. [102].

increases, as indicated by the broadening of the reflections and the increase in the background signal; new peaks appear and some of them could be referred to pristine C_{60}, which probably segregates. No other pure phases were observed.

Analogous *bcc* phase characterises all the considered lithium stoichiometries, from $x = 3$ to $x = 6$, with negligible dependence of the lattice parameter from lithium content x (see fig. 6.17a). Synchrotron radiation diffraction on $(NH_3)_6Li_4C_{60}$ obtained after pumping the perammoniated phase at 60° C for 1/2 hour was performed at ESRF-ID31 (Grenoble) and provided the necessary resolution for a deeper structural investigation. The diffraction data, taken at room temperature with $\lambda = 0.85055$ Å, are in good agreement with the structure proposed by Durand [102]; in this scheme, lithium cations are linearly coordinated with two ammonia molecules, arranged at the distance of ~ 2.33 Å, and are placed in a trigonal bipyramidal environment, in which the equatorial planes are triangle of C_{60}^{3-} anions, as shown in fig. 6.17b. During this analysis, NH_3 units were approximated to Ne atoms, because of the impossibility of localizing hydrogen atoms with x-rays. Rietveld refinement performed on the crystallographic data (see fig. 6.18) allowed to determine both the lithium and ammonia fractional occupancy in the sample; the results are in good agreement and lead to the nominal stoichiometry $(NH_3)_{5.40(1)}Li_{3.58(7)}C_{60}$. The high value of the thermal factor for Ne can be rationalised if the static disorder of the ammonia molecule in the structure is taken into account. In tab. 6.7 the refined parameters obtained for this sample were summarised.

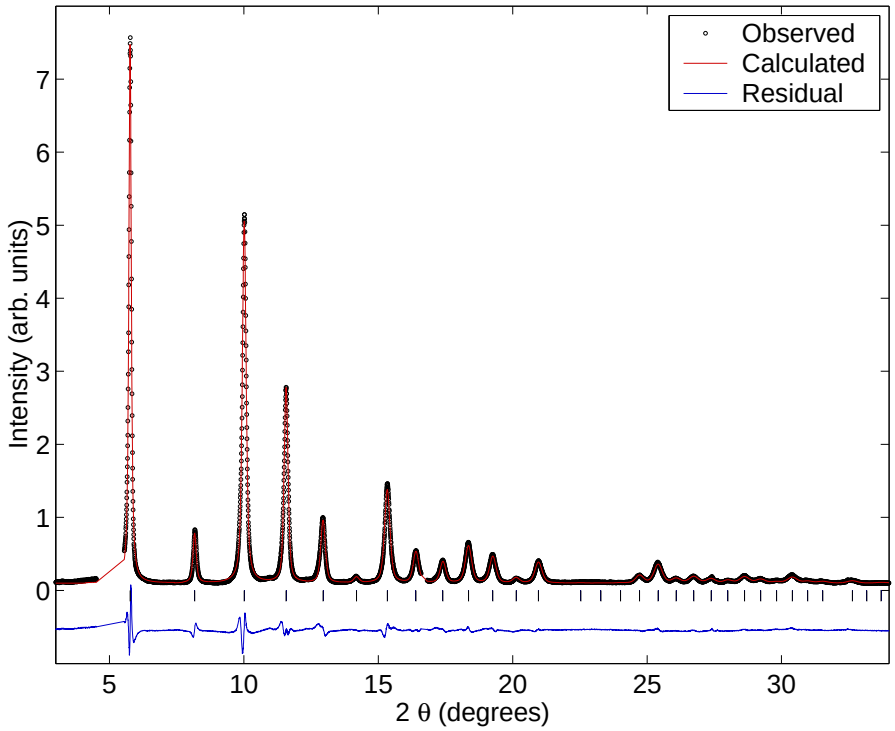

Figure 6.18: Measured (o) and calculated (solid line) powder diffraction pattern of $(NH_3)_6Li_4C_{60}$ at 25° C (spatial group $\mathbf{Im\overline{3}}$, $a = 11.9213(2)$ Å, agreement factors $R_{wp} = 7.71\%$, $R_{F2} = 7.09\%$). The lower solid line in *blue* is the difference profile, whereas the ticks mark the reflection positions.

Magnetic and electronic properties

The *bcc* structure of ammoniated lithium fullerides display a noticeable C_{60}-C_{60} distance of ~ 10.32 Å, a value which is totally incompatible with fullerene polymerisation. Hence the electrons donated by the alkali fill the molecular frontier orbital t_{1u}, which should conserve the triple degeneracy, thanks to the cubic symmetry of the lattice; in this context hence it is of paramount importance to investigate the electronic properties of these correlated systems, in order to understand if the competition between the energy gained by delocalising the charges, given by the narrow bandwidth W, and the opposite inter-electron repulsion U gives rise to a metallic state rather than a metal to insulator transition. Magnetisation measurements were performed on the cubic samples $(NH_3)_6Li_xC_{60}$, both for $x = 3$ and $x = 4$, with a SQUID magnetometer [12]; in all the cases, the measured magnetisation turn out to be strongly dependent on the temperature, as expected in a system in which the t_{1u} electrons are localised. In fig. 6.19, the magnetic molar susceptibility χ (emu/mol) versus the temperature of

a (Å)	11.9213(2)
R_{wp}, R_{F2}	7.71, 7.09

	x	**y**	**z**	**U_{iso}(Å^2)**	**Pos.**	**Frac.**
C1	0.1206	0.0976	0.2554	1.63(2)	*48h*	1
C2	0.0613	0.1935	0.2182	1.63(2)	*48h*	1
C3	0.0586	0	0.2924	1.63(2)	*48h*	1
Ne	0.516	0.274	0	10.72(8)	*24g*	0.450(1)
Li	0.378	0.413	0	5.69(7)	*24g*	0.298(6)

Table 6.7: Refined structural parameters of $(NH_3)_6Li_4C_{60}$ starting from Rietveld analysis of Synchrotron data (ESRF-ID31, Grenoble). The atomic positions were assumed as in [102].

$(NH_3)_6Li_4C_{60}$ was shown. The curve is well fitted with a Curie-Weiss function:

$$\chi = \frac{C}{(T-\theta)} + \chi_0 \tag{6.4}$$

where χ is the molar susceptibility, C is the Curie constant, θ the Neel temperature, T the temperature in Kelvin and χ_0 the contribution from temperature independent susceptibilities (diamagnetism, Van Vleck paramagnetism). The range considered for the fit was $2-135$ K, due to the presence of an anomaly at ~ 150 K, which is commonly attributed to the freezing of the rotational dynamics in ammonia molecules. The Curie-Weiss behaviour of χ indicates the presence of an antiferromagnetic coupling between the localised spins, even if no sign of effective antiferromagnetic order was observed at the corresponding θ. Similar features were observed also in case of $x = 3$. This fact is in contrast with previously reported results [101, 102], which on the contrary observed an anomaly in the χ dependence, both for $x = 3$ and $x = 5$; this effect was interpreted as an antiferromagnetic phase transition of the sample. Actually similar anomalies were observed also in our data, but were attributed to a problem in sample thermalisation; further μSR measurements on these compounds definitively confirmed the absence of long range magnetic order [103, 12].

From the knowledge of C is possible to extract the effective molecular magnetic moment p, in units of Bohr magnetons μ_B:

$$C = \frac{N_a p^2 \mu_B^2}{3k_B} = n \cdot \frac{N_a g^2 j(j+1)\mu_B^2}{3k_B} \tag{6.5}$$

where N_a is the Avogadro's number, k_B the Boltzmann's constant, g the giromagnetic

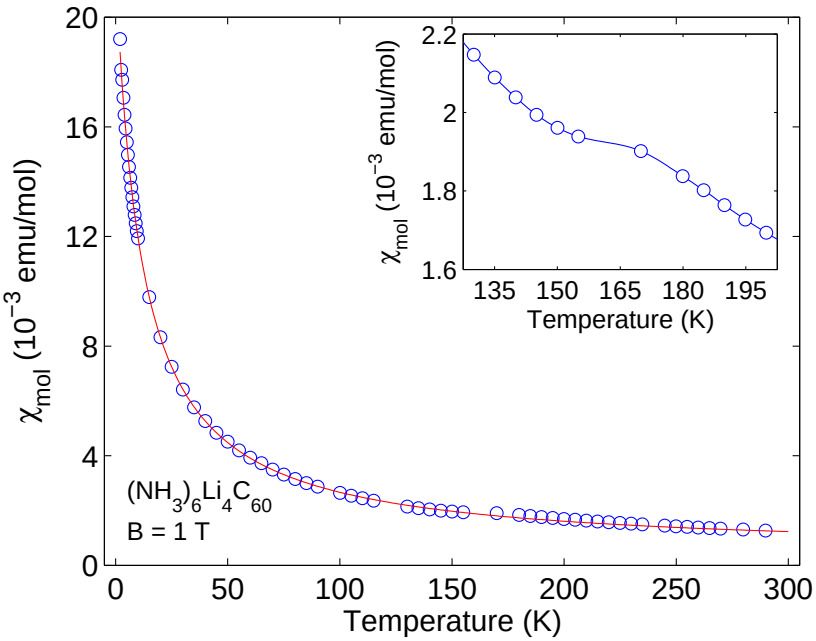

Figure 6.19: Magnetic behaviour of $(NH_3)_6Li_4C_{60}$.

factor and J the total angular moment. In case of free electron spins, $g = 2$ and $J = 1/2$, and n represents the number of free $1/2$ spins on the molecule; this is usually a good approximation for an electron in a molecular orbital, because the orbital angular moment is quenched [104]. The extracted values for p, and n for $x = 3$ and $x = 4$ resulted respectively $p = 0.834\,\mu_B$, $n = 0.23$ and $p = 1.41\mu_B$, $n = 0.67$. On one hand, the magnetic moment per C_{60} units turn out to be unexpectedly low and does not match the even-odd effect due to the electron filling of the t_{1u}-derived band, if a complete charge transfer on the buckyball is admitted. Nevertheless, these values are too high to arise from paramagnetic impurities, thus substantially confirming an insulating nature for these compounds. Probably other effects could be involved in this anomalous behaviour and a clear explanation of these results is not yet achieved.

6.5 The series $Li_xNa_{4-x}C_{60}$

In order to investigate new unusual polymeric structures, a part of this work was devoted to the preparation and the characterisation of the mixed phases $Li_xNa_{4-x}C_{60}$, with $0 < x < 4$. Both the phases at the extremes of this series in fact consist of two-dimensional polymers: Li_4C_{60}, which revealed to have the unique hybrid struc-

ture described previously, with insulating character, and Na_4C_{60}, which from literature results a single bonded metallic polymer [40]. The study of the features of the intermediate stoichiometries is important also because it could provide new insight in the knowledge of the two polymers, in particular which are the parameters that determine the two polymeric structures. Further information could arise from the investigation of the structure and the electronic properties of the high temperature phases, when any bonding structure is prevented.

This study is still in progress, hence only the preliminary results will be discussed.

6.5.1 Sample preparation and preliminary x-ray investigation

The series $Li_xNa_{4-x}C_{60}$, with $0 \leq x \leq 4$, was prepared directly by thermal evaporation of alkali metal, as described in sec. 5.3. This technique was preferred with respect that based on thermal decomposition of lithium and sodium azides; in fact, preliminary efforts to produce polymeric Na_4C_{60} starting from sodium azide did not allow to obtain well polymerised samples, probably due to the too short annealing time which characterised this preparation method. Hence the samples were annealed at 270° C for three weeks in an evacuated Pyrex tube, with several intermediate regrinding.

Preliminary laboratory x-ray diffraction (CuK_α), performed at room temperature, indicates that all the samples were characterised by a good crystallinity; in particular, Li_4C_{60} and Na_4C_{60} appeared homogeneous and the peaks match those of the two polymeric proposed structure [88, 40, 41], thus guaranteeing that the reaction occurred. The diffraction pattern of the phase with $x = 3$, due probably to the low resolution of the measurements, turn out to be practically undistinguishable from that of Li_4C_{60}. On the other hand, $Li_2Na_2C_{60}$ and Li_3NaC_{60} contained at least two phases, where the majority contribution probably arose from those of Li_4C_{60} and Na_4C_{60} polymers. The same features were also indicated by Roding et al. [91].

6.5.2 Synchrotron radiation diffraction results

Further insight came from a more detailed investigation, started from synchrotron x-ray powder diffraction taken on the same sample at room temperature. The measures were performed at ESRF-ID31, and the selected wavelength of the radiation used was $\lambda = 0.85055$ Å. In fig. 6.20 the diffraction profiles for the whole series is displayed. Thanks to the higher resolution of the data, it was possible to analyse them with Le Bail pattern decomposition, in GSAS, and the results were summarised in tab. 6.8.

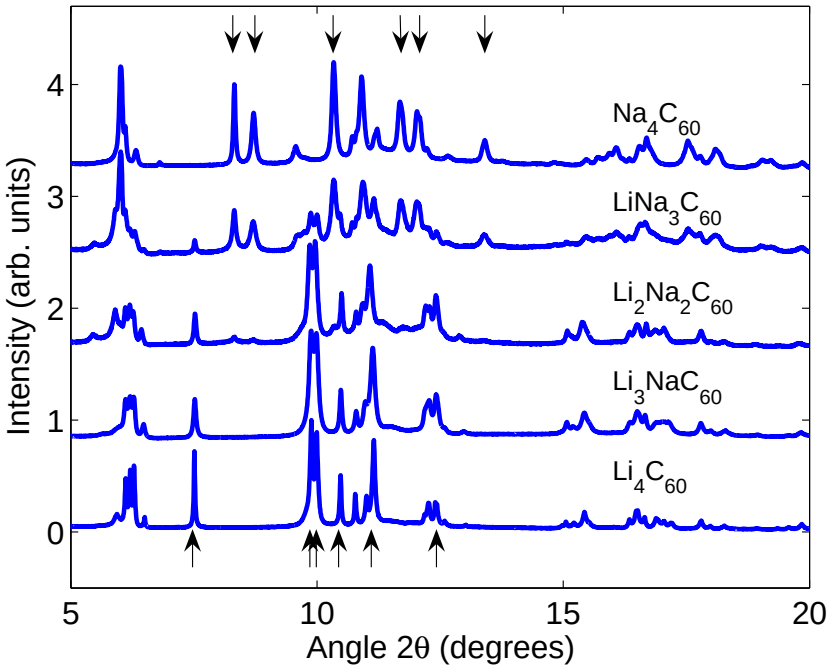

Figure 6.20: High resolution powder diffraction patterns of the series $Li_xNa_{4-x}C_{60}$ with $0 \leq x \leq 4$. The arrows indicate the main peaks of the Li_4C_{60} and Na_4C_{60} phases. The intermediate stoichiometries show phase-segregation of these two polymeric phases.

These results substantially confirmed the preliminary analysis of laboratory x-ray data. Good agreement factors, in fact, were obtained simply by fitting the diffractograms with the cell of Li_4C_{60}, in case of Li_3NaC_{60}, or a mixture of Li_4C_{60} and Na_4C_{60} for the other two mixed stoichiometries. In $Li_2Na_2C_{60}$ a further minority *fcc* phase was introduced, to take into account several otherwise not indexed peaks. However, no evident traces of unreacted C_{60} or of other Na_xC_{60} phases were observed.

The sensitive modifications of the cell parameters for both the phases, observed when x varies in the compounds, could be due to a possible diffusion of the two alkali species in the two phases, which however is such that the original symmetry is retained. This fact seems to be confirmed also by preliminary Rietveld analysis, but the work on this issue is still in progress.

6.5.3 Thermal treatments

The structure of the phases observed at room temperature underwent a deep transformation when the samples are heated above 300° C. At this temperature, as observed

	$\mathbf{Li_4C_{60}}$ (s. g. **I 2/m**)			
	a (Å)	**b(Å)**	**c(Å)**	β (°)
$\mathbf{Li_4C_{60}}$	9.31393(9)	9.0552(1)	14.9997(1)	90.925(1)
$\mathbf{Li_3NaC_{60}}$	9.3057(2)	9.0389(2)	15.0355(3)	90.930(2)
$\mathbf{Li_2Na_2C_{60}}$ *	9.2921(4)	9.0404(5)	15.1406(6)	89.058(2)
$\mathbf{LiNa_3C_{60}}$	9.3187(8)	9.0083(8)	15.021(1)	91.051(7)
$\mathbf{Na_4C_{60}}$	/	/	/	/
	$\mathbf{Na_4C_{60}}$ (s. g. **I 2/m**)			
	a(Å)	**b(Å)**	**c(Å)**	β (°)
$\mathbf{Li_4C_{60}}$	/	/	/	/
$\mathbf{Li_3NaC_{60}}$	/	/	/	/
$\mathbf{Li_2Na_2C_{60}}$ (*)	11.296(4)	11.756(4)	10.192(4)	95.10(4)
$\mathbf{LiNa_3C_{60}}$	11.2705(5)	11.7152(4)	10.2207(5)	96.069(5)
$\mathbf{Na_4C_{60}}$	11.2547(4)	11.7145(3)	11.2563(3)	96.145(3)

Table 6.8: Refined cell parameters for the series $Li_xNa_{4-x}C_{60}$, with $0 \leq x \leq 4$, obtained with powder pattern decomposition of synchrotron data. Good agreement are reached by considering the phases of Li_4C_{60} or Na_4C_{60}, or a mixture of them. (*) In $Li_2Na_2C_{60}$ further peaks, referred to a minority cubic *fcc* phase, were also observed (s. g. $\mathbf{F\,m\,\overline{3}\,m}$, $a = 14.290(2)$ Å).

also for the pristine phases of Li_4C_{60} and Na_4C_{60}, the thermal excitation overcomes the bonding energy, and the compounds are in a monomer phase. Despite the lack of homogeneity of the precursors, the reflections in the high temperature diffraction profiles of mixed $Li_xNa_{4-x}C_{60}$ compounds are all well indexed by a single phase, and the variation of the x parameter in the series leads to an unexpected wealth of different molecular arrangements, as shown in fig. 6.21. Li_3NaC_{60} is characterised by *fcc* symmetry, thus resembling the monomer phase of Li_4C_{60}. On the contrary, both $Li_2Na_2C_{60}$ and $LiNa_3C_{60}$ (not shown here) display an unusual *hcp* hexagonal cell, similar to that observed in the hexagonal phase of pristine C_{60} [105, 106, 107]. Finally, Na_4C_{60} is characterised by a tetragonal symmetry, with the presence of a minority *fcc* phase, absolutely in agreement with [42]. Due to the atypical *hcp* arrangement of fullerene units in $Li_2Na_2C_{60}$, as compared with the other known alkali doped structures, preliminary structural investigation focussed on this compound. A more careful analysis of the diffraction profile revealed that the structure is characterised by an high level of disorder and faulting; this feature appears as a not homogeneous broadening of the reflections for which $h - k = 3t \pm 1$, where t is an integer [108], and on the typical asymmetric shape of several peaks [109, 110]. Investigation of the systematic absences in the pattern profile allowed to restrict the class of possible spatial groups to seven candi-

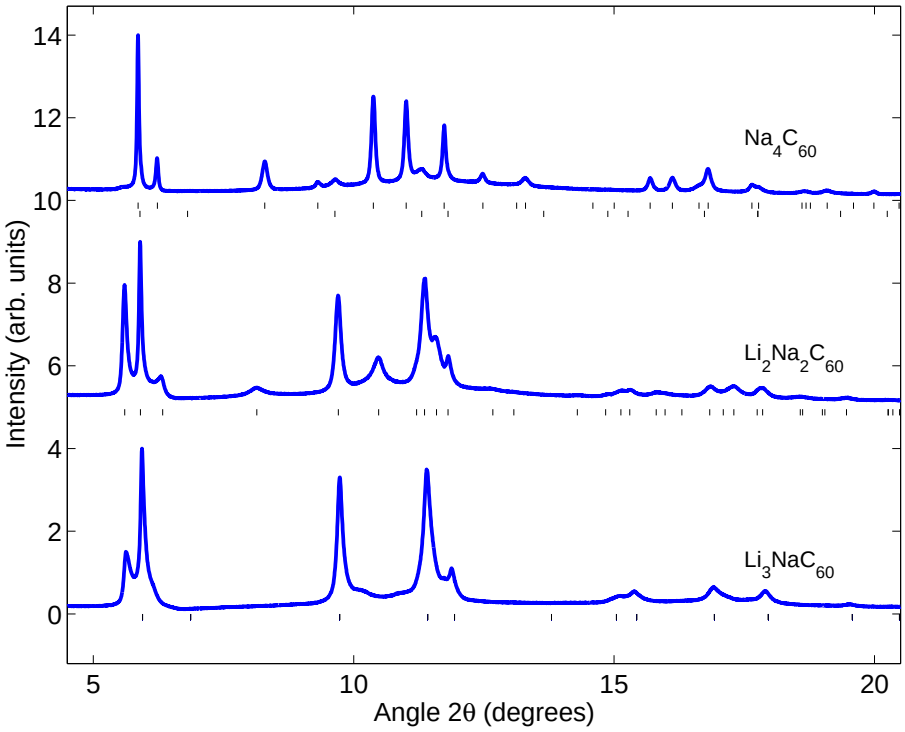

Figure 6.21: The three different structural phases observed from synchrotron radiation diffraction performed on $Li_xNa_{4-x}C_{60}$ at high temperature. a) Powder pattern of Li_3NaC_{60} at $T = 350°$ C is compatible with a cubic *fcc* symmetry, whereas b) $Li_2Na_2C_{60}$ at $T = 350°$ C is well indexed as hexagonal *hcp* cell; finally c) Na_4C_{60} at $T = 300°$ C turn out to be tetragonal *bct*, with a minority cubic phase, as already described in [42]. The mixed stoichiometry shows evident effects derived by presence stacking faults in the structure.

dates: **P 6$_3$ m c** (186), **P $\bar{6}$ 2 c** (190), **P 6$_3$/m m c** (194), **P 6 c c** (184), **P 6/m c c** (192) if the symmetry is hexagonal, **P 3 c 1** (158), **P $\bar{3}$ c 1** (165) if the symmetry is trigonal. The similarity of the observed structure with that of the hexagonal phase of pristine C_{60} [105] suggested **P 6$_3$/m m c** as the best choice. Le Bail pattern decomposition of the data taken at $T = 430°$ C using this symmetry led to obtain a good agreement ($R_{wp} = 5.44\%$) and provided the following refined parameters: $a = 10.0726(2)$ Å, $c = 16.5570(5)$ Å, $\gamma = 120°$. The shortest C_{60}-C_{60} contact turn out to be ~ 10.07 Å, a value slightly higher than that of monomeric Li_4C_{60} at the same temperature (~ 9.97 Å) and is compatible with the compound in the plastic state.

The starting structural model proposed for $Li_2Na_2C_{60}$ consisted hence of freely rotating fullerenes, placed in the special positions $(\frac{1}{3}, \frac{2}{3}, \frac{1}{4})$ and $(\frac{2}{3}, \frac{1}{3}, \frac{3}{4})$ of the hexagonal cell, the *hcp* packing being generated by the symmetry operations of the space group

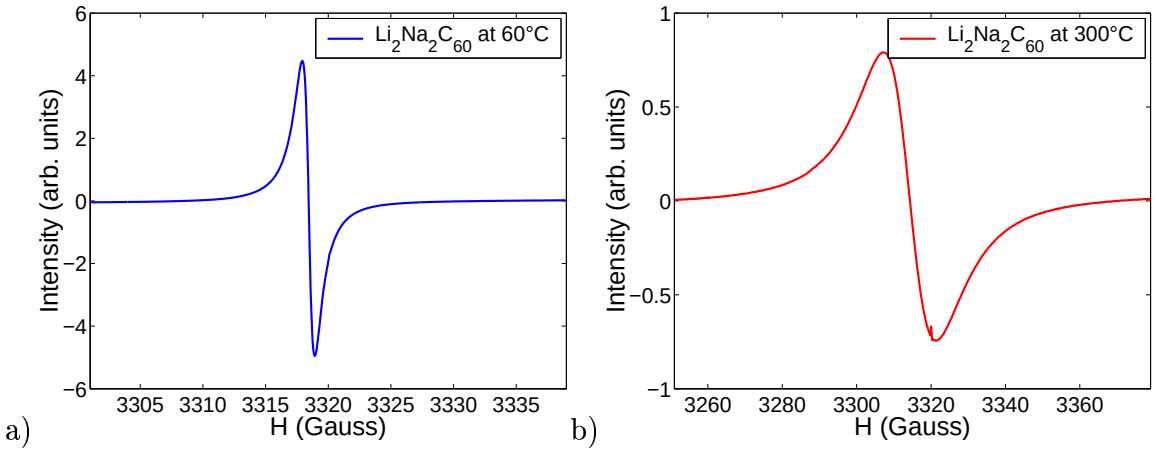

Figure 6.22: Preliminary ESR measurements on $Li_2Na_2C_{60}$ at a) 60° C (mixed polymeric phase), and b) at 300° C (monomer state). In both the cases, line-shape is well fitted with a Lorentzian function, thus indicating that no metal-to-insulator transitions occur in this compound in consequence of the depolymerisation process.

[105]. To take into account the effects of the C_{60} dynamics, buckyball were modelled by spherical shells with FULLPROF program. However, the agreement between experimental and calculated intensities, obtained with preliminary Rietveld refinement, resulted unexpectedly poor ($R_{F^2} = 33.4\%$), thus suggesting that a further minority phase, probably cubic, could be superimposed to the hexagonal reflections. The structure analysis of $Li_2Na_2C_{60}$ is still in progress, in order to determine without ambiguity the features of this phase.

6.5.4 Electronic properties of $Li_2Na_2C_{60}$

The peculiar structural features observed in the high temperature monomer $Li_2Na_2C_{60}$ phase stimulated the interest on the electronic properties of this compound, in order to estabilish a comparison with monomer Li_4C_{60} and Na_4C_{60}. As already discussed in detail, both these two phases display a metallic behaviour (see sec. 6.2.2 and [42]), as evidenced by the Dysonian lineshape of the ESR signal.

Preliminary CW ESR measurements were performed on $Li_2Na_2C_{60}$ at different temperatures, in collaboration with Dr. Denis Arčon, at the Jozef Stefan Institute of Ljubljana. In fig. 6.22 the line-shape of the ESR signal, respectively at $T = 60°$ C and $T = 300°$ C, are shown. At the lowest temperature, the line appears very narrow, as found also for polymeric Li_4C_{60}. The absence of strong asymmetry in the profile both in the polymer and especially in the monomer phase, confirmed by the good fit

of the line-shape with a Lorentzian function, suggest that no metal-to-insulator transition takes place in this sample. Probably the higher interfullerene distance which was detected in this compound, as compared with that of the other metallic A_4C_{60} phases (see tab. 6.6), plays an important role in inducing electronic localisation; nevertheless, it is still not clear if the unusual hexagonal crystal symmetry could provide a further contribution and favour an insulating state. Further Raman and ESR measurements are scheduled, in order to evaluate the effective charge transfer on these compound and to investigate the electronic properties of the other mixed stoichiometries; this investigation could contribute to define the role played both by the crystal symmetry and by the C_{60}-C_{60} distance in driving the electronic properties of these highly correlated systems.

Conclusions

In this work a detailed investigation of lithium intercalated fullerides and other derivative compounds was performed, ranging from the synthesis and the first characterisation of the samples, to the structural and spectroscopic study, respectively with high resolution synchrotron diffraction and Raman spectroscopy. This allowed to shed new light on the interesting properties of this class of compounds, which, if compared to other alkali doped fullerides, is somewhat less investigated, probably due to the difficulties encountered during their preparation.

First, the Li_xC_{60} series ($1 \leq x \leq 6$) was considered; Li_4C_{60}, which after a preliminary x-ray diffraction analysis appeared as the representative of these compounds, underwent synchrotron radiation diffraction (ESRF-Grenoble). The systematic Rietveld refinement of collected data showed that the compound is an unusual hybrid polymer, in which both four membered carbon rings ("double" bonds) and single C-C bonds coexist and give rise to a two-dimensional network. An analogous structure characterises also the other compounds with $3 \leq x \leq 5$. This feature is rather peculiar in the family of fullerene polymers, because so far only structures with one type of bonding motif, either single or "double", have been observed. Parallel ^{13}C NMR/MAS and Raman spectroscopy substantially confirmed this result, indicating that the as prepared polymer presents a diamagnetic insulating character. The atypical bonding scheme was found to depend on the peculiar lithium characteristics, as compared with the other alkali metals; in particular, as indicated by the structural analysis, the small Li^+ ionic radius is of paramount importance in stabilising such a close packing of fullerenes, giving rise to polymerisation. Although Raman spectroscopy revealed to be a valuable tool for probing the amount of charge transferred to C_{60} in monomeric fullerides, the empirical rules adopted in that case proved not to be reliable in the case of polymers. The question on the amount of transferred charge to C_{60} is thus still open.

Subsequent study of Li_4C_{60} depolymerisation, induced by thermal treatments, provided other interesting results. Above $\sim 325°$ C, the polymeric bonds are completely broken, and a new monomer face-centered cubic phase appears. From high tempera-

ture ESR, Raman and preliminary ^{13}C NMR spectroscopy measurements, it is evinced that monomer Li_4C_{60} behaves as a metal. Furthermore, from Raman investigation of the $A_g(2)$ mode downshift, a full charge transfer of four electrons to the bucky-ball was detected. These results were fully supported also by an exhaustive Rietveld analysis of the synchrotron powder diffraction profile of monomer Li_4C_{60}, in which rotating fullerene molecules were modelled with symmetry adapted spherical harmonics (SASH). The metallicity of *fcc* monomer Li_4C_{60} is rather atypical, as compared with the other A_4C_{60} systems (A=K, Rb, Cs), which on the contrary turn out to be all *bct* nonmagnetic insulators; it seems to be rationalised only if the higher site symmetry of the lithium fulleride is taken into account, thus favouring the electronic hopping in this highly correlated system. These result could shed new light on future theoretical studies on these systems.

Other investigations focussed on the ammoniated phases of lithium-doped fullerides. The intercalation of ammonia molecules in Li_xC_{60} prevented the polymerisation of the fullerenes also at low temperatures, and allowed to obtain a totally different body centered cubic phase. The noticeable interfullerene distance observed in this phase provoked the localisation of the electrons in these compounds, as shown by the strongly temperature-dependent magnetic response of the samples. Despite the evidence of a Curie-Weiss like magnetic susceptibility, no antiferromagnetic order was detected in these compounds, unlike previously reported in literature.

To gain further insight on the unusual structural and electronic properties of Li_4C_{60}, a systematic investigation of the mixed phases $Li_xNa_{4-x}C_{60}$ was also started. High resolution synchrotron radiation diffraction on the as prepared compounds evidenced the segregation of the two polymeric phases of Li_4C_{60} and Na_4C_{60}. On the contrary, the structural analysis performed at high temperature, when the compounds are in a monomer form, showed a wealth of different phases, depending on the alkali stoichiometry, which are still under study. In particular, monomer $Li_2Na_2C_{60}$, is characterised by an unusual *hcp* structure, in which, from preliminary ESR measurement no metallic character was observed. Further investigations are required in order to unambiguously define the effect of the structural features of these systems on the overall electronic behaviour.

Appendix A

Multipole expansion of orientational distributions

As already seen in chap. 2, fullerite and fullerides are generally plastic solids, in which fullerene units are free to rotate around their centre of simmetry. If an accurate diffraction analysis of these compounds should be performed, it is necessary to seriously take into account this aspect. In this section the theory for the analytical treatment of the orientational distribution in librating rigid molecules, developed by M. Kara and K. Suonio [51] is described; the particular case of the icosahedral C_{60} molecule placed in a cubic site, is discussed in more detail.

Static and dynamic densities

Let us consider a rigid molecule, free to rotate around a fixed point. In general, the electronic density distribution describing the molecule, in the *static* (σ) and in the *dynamic* (ρ) case respectively, can be expressed as a *multipole expansion* of the product of the two radial and angular components, as:

$$\sigma(\mathbf{r}) = \sum_{l\,mp} \sigma_{l\,mp}(r) y_{l\,mp}(\theta, \phi) \tag{6}$$

$$\rho(\mathbf{r}) = \sum_{l\,mp} \rho_{l\,mp}(r) y_{l\,mp}(\theta, \phi) \tag{7}$$

where $y_{l\,mp}(\theta, \phi)$ are the *normalised real spherical harmonics*, defined as [51]:

$$y_{lmp}(\theta, \phi) = \left[\frac{1}{1+\delta_{m0}} \frac{2l+1}{2\pi} \frac{(l-m)!}{(l+m)!} \right]^{\frac{1}{2}} \cdot P_l^m(\cos\theta) \begin{cases} \cos m\phi & \text{if } p = + \\ \sin m\phi & \text{if } p = - \end{cases} \tag{8}$$

here $P_l^m(\cos\theta)$ are the *Legendre associated polynomials*, and $l = 0, 1, ..., m = 0, 1, ..., l$ and p is the parity. In x-ray diffraction studies, the density function physically consists

of the electron density.

The relationship between the static density $\sigma(\mathbf{r})$ and the dynamic density $\rho(\mathbf{r})$ is determined by the *orientational distribution* $f(\alpha, \beta, \gamma) = f(\omega)$ through the expression:

$$\rho(\mathbf{r}) = \int f(\omega)\Re(\omega)\sigma(\mathbf{r})d\omega \tag{9}$$

where $\Re(\omega)$ denotes a *rotation* through Eulerian angles α, β, γ about the centre of mass of the molecule, Actually, $f(\omega)$ is a orientation probability density, hence $f(\omega) \geq 0$ and $\int f(\omega)d\omega = 1$.

The static density must reflect the geometry, and hence to the *body symmetry* of the molecule; on the contrary, the dynamical density is constrained by the *site symmetry*, which depends on the geometry of the overall crystal.

An orientational distribution $f(\omega)$ is site symmetric if it produces from any static density $\sigma(\mathbf{r})$ through eq. 9 *a site symmetric dynamic density $\rho(\mathbf{r})$.*

In the following discussion, the relations between *body* and *site* symmetry constraints on the dynamic density of a libration molecule, in terms of selection rules on multipole expansion coefficients, will be shown.

Thanks to its symmetry, the radial component of $\sigma(\mathbf{r})$ in the eq. 9 is insensitive to the effect of the rotation operator $\Re(\omega)$, and hence only the angular part $y_{l\,mp}(\theta, \phi)$ is changed. The transformation properties of spherical harmonics under rotations are defined by the *Wigner functions*, which form a convenient orthonormal basis. For the real spherical harmonics, the rotation is expressed by the equation:

$$\Re(\omega)y_{l\,mp}(\theta, \phi) = \sum_{nr} C^l_{nr\,mp}(\omega)y_{l\,nr}(\theta, \phi) \tag{10}$$

where $C^l_{nr\,mp}(\omega)$ are the real *Wigner functions* [51], and the relation $\int (C^l_{nr\,mp})^2 d\omega = 8\pi^2/(2l+1)$ holds; the indices l, mp are referred to the initial set of spherical harmonics, whereas the indeces l, nr to the rotated one. In an analogous position, also the orientational distribution can be represented as a real expansion:

$$f(\omega) = \sum_{l\,nr\,mp} a^l_{nr\,mp} C^l_{nr\,mp}(\omega)d\omega \tag{11}$$

where the coefficients $a^l_{nr\,mp}$ represent the "weights" which define the probability of the

distribution, and are given by:

$$a^{l}_{nr\,mp} = \frac{2l+1}{8\pi^2} \int f(\omega) C^{l}_{nr\,mp}(\omega) d\omega \tag{12}$$

Inserting eq. 6, 10 and 11 in eq. 9 leads the following espression for the dynamical density:

$$\rho(\mathbf{r}) = \int \sum_{lnrmp,l'n'r'm'p'} a^{l'}_{n'r'm'p'} \cdot C^{l'}_{n'r'm'p'}(\omega) \sigma_{l\,mp}(r) \cdot C^{l}_{nr\,mp}(\omega) y_{l\,nr}(\theta,\phi) d\omega =$$

$$= \sum_{l\,nr} \left[\frac{8\pi^2}{2l+1} \sum_{mp} a^{l}_{nr\,mp} \sigma_{l\,mp}(r) \right] y_{l\,nr}(\theta,\phi) \tag{13}$$

The comparison of eq. 7 and 13 yields the radial dynamical density:

$$\rho_{l\,nr}(r) = \frac{8\pi^2}{2l+1} \sum_{mp} a^{l}_{nr\,mp} \sigma_{l\,mp}(r) \tag{14}$$

This important results shows that:

- The radial density of the site-symmetric dynamic multipole expansion is a linear combination of the radial density of the body-symmetric static multipole expansion, of the *same* multipole order l.
- Since the dynamical density must satisfy the site symmetry, hence $\rho_{l\,nr} \equiv 0$ for the indices l, n, r which violate the selection rules of the site symmetry. The corresponding coefficients $a^{l}_{nr\,mp}$ for all mp must vanish.
- This is true *irrespective* of the radial densities $\sigma_{l\,mp}$, because, in general, the body symmetry could be lower than the site symmetry.
- These selection rules coincide with those that make the basis $\{y_{l\,nr}(\theta,\phi\}$ of density functions site symmetric.

Cubic sites

If the site symmetry is cubic, it is possible, to simplify the calculus, by making unitary transformation of the $\{y_{l\,nr}(\theta,\phi)\}$ basis, to obtain another real orthonormal basis $\{K_{lj}\}$:

$$K^{cub}_{lj}(\theta,\phi) = \sum_{mp} k^{cub}_{l\,mp\,j} y_{lmp}(\theta,\phi) \tag{15}$$

These functions called *cubic harmonics* were first proposed by Bethe [96] and they consist of linear combinations of real spherical harmonics. In tab. 1 the cubic conversion factors up to the order ten are reported [51]:

Even	mp					
l, j	0+	2+	4+	6+	8+	10+
0 1	1					
4 1	$\frac{1}{2}\left(\frac{7}{3}\right)^{1/2}$		$\frac{1}{2}\left(\frac{5}{3}\right)^{1/2}$			
6 1	$\frac{1}{2}\left(\frac{1}{2}\right)^{1/2}$		$-\frac{1}{2}\left(\frac{7}{2}\right)^{1/2}$			
6 2		$\frac{1}{4}11^{1/2}$		$-\frac{1}{4}5^{1/2}$		
8 1	$\frac{1}{8}33^{1/2}$		$\frac{1}{4}\left(\frac{7}{3}\right)^{1/2}$		$\frac{1}{8}\left(\frac{65}{3}\right)^{1/2}$	
10 1	$\frac{1}{8}\left(\frac{65}{6}\right)^{1/2}$		$-\frac{1}{4}\left(\frac{11}{2}\right)^{1/2}$		$-\frac{1}{8}\left(\frac{187}{6}\right)^{1/2}$	
10 2		$\frac{1}{8}\left(\frac{247}{6}\right)^{1/2}$		$\frac{1}{16}\left(\frac{19}{3}\right)^{1/2}$		$-\frac{1}{16}85^{1/2}$
Odd	mp					
l, j		2−	4−	6−	8−	
3 1		1				
7 1		$\frac{1}{2}\left(\frac{16}{6}\right)^{1/2}$		$\frac{1}{2}\left(\frac{11}{6}\right)^{1/2}$		
9 1		$\frac{1}{4}3^{1/2}$		$-\frac{1}{4}13^{1/2}$		
9 2			$\frac{1}{2}\left(\frac{17}{6}\right)^{1/2}$		$-\frac{1}{2}\left(\frac{7}{6}\right)^{1/2}$	

Table 1: Cubic conversion factors $k^{cub}_{l\,mp\,j}$ up to tenth order from [51].

In ref. [111] it is possible to find the conversions up to the 30-th order. Further index rules are given for the five cubic site symmetries (tetrahedral and octahedral) **23** (T), **m3** (T_h), **432** (O), $\overline{\mathbf{4}}$**3m** (T_d) and **m3m** (O_h), as represented in tab. 2.

The same results can be obtained also by using this basis, if the site symmetry is cubic; in this case the rotator functions $C^{cub}_{lj\,mp}(\omega)$, which describe the rotation of the cubic harmonics are unitary transformations of the real Wigner functions:

$$C^{cub}_{lj\,mp}(\omega) = \sum_{nr} k^{cub}_{l\,nr\,j} C^{l}_{nrmp}(\omega) \tag{16}$$

and, starting from the generic static density $\sigma(\mathbf{r})$ of eq. 6, the dynamical density is now expressed as:

$$\rho(\mathbf{r}) = \sum_{lj} \left[\frac{8\pi^2}{2l+1} \sum_{nr} a^{cub}_{lj\,nr} \sigma_{l\,nr}(r) \right] K^{cub}_{lj}(\theta, \phi) \tag{17}$$

	Point group				
	23	**m3**	**432**	**$\bar{4}$3m**	**m3m**
l, j					
0 1	x	x	x	x	x
3 1	x			x	
4 1	x	x	x	x	x
6 1	x	x	x	x	x
6 2	x	x			
7 1	x			x	
8 1	x	x	x	x	x
9 1	x			x	
9 2	x		x		
10 1	x	x	x	x	x
10 2	x	x			

Table 2: Index rule for cubic symmetries (from [51]).

where the radial part is:

$$\rho_{lj} = \frac{8\pi^2}{2l+1} \sum_{nr} a^{cub}_{lj\,nr} \sigma_{l\,nr}(r) \tag{18}$$

Again, the expansion coefficient $a^{cub}_{lj\,nr}$ of the orientational distribution, expressed in a symilar way as eq. 12, must vanish identically, unless the basis function $K^{cub}_{lj}(\theta, \phi)$ represents a cubic harmonic of the site symmetry. This means that, in general, the multipole expansion of $\rho(\mathbf{r})$ will contain a smaller number of terms than the expansion of $\sigma(\mathbf{r})$, due to the site symmetry restrictions. In fig. 1 some *cubic* harmonics, up to the 10-th order, are displayed.

Icosahedral body symmetry

The molecular symmetry defines the sequence of indices in the multipole expansion (eq. 6) of the static density. For an icosahedral molecule it can be expanded on the basis of the *normalised icosahedral harmonics* [51]:

$$K^{ico}_{lj}(\theta, \phi) = \sum_{nr} k^{ico}_{l\,nr\,j} y_{l\,nr}(\theta, \phi) \tag{19}$$

and the static density is expressed by:

$$\sigma(\mathbf{r}) = \sum_{ij} \sigma^{ico}_{lj}(r) K^{ico}_{lj}(\theta, \phi) \tag{20}$$

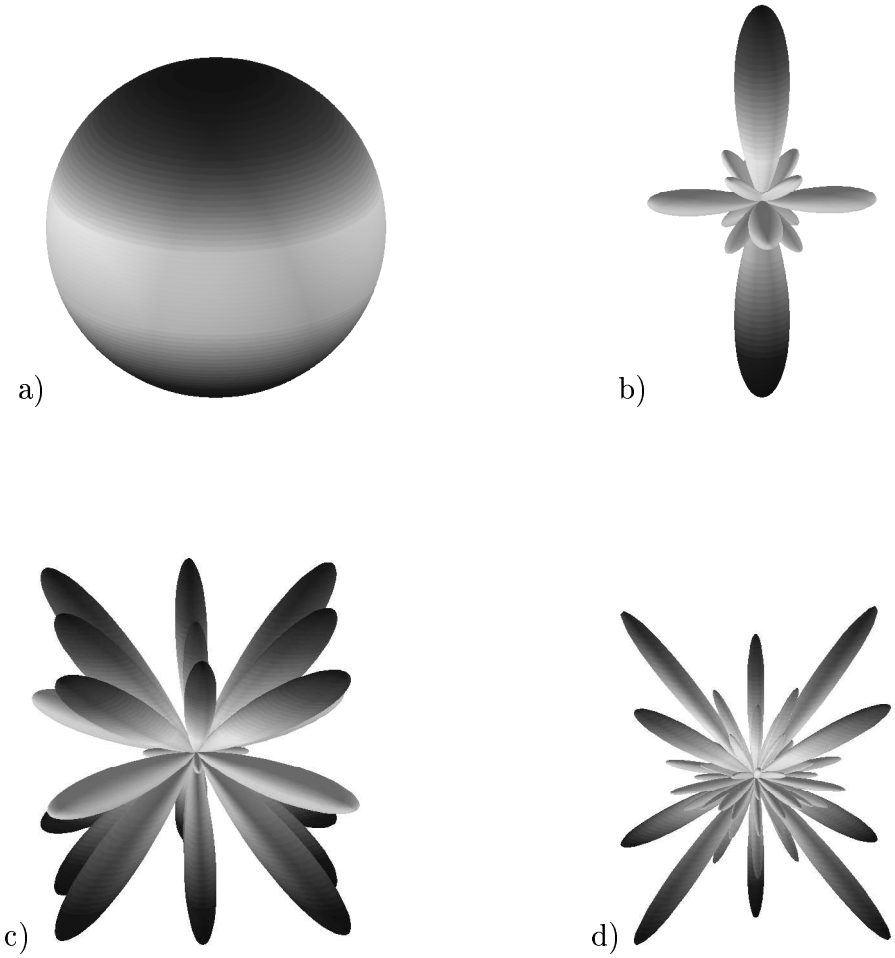

Figure 1: Cubic harmonics of different orders: a) $l = 0$, $j = 1$; b) $l = 4$, $j = 1$; c) $l = 6$, $j = 1$ and d) $l = 10$, $j = 1$.

Here, only the terms σ_{lj}^{ico} which satisfy the body symmetry are non-zero. In tab. 3 the icosahedral conversion factor up to the tenth order are given, with the same choice of coordinate axes are chosen as indicated in [51].

	mp		
l, j	0+	5+	10+
0 1	1		
6 1	$\frac{1}{5}11^{1/2}$	$-\frac{1}{5}14^{1/2}$	
10 1	$\frac{1}{25}\left(\frac{247}{3}\right)^{1/2}$	$\frac{1}{25}418^{172}$	$\frac{1}{25}\left(\frac{374}{3}\right)^{1/2}$

Table 3: Icosahedral conversion factors k_{lnrj}^{ico} up to tenth order, corresponding to the coordinate axes chosen as indicated in [51].

C_{60} molecule in a m3m cubic site

If a C_{60} molecule (belonging to the icosahedral point group) is free to rotate about its centre of symmetry in a cubic site with symmetry **m3m**, it is possible to obtain an analytical expression for its dynamical density, by following the method descibed above, starting from the knowledge of the static density $\sigma(\mathbf{r})$. The rotation of icosahedral harmonics in cubic sites is now represented by an equation analogous to eq. 9, in which the *icosahedral-body cubic site rotators* appear [51]:

$$C^{cub-ico}_{l\,i\,j}(\omega) = \sum_{nr\,mp} k^{cub}_{l\,nr\,i} k^{ico}_{l\,mp\,j} C^{l}_{nr\,mp}(\omega) \tag{21}$$

The final expression of the dynamical density $\rho(\mathbf{r})$ is:

$$\rho(\mathbf{r}) = \sum_{li} \rho_{li}(r) K^{cub}_{li}(\theta, \phi) \tag{22}$$

where:

$$\rho_{li}(r) = \sum_{j} \frac{8\pi^2}{2l+1} a^{cub-ico}_{l\,i\,j} \sigma^{ico}_{lj}(r) \tag{23}$$

and:

$$a^{cub-ico}_{l\,i\,j} = \frac{2l+1}{8\pi^2} \int f(\omega) C^{cub-ico}_{l\,i\,j}(\omega) d\omega \tag{24}$$

In this case, the selection rules of the body icosahedral symmetry, characterising $\sigma^{ico}_{lj}(r)$, are more stringent than those of the site. This obviously reflected on the sequence of the l, i indices of the expansion of $\rho(\mathbf{r})$ in eq. 22. In particular, referring to tab. 2 and tab. 3, if one considers the cubic expansion of the dynamic density up to the tenth order (which is sufficient in most cases), only three terms remain, corresponding to the couples $(l,\, i) = (0,\, 1), (6,\, 1), (10,\, 1)$.

Bibliography

[1] H. W. Kroto, J. R. Heath, S. C. O'Brien, R. F. Curl, and R. E. Smalley, "C_{60} : Buckminsterfullerene", Nature **318,** 162 (1985).

[2] W. Kratschmer, L. D. Lamb, K. Foristopoulos, and D. R. Huffman, "Solid C_{60} : a new form of carbon", Nature **347,** 354 (1990).

[3] P. W. Stephens, L. Mihaly, P. L. Lee, R. L. Whetten, S. M. Huang, R. Kaner, F. Deiderich, and K. Holczer, "Structure of single-phase superconducting K_3C_{60}", Nature **351,** 632 (1991).

[4] T. Takenobu, T. Muro, Y. Iwasa, and T. Mitani, "Antiferromagnetism and phase diagram in ammoniated alkali fulleride salts", Phys. Rev. Lett. **85,** 381 (2000).

[5] L. Forró and L. Mihaly, "Electronic properties of doped fullerides", Rep. Prog. Phys. **64,** 649 (2001).

[6] T. L. Makarova, B. Sundqvist, P. Esquinazi, R. Höhne, Y. Kopelevich, P. Scharff, V. A. Davydov, L. S. Kashevarova, and A. V. Rakhmanina, "Magnetic carbon", Nature **413,** 716 (2001).

[7] J. Kohanoff, W. Andreoni, and M. Parrinello, "A possible new higly stable fulleride cluster: $Li_{12}C_{60}$", Chem. Phys. Lett. **198,** 472 (1992).

[8] M. Kosaka, K. Tanigaki, K. Prassides, S. Margadonna, A. Lappas, and C. M. Brown, "Superconductivity in Li_xCsC_{60}", Phys. Rev. B **59,** 6628 (1999).

[9] M. Yasukawa and S. Yamanaka, "Synthesis of Li_xC_{60} (x=1 - 28) fullerides under high-pressure and high temperature conditions and their electrical properties", Chem. Phys. Lett. **341,** 467 (2001).

[10] L. Cristofolini, M. Riccò, and R. D. Renzi, "NMR and high resolution x-ray diffraction evidence of an alkali-metal fulleride with large interstitial clusters: $Li_{12}C_{60}$", Phys. Rev. B **59,** 8343 (1999).

[11] T. Wågberg, P. Stenmark, and B. Sundqvist, "Structural aspects of two-dimensional polymers: Li_4C_{60}, Na_4C_{60} and tetragonal C_{60}. Raman spectroscopy and x-ray diffraction", J. Phys. Chem. Sol. **65,** 317 (2004).

[12] M. Belli, "Magnetic and transport properties of intercalated fullerides", Ph. D. Thesis (2006).

[13] P. A. Heiney, J. E. Fisher, A. R. McGhie, and W. J. Romanow, "Orientational ordering transition in solid C_{60}", Phys. Rev. Lett. **66,** 2911 (1991).

[14] D. M. Cox *et al.*, "Characterization of C_{60} and C_{70} clusters", J. Am. Chem. Soc. **113,** 2940 (1991).

[15] Q. Xie, E. Perez-Cordero, and L. Echegoyen, "Electrochemical detection of $C_{60}{}^+$ and $C_{70}{}^+$: enhanced stability of fulleride solution", J. Am. Chem. Soc. **114,** 3978 (1992).

[16] Y. Iwasa and T. Takenobu, "Superconductivity, Mott Hubbard states, and molecular orbital order in intercalated fullerides", J. Phys. Condens. Matt. **15,** R495 (2003).

[17] R. C. Haddon *et al.*, "Conducting films of C_{60} and C_{70} by alkali-metal doping", Nature **350,** 320 (1991).

[18] C. A. Kuntscher and G. M. Bendele, "Alkali-metal stoichiometry and structure of K_4C_{60} and Rb_4C_{60}", Phys. Rev. B **55,** 3366 (1997).

[19] R. F. Kiefl *et al.*, "Evidence of endohedral muonium in K_xC_{60} and consequences for electronic structure", Phys. Rev. Lett. **69,** 2005 (1992).

[20] U. Mizutani, in *Introduction to electron theory of metals* (Cambridge University Press, 2003).

[21] M. P. Gelfand and J. P. Lu, "Orientational disorder and electronic states in C_{60} and A_3C_{60}, where A is and alkali metal", Phys. Rev. Lett. **68,** 1050 (1992).

[22] E. J. Mele and S. C. Erwin, "Electron propagation in orientationally disordered fullerides", Phys. Rev. B **50,** 2150 (1994).

[23] O. Gunnarsson, E. Koch, and R. M. Martin, "Mott transition in degenerate Hubbard models: Application to doped fullerenes", Phys. Rev. B **54,** R11026 (1996).

[24] E. Koch, O. Gunnarson, and R. Martin, "Filling dependence of the Mott transition in the degenerate Hubbard model", Phys. Rev. B **60,** 15714 (2000).

[25] J. E. Han, E. Koch, and O. Gunnarsson, "Metal-insulator transitions: influence of lattice structure, Jahn Teller Effect and Hund's rule coupling", Phys. Rev. Lett. **84,** 1276 (2000).

[26] M. Capone, M. Fabrizio, P. Giannozzi, and E. Tosatti, "Theory of the metal-nonmagnetic Mott-Jahn-Teller insulator transition in K_4C_{60}", Phys. Rev. B **62,** 7619 (2000).

[27] V. Brouet, H. Alloul, S. Garaj, and L. Forró, "Gaps and excitations in fullerides with partially filled bands: NMR study of Na_2C_{60} and K_4C_{60}", Phys. Rev. B **66,** 155122 (2002).

[28] P. Fazekas, in *Lecture notes on electron correlation and magnetism* (World Scientific, 1999).

[29] M. Knupfer and J. Fink, "Mott Hubbard-like behaviour of the energy gap of A_4C_{60} (A = Na, K, Rb, Cs) and $Na_{10}C_{60}$", Phys. Rev. Lett. **79,** 2714 (1997).

[30] R. Kerkoud, P. Auban-Senzier, D. Jerome, S. Brazovskii, I. Luk'Yanchuk, N. Kirova, F. Rachdi, and C. Goze, "Insulator-metal transition in Rb_4C_{60} under pressure from ^{13}C-NMR", J. Phys. Chem. Sol. **57,** 143 (1996).

[31] A. M. Rao, P. Zhou, K. A. Wang, G. T. Hager, J. M. Holden, Y. Wang, W. T. Lee, and X. X. Bi, "Photoinduced polymerisation of solid C_{60} films", Science **259,** 955 (1991).

[32] Y. Iwasa *et al.*, "New phases of C_{60} synthesized at high pressure", Science **264,** 1570 (1992).

[33] M. Nuñez-Regueiro, L. Marques, J. L. Hodeau, O. Bethoux, and M. Perroux, "Polymerised fullerite structure", Phys. Rev. Lett. **74,** 278 (1995).

[34] L. Marquez, M. Mezouar, J. L. Hodeau, M. Nuñez-Regueiro, N. R. Serebryanaya, V. A. Ivdenko, V. D. Blank, and G. A. Dubitsky, "'Debye-Scherrer Ellipses' from 3D fullerene polymers: an anisotropic pressure memory signature", Science **283,** 1720 (1999).

[35] S. Pekker, G. Oszlanyi, and G. Faigel, "Structure and stability of covalently bonded polyfulleride ions in A_xC_{60}", Chem. Phys. Lett. **282,** 435 (1998).

[36] V. A. Davydov, L. S. Kashevarova, A. V. Rachmanina, V. Agafonov, H. Allouchi, R. Ceolin, A. V. Dzyabchenko, V. M. Senyavin, and H. Szwarc, "Tetragonal polymerised phase of C_{60}", Phys. Rev. B **58,** 14786 (1998).

[37] J. Winter and H. Kuzmany, "Potassium doped fullerene KC_{60} with x = 0, 1, 2, 3, 4 and 6", Solid State Commun. **84,** 935 (1992).

[38] D. Arčon, K. Prassides, S. Margadonna, A.-L. Maniero, L. Brunel, and K. Tanigaki, "Electron spin resonance study of the polymeric phase of Na_2RbC_{60}", Phys. Rev. B **60,** 3856 (1999).

[39] G. M. Bendele, P. W. Stephens, K. Prassides, K. Vavekis, K. Kordatos, and K. Tanigaki, "Effect of charge state on polymeric bonding geometry: the ground state of Na_2RbC_{60}", Phys. Rev. Lett. **80,** 736 (1998).

[40] G. Oszlanyi, G. Baumgartner, G. Faigel, and L. Forró, "Na_4C_{60}: and alkali intercalated two dimensional polymer", Phys. Rev. Lett. **78,** 4438 (1997).

[41] Y. Kubozono, Y. Takabayashi, T. Kambe, S. Fujiki, S. Kashino, and S. Emura, "Structure and physical properties of Na_4C_{60} under ambient and high pressure", Phys. Rev. B **63,** 045418 (2001).

[42] G. Oszlanyi, G. Baumgartner, G. Faigel, L. Granasy, and L. Forró, "Polymer-monomer phase transition in Na_4C_{60}", Phys. Rev. B **58,** 5 (1998).

[43] T. Shiroka, M. Riccò, F. Barbieri, E. Zannoni, and M. Tomaselli, "Clustering and polymerization of $Li_{15}C_{60}$", Physics of the solid state **44,** 521 (2001).

[44] M. J. Rosseinsky, "Recent developments in the chemistry and physics of metal fullerides", Chem. Mater. **10,** 2665 (1998).

[45] O. Zhou, R. M. Fleming, D. W. Murphy, M. J. Rosseinky, A. P. Ramnirez, R. B. van Dover, and R. C. Haddon, "Increased transition temperature in superconducting Na_2CsC_{60} by intercalation of ammonia", Nature **362,** 433 (1993).

[46] H. Shimoda, Y. Iwasa, Y. Miyamoto, Y. Maniwa, and T. Mitani, "Superconductivity of fcc fullerides containing off-centered octahedral cations", Phys. Rev. B **54,** R15 653 (1996).

[47] S. Margadonna, E. Aslanis, and K. Prassides, "Ammoniated alkali fullerides $(ND_3)NaA_2C_{60}$: ammonia specific effects and superconductivity", J. Am. Chem. Soc. **124,** 10146 (2002).

[48] T. Shiroka, G. Fumera, O. Ligabue, G. Antonioli, and M. Riccò, "NMR structural investigations of ammonia-doped fullerides", Chem. Phys. Lett. (submitted).

[49] M. Riccò, G. Fumera, T. Shiroka, O. Ligabue, C. Bucci, and F. Bolzoni, "Metal-to-insulator evolution in $(NH_3)_xNaK_2C_{60}$: an NMR study", Phys. Rev. B **68,** 035102 (2003).

[50] C. Giacovazzo, H. L. Monaco, D. Viterbo, F. Scordari, G. Gilli, G. Zanotti, and M. Catti, in *Fundamentals of crystallography*, C. Giacovazzo, ed., (International Union of Crystallography - Oxford University Press, 1992).

[51] M. Kara and K. Kurki-Suonio, "Symmetrized multipole analysis of orientational distributions", Acta Cryst. **A37,** 201 (1981).

[52] J. Schwinger, "On the classical radiation of accelerated electrons", Phys. Rev. **75,** 1912 (1949).

[53] G. Margaritondo, Y. Hwu, and G. Tromba, "Synchrotron light: from basics to coherence-related applications", Conference Proceedings on Synchrotron Radiation: Fundamentals, Methodologies and Applications p. 25 (2001).

[54] J. I. Langford and D. Louër, "Powder diffraction", Rep. Prog. Phys. **59,** 131 (1996).

[55] B. D. Cullity, in *Elements of x-ray diffraction* (Addison-Wesley publishing company, Inc., 1967).

[56] A. C. Larson and R. V. Dreele, in *GSAS - General Structure Analysis System* (2000).

[57] D. A. Long, in *The Raman effect: a unified treatment of the theory of Raman scattering by molecules* (John Wiley and Sons Ltd, 2002).

[58] J. H. Weaver and D. M. Poirier, "Solid State Properties of Fullerene and Fullerene-Based Materials", In *Solid State Physics. Advances in Research and Applications*, H. Ehrenreich and F. Spaepen, eds.,**48,** 225–347 (Academic Press Limited, Boston, San Diego, New York, London, Sydney, Tokyo, Toronto, 1994).

[59] K. Prassides, J. Tomkinson, C. Christides, M. J. Rosseinsky, D. W. Murphy, and R. C. Haddon, "Vibrational spectroscopy of superconducting K_3C_{60} by inelastic neutron scattering", Nature **354,** 462 (1991).

[60] P. H. M. van Loosdrecht, P. J. M. van Bentum, and G. Meijer, "Rotational ordering transition in single crystal C_{60} studied by Raman spectroscopy", Phys. Rev. Lett. **68,** 1176 (1992).

[61] K. A. Wang, Y. Wang, F. Zhou, J. M. Holden, S. L. Ren, G. T. Hager, H. F. Ni, P. C. Elkund, G. Dresselhaus, and M. S. Dresselhaus, "Raman scattering in C_{60} and alkali-metal-doped C_{60} films", Phys. Rev. B **45,** 1955 (1992).

[62] P. Zhou, K. A. Wang, Y. Wang, and P. C. Helkund, "Raman scattering in C_{60} and alkali-metal-saturated C_{60}", Phys. Rev. B **46,** 2595 (1992).

[63] P. Zhou, K. A. Wang, P. C. Eklund, G. Dresselhaus, and M. S. Dresselhaus, "Raman scattering study of the electron-phonon interaction in M_3C_{60} (M=K, Rb)", Phys. Rev. B **48,** 8412 (1993).

[64] P. Zhou, K. A. Wang, A. M. Rao, P. C. Eklund, G. Dresselhaus, and M. S. Dresselhaus, "Raman scattering study of homogeneous K_3C_{60} films", Phys. Rev. B **45,** 10838 (1992).

[65] T. Wågberg and B. Sundqvist, "Raman study of the two-dimensional polymers Na_4C_{60} and tetragonal C_{60}", Phys. Rev. B **65,** 155421 (2002).

[66] V. A. Davydov, L. S. Kashevarova, and A. V. Rakhmanina, "Spectroscopic study of pressure-polymerized phases of C_{60}", Phys. Rev. B **61,** 11936 (2000).

[67] G. B. Adams and J. B. Page, "Theoretical studies of Raman spectra for planar polymerized C_{60}", Phys. Stat. Sol. (b) **1,** 95 (226).

[68] P. E. Werner, L. Eriksson, and M. Westdahl, "TREOR, a semi-exaustive trial-and-error powder indexing program for all symmetries", J. Appl. Phys. **18,** 367 (1985).

[69] A. Boultif and D. Louër, "Indexing of powder diffraction patterns for low-symmetry lattices by the successive dichotomy method", J. Appl. Phys. **24,** 987 (1991).

[70] J. W. Visser, "A fully automatic program for finding the unit cell from powder data", J. Appl. Phys. **2,** 89 (1969).

[71] D. Porob and T. N. Gururow, "Ab initio structure determination via powder x-ray diffraction", Proc. Indian. Acad. Sci. **113,** 435 (2001).

[72] G. S. Pawley, "Unit-cell refinement from powder diffraction scans", J. Appl. Phys. **14,** 357 (1981).

[73] A. L. Bail and D. Louër, "Smoothing and validity of crystallite-size distributions from x-ray line profile analysis", J. Appl. Phys. **11,** 50 (1978).

[74] M. Sakata, R. Mori, S. Kumazawza, M. Takata, and H. Toraya, "Electron-density distribution from x-ray powder data by use of profile fits and the maximum-entropy method", J. Appl. Phys. **23,** 526 (1990).

[75] M. W. Deem and J. M. Newsam, "Determination of 4-connected framework crystal structures by simulated annealing", Nature **342,** 260 (1989).

[76] H. M. Rietveld, "Line profiles of neutron powder-diffraction peaks for structure refinement", Acta Cryst. **22,** 151 (1967).

[77] G. Caglioti and F. P. Ricci, "Choice of collimators for a crystal spectrometer for neutron diffraction", Nuclear Instruments **3,** 223 (1958).

[78] K. Holkzer, O. Klein, S. M. Huang, R. B. Kaner, K. J. Fu, R. L. Whetten, and F. Diederich, "Alkali-fullerides superconductors: synthesis, composition and diamagnetic shielding", Science **252,** 1154 (1991).

[79] D. W. Murphy, M. J. Rosseinsky, R. M. Fleming, R. Tycko, A. P. Ramirez, R. C. Haddon, G. Dabbagh, J. C. Tully, and R. E. Walstedt, "Synthesis and characterisation of alkali metal fullerides: A_xC_{60}", J. Phys. Chem. Sol. **53,** 1321 (1996).

[80] H. D. Fair and R. F. Walker, in *Energetic materials - 1 Physics and chemistry of the inorganic azides* (Plenum Press - New York and London, 1977).

[81] R. A. Levy, "Electron spin resonance in metals and metal-ammonia solutions", Phys. Rev. **102,** 31 (1956).

[82] J. C. Wasse, S. Hayama, and N. T. Skipper, "Structure of a metallic solution of lithium in ammonia", Phys. Rev. B **61,** 11993 (2000).

[83] F. Zhou, C. Jehoulet, and A. J. Bard, "Reduction and electrochemistry of C_{60} in liquid ammonia", J. Am. Chem. Soc. **114,** 11004 (1992).

[84] X. Chen and S. Yamanaka, "Single crystal x-ray structural refinement of the 'tetragonal' C_{60}", Chem. Phys. Lett. **360,** 501 (2002).

[85] T. Hahn, in *International tables of crystallography - Volume A*, T. Hahn, ed., (Addison-Wesley publishing company, Inc., 2001).

[86] A. Huq, P. W. Stephens, G. M. Bendele, and R. M. Ibberson, "Polymeric fullerene chains in RbC_{60} and KC_{60}", Chem. Phys. Lett. **347,** 13 (2001).

[87] Y. Maniwa, H. Ikejiri, I. Tou, M. Yasukawa, and S. Yamanaka, "NMR of Li-doped C_{60} polymers", Synth. Met. **121,** 1105 (2001).

[88] S. Margadonna, D. Pontiroli, M. Belli, T. Shiroka, M. Riccò, and M. Brunelli, "Li_4C_{60}: a polymeric fulleride with a two dimensional architecture and mixed interfullerene bonding motif', J. Am. Chem. Soc. **126,** 15032 (2004).

[89] M. Riccò, T. Shiroka, M. Belli, D. Pontiroli, M. Pagliari, G. Ruani, D. Palles, S. Margadonna, and M. Tomaselli, "Unusual polymerisation in the Li_4C_{60} fulleride", Phys. Rev. B **72,** 155437 (2005).

[90] M. Tomaselli, B. H. Meier, M. Riccò, T. Shiroka, and A. Sartori, "NMR evidence for sp^3 carbon in the low-temperature phase of Li_xC_{60}", Phys. Rev. B **63,** 113405 (2001).

[91] R. Roding, T. Wågberg, and B. Sundqvist, "Raman spectroscopy and x-ray diffraction studies of the single- and double-bonded two dimensional polymers $Na_nLi_{4-n}C_{60}$", J. Phys. Chem. Sol. **65,** 355 (2004).

[92] D. Pontiroli, M. Riccò, T. Shiroka, M. Belli, G. Ruani, D. Palles, and S. Margadonna, "New polymeric phase in low-doped lithium intercalated fullerides", Fullerenes, Nanotubes and Carbon Nanostructures (in press).

[93] S. Margadonna, C. M. Brown, K. Prassides, A. N. Fitch, K. D. Knudsen, T. L. Biham, M. Mezouar, I. Hirosawa, and K. Tanigaki, "Temperature and pressure dependence of orientational disorder and bonding in Li_2CsC_{60}", Inorg. Mater. **1,** 157 (1999).

[94] F. J. Dyson, "Electron spin resonance absorption in metals. II. Theory of electron diffusion and the skin effect", Phys. Rev. **98,** 349 (1955).

[95] R. Moret *et al.*, "Structural phase transitions in single crystal C_{60}", J. Phys. I France **2,** 511 (1992).

[96] F. C. V. der Lage and H. A. Bethe, "A method for obtaining electronic eigenfunctions and eigenvalues in solids with an application to sodium", Phys. Rev. **71,** 612 (1947).

[97] J. R. Carvajal, in *An introduction to the program Fullprof 2000* (2001).

[98] S. C. Erwin and W. E. Pickett, "Theoretical normal-state transport properties of K_3C_{60}", Phys. Rev. B **46,** 14257 (1992).

[99] R. M. Fleming, P. Ramirez, M. j. Rosseinsky, D. W. Murphy, R. Haddon, S. M. Zahurak, and A. V. Markhija, "Relation of structure and superconductiong transition temperatures in A_3C_{60}", Nature **352,** 787 (1991).

[100] I. Lukyanchuk, N. Kirova, F. Rachdi, C. Goze, P. Molinie, and M. Mehring, "Electronic localization in Rb_4C_{60} from bulk magnetic measurements", Phys. Rev. B **51,** 3978 (1995).

[101] P. Durand, G. R. Darling, Y. Dubitsky, A. Zaopo, and M. J. Rosseinsky, "The Mott-Hubbard insulating state and orbital degeneracy in the superconducting $C_{60}{}^{3-}$ fulleride family", Nat. Mater. **2,** 605 (2003).

[102] P. Durand, Y. Dubitsky, M. J. Rosseinsky, and A. Zaopo, "Expanded fullerides and electron localisation - Lithium-rich ammoniated C_{60} phases", Dalton Trans. **19,** 3137 (2004).

[103] M. Riccò, M. Belli, T. Shiroka, D. Pontiroli, M. Pagliari, F. Gianferrari, and A. Gorreri, "μSR and SQUID investigation of ammoniated lithium fullerides", Phys. B (in press).

[104] C. Kittel, in *Introduzione alla fisica dello stato solido* (Bollati Boringhieri, 2001).

[105] J. L. de Boer, S. van Smaalen, V. Petricek, M. Dusek, M. A. Verheijen, and G. Meijer, "Hexagonal close-packed C_{60}", Chem. Phys. Lett. **219,** 469 (1994).

[106] R. Céolin, J. L. Tamarit, D. O. López, M. Barrio, V. Agafonov, F. Moussa, and H. Szwarc, "Hexagonal close-packed C_{60}", Chem. Phys. Lett. **219,** 21 (1999).

[107] E. V. Skokan, I. V. Arkhangelskii, D. E. Izotov, N. V. Chelovskaya, and M. M. N. Y. A. Velikodnyi, "Stability of hexagonal modification of fullerite C_{60}", Carbon **43,** 803 (2005).

[108] R. P. Stratton and W. J. Kitchingman, "Stacking faults densities in hexagonal gold alloys", Brit. J. Appl. Phys. **17,** 1039 (1996).

[109] B. E. Warren, "X-ray diffraction in random layer lattices", Phys. Rev. **59,** 693 (1966).

[110] L. Velterop, R. Delhez, T. H. de keijser, E. J. Mittemeijer, and D. Reefman, "X-ray diffraction analysis of stacking and twin faults in f.c.c. metals: a revision and alloeance for texture and non-uniform fault probabilities", Appl. Cryst. **33,** 296 (2000).

[111] F. M. Mueller and M. Priestley, "Inversion of cubic de Haas-van Alphen data, with and application to Palladium", Phys. Rev. **148,** 638 (1966).

Acknowledgements

Dopo tutta la fatica fatta per vergare queste centocinquanta pagine in inglese, sento la necessità di scrivere la pagina dei ringraziamenti nella mia madrelingua.

Desidero innanzitutto ringraziare il mio supervisore Mauro Riccò, per avermi dato la possibilità di fare ricerca nel Gruppo Fullereni di Parma. Sono a lui grato specialmente per il bellissimo rapporto professionale che è riuscito ad instaurare con me e i miei collaboratori, e per la fiducia che ha sempre riposto nelle nostre capacità; questo mi è stato di grande aiuto per portare a termine il mio lavoro.

Un grazie particolare a Toni Shiroka, per l'instancabile ed impagabile aiuto offertomi sempre con grande disponibilità. Grazie alla sua elevata competenza informatica, al virtuosismo linguistico e alla sua profonda conoscenza scientifica, mi è stato possibile superare brillantemente problemi e situazioni apparentemente insormontabili.

Stringo con un abbraccio il caro Matteo Belli, per la sua pazienza e disponibilità dimostratami sempre, ed in particolare in quest'ultimo periodo di stesura della tesi (filo diretto su Skype ventiquattro ore su ventiquattro!). Durante le numerose missioni e scuole a cui abbiamo partecipato insieme, è nato un rapporto di amicizia che spero durerà a lungo.

Un grazie sincero a Massimo Pagliari, per le importanti consulenze e discussioni di chimica, per avermi fatto conoscere il mondo Mac, ma soprattutto per le divertenti giornate trascorse nel laboratorio di sintesi, alle prese con ogni tipo di sostanze tossiche.

Desidero inoltre ringraziare Fabio Gianferrari, che per primo mi ha fatto conoscere al Gruppo Fullereni, quasi tre anni fa; è stato inoltre fondamentale il suo aiuto di "hackeraggio informatico" (mitico "magicVNC"!).

Come poi non ricordare l'aiuto di Sandra, che con amorevole precisione ha provveduto alla gestione del laboratorio, ed è riuscita pure a soddisfare il nostro palato (anche se non troppo spesso!) con delle buonissime torte, contribuendo a creare fra noi un clima sereno e familiare.

Voglio inoltre ricordare Massimiliano ed Angelo, validi colleghi, e Giuseppe Allodi, vero "guru" di Linux, per il provvidenziale aiuto informatico.

Durante questi anni di Dottorato, ho avuto modo di stringere importanti collaborazioni, assolutamente fondamentali per portare avanti il mio lavoro, con persone di alto livello scientifico. Desidero in particolare ringraziare la cara Serena Margadonna, per l'aiuto e gli importanti insegnamenti ricevuti durante il periodo trascorso a Cambridge, Denis Arčon, per l'accoglienza con cui mi ha accolto a Ljubljana, e Giampiero Ruani.

Voglio ricordare poi tutti i componenti del mio bellissimo ufficio, la mitica "Area 51": Margherita, Alessia, Christian, Silvia, Elena, che hanno sopportato i miei fastidiosi pensieri ad alta voce nei momenti passati davanti al computer. Un ringraziamento speciale va a Raffaella, cara amica, con cui non solo ho trascorso nove anni di studio universitario, ma anche tre lunghi anni di pendolaraggio Piacenza-Parma, tra mille gioie e dolori; il suo impagabile aiuto, il potermi confrontare con la sua non comune intelligenza e la sua schiettezza, sono stati per me sempre motivo di sprone a migliorarmi.

Grazie a Erica, amica di vecchia data, che mi ha fornito importanti consulenze di cristallografia, veramente utili per il mio lavoro.

Grazie a Samantha per l'aiuto morale che ho ricevuto da lei in moltissime circostanze, specialmente nei momenti difficili, e per il bellissimo "angolo caffè" che siamo ultimamente riusciti ad organizzare nel Laboratorio Film Sottili.

Un pensiero poi a Chiara e a tutti i dottorandi di Fisica e Scienze dei Materiali che molto "democraticamente" hanno sostenuto in questi anni la mia carica di loro rappresentante.

Grazie a Valentina, per l'amicizia che è nata fra noi durante il viaggio Piacenza-Parma; il ritrovo la mattina al "Bar Paradiso" ha contribuito ad allietare l'inizio della giornata lavorativa.

Grazie a Paolo, per l'amicizia nata ai tempi della mia tesi di laurea e continuata sul treno. Sono stati importanti i suoi consigli sull'uso di Matlab, e il suo suggerimento di scrivere la tesi con Lyx.

Un pensiero speciale a Daniela, che ho avuto la fortuna di conoscere durante il periodo di dottorato.

Da ultimo, ringrazio con grande affetto i miei genitori, che da sempre mi hanno aiutato e sostenuto, partecipando sia materialmente che moralmente a tutte le esperienze che ho vissuto in questi anni.